

Fabricating Silicon Germanium Waveguides by Low Pressure Chemical Vapor Deposition

by

Dean Edward Berlin

B.S., Materials Science and Engineering (2000)

Massachusetts Institute of Technology

Submitted to the Department of Materials Science and Engineering
in Partial Fulfillment of the Requirements for the Degree of

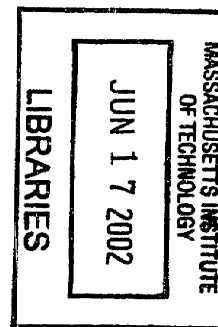
Master of Science with Recommendation
from the Department of Materials Science and Engineering

at the

MASSACHUSETTS INSTITUTE OF TECHNOLOGY

February 2002

© 2002 Massachusetts Institute of Technology
All rights reserved



ARCHIVES

Signature of Author:
Department of Materials Science and Engineering
December 27, 2001

Certified by:
Eugene A. Fitzgerald
Professor, Department of Materials Science and Engineering
Thesis Supervisor

Accepted by:
Harry L. Tuller
Chairman, Departmental Committee on Graduate Students

Fabricating Silicon Germanium Waveguides by Low Pressure Chemical Vapor Deposition

by

DEAN EDWARD BERLIN

Submitted to the Department of Materials Science and Engineering on December 27, 2001 in partial fulfillment of the requirements for the Degree of Master of Science with Recommendation from the Department of Materials Science and Engineering

Abstract

Low loss optical waveguide structures combining the high bandwidth of light transmission and the economics of silicon substrates have been made possible by Low Pressure Chemical Vapor Deposition (LPCVD). This work explores the fabrication, modeling, and testing of LPCVD SiGe waveguides.

Thesis research was conducted during a six-month internship at Applied Materials, a semiconductor equipment manufacturing company. The present work can be divided into two parts: developmental work on the Applied Materials' Epi Centura® LPCVD reactor and use of this reactor to fabricate optical waveguides. Development was performed on the reactor to improve its performance for the deposition of epitaxial SiGe films in several essential aspects. The wafer heating and flow uniformity was given greater flexibility by employing a 3-zone heating lamp module, AccuSETT® flow controllers, and flow baffles. $1\sigma=0.58\%$ was achieved for thickness uniformity. The incorporation of an in-line purifier in the GeH_4 supply line was found to reduce the oxygen concentration below the SIMS detection limit. Process conditions were identified for selective silicon epitaxial growth on silicon surfaces and not on oxide surfaces. Atomic force microscopy was used to characterize the surface roughness of polycrystalline SiGe films deposited on nitride and oxide layers. The effect of C incorporation on the suppression of B diffusion was confirmed using this reactor. The addition of C to the SiGe lattice was shown to nullify the strain associated with epitaxial deposition on Si.

Using the optimized reactor, optical waveguides were fabricated to determine the optimum processing conditions to produce low transmission loss structures. XRD scans on these samples confirm that low Ge concentration and relaxed structures were fabricated. Attenuation measurements in straight waveguide sections confirm that low loss transmission is achievable. The basic equations of optical transmission in planar waveguides are presented and solved for square cross-section strip SiGe waveguide design. The Marcatili method was used to model the electric field mode profiles in the waveguide core and cladding. Curved structures were designed to explore the crosstalk and coupling effects between adjacent waveguides.

Thesis Supervisor: Eugene A. Fitzgerald

Title: Professor of Materials Science and Engineering

Table of Contents

Chapter 1 Introduction	10
Chapter 2 Background	12
2.1 Epitaxial Films.....	12
2.2 Photonic devices and SiGe	17
2.3 Microelectronic Devices and SiGe	23
2.3.1 MOSFETs.....	23
2.3.2 HBTs	26
2.4 Basics of Chemical Vapor Deposition.....	29
2.5 Applied Materials' Epi Centura® LPCVD.....	34
Chapter 3 Metrology Tools	36
Section 3.1 XRD – Film Strain & Composition	36
Section 3.2 Ellipsometry – Thickness & Composition Uniformity	38
Section 3.3 SIMS – Accurate Concentration Profiling.....	39
Section 3.4 FTIR – Film Thickness	41
Section 3.5 AFM – Surface Roughness.....	41
Chapter 4 LPCVD Hardware Modifications.....	43
Section 4.1 Achieving Uniform Chamber Conditions.....	44
Sub-Section 4.1.1 Temperature Calibration.....	45
Sub-Section 4.1.2 Improving Flow Uniformity.....	51
Sub Section 4.1.2-A Fine Tuning: AccuSETT® Valves	54
Sub Section 4.1.2-B Fine Tuning: Carrier Gas Flow	57
Sub-Section 4.1.3 Improving Deposition Uniformity.....	59
Section 4.2 Purifying Process Gases	60
Chapter 5 LPCVD Process Characterization.....	65
Section 5.1 Selective Epitaxial Growth	65
Section 5.2 Polycrystalline SiGe on Oxide and Nitride.....	68
Section 5.3 SiGeC Epitaxial Films	70
Sub-Section 5.3.1 Effect of C on B Diffusivity	70
Sub-Section 5.3.2 SiGeC Strain Compensation.....	72

Chapter 6 Application: Waveguides	76
Section 6.1 Waveguide Equations	76
Section 6.2 Solution of Waveguide Equations	83
Section 6.3 Waveguide Fabrication	90
Section 6.4 Optical Loss Measurements	96
Section 6.5 Future Waveguide Test Structures	100
Chapter 7 Thesis Summary & Recommendations	103
2.6 LPCVD Chamber Improvements	103
2.6.1 Summary of Results & Conclusions	103
2.6.2 Recommendations for Future work	104
2.7 Waveguides	105
2.7.1 Conclusions	105
2.7.2 Recommendations for Future Work	106
Chapter 8 Acknowledgements	108
Chapter 9 References.....	110
Chapter 10 Appendix.....	113
Section 10.1 Units	113
Section 10.2 Derivation of Wave Equations.....	114
Section 10.3 Aeronex GateKeeper® Hydride Gas Purifier Data Sheet.....	118

List of Figures

Figure 2.1: Pseudomorphic and relaxed heteroepitaxy. Film relaxes by forming misfit dislocations at interface. (Adapted from [17])	12
Figure 2.2: Critical thickness vs. composition for $\text{Si}_{1-x}\text{Ge}_x$ on Si [3].	14
Figure 2.3: Diamond-lattice crystal structure of Si.....	14
Figure 2.4: Band gap variation of $\text{Si}_{1-x}\text{Ge}_x$ alloys against composition [3].	16
Figure 2.5: Increasing the Ge fraction strongly increases the growth rate [23].....	16
Figure 2.6: An integrated optical system [24]	18
Figure 2.7: Arrayed waveguide grating [25]	18
Figure 2.8: Absorption co-efficient versus wavelength for Si and Ge.....	20
Figure 2.9: Dispersion of refractive index for Si, Ge, and SiGe alloys of Figure 2.8 [32].....	20
Figure 2.10: The basic MOSFET structure. (a) Idealized cut-away view of a p-channel MOSFET and corresponding circuit symbol. (b) Simplified cross-sectional view showing the terminal designations, carrier and current flow directions, and standard biasing conditions	24
Figure 2.11: Extended Source/Drain to produce shallow junctions	25
Figure 2.12: (a) the basic N^+PN BJT physical structure (b) spatial visualization of diffusion currents under active mode biasing [6]	26
Figure 2.13: Simultaneous deposition of epitaxial base contact and polycrystalline base electrode.....	29
Figure 2.14: CVD Processes: (1) Reactant transport to wafer region; (2) Reactant diffusion through boundary layer to wafer surface; (3) Reactant adsorption on surface; (4) Reactant decomposition and diffusion along surface; (5) Desorption of reaction byproducts from wafer surface; (6) Byproduct diffusion through boundary layer; (7) Byproducts exit the system via exhaust	29
Figure 2.15: “Classic” plot of the regime transition [13]. (A) Reaction-rate limited regime; (B) Mass flow-limited regime. This should be compared with Figure 4.1 on page 44.....	33
Figure 2.16: Growth velocity vs. $1/T$ for atmospheric and reduced pressure conditions. The lower total pressure (with P_R and C_R remaining fixed) shifts the h_g curve upward, extending the surface reaction regime to higher temperatures [11].	34
Figure 2.17: Epi Centura® LPCVD reactor	35
Figure 3.1: Bragg Diffraction.....	37
Figure 3.2: Ellipsometry apparatus	38
Figure 3.3: SIMS profiles obtained to show the “mixing effect”	40
Figure 3.4: FTIR measured spectrum overlaid on model spectrum. This particular fringe pattern corresponds to a $4.232\mu\text{m}$ thick epilayer of intrinsic Si on p^+ substrate.....	41

Figure 3.5: AFM principle of operation	42
Figure 4.1: Empirically determined LPCVD growth rate data for 200slm SiH ₂ Cl ₂ (DCS) 20Torr. This should be compared with Figure 2.15 on page 33.	44
Figure 4.2: Causes of thermal non-uniformity include: (a) reduced view factor to the lamp array for large <i>r</i> , (b) very small view factors along the wafer edge, and (c) non-uniform gas phase heat transfer [13]. ...	45
Figure 4.3: Orientation of thermocoupled wafer in process chamber.....	47
Figure 4.4: Lower Pyrometer Calibration (20Torr).....	47
Figure 4.5: Center-point thermocouple temperature vs. delivered lamp power (20Torr).....	48
Figure 4.6: Diagram showing lamp bank illuminating wafer and susceptor	48
Figure 4.7: Inner/Middle/Outer lamp power distribution calibration	49
Figure 4.8: Reducing right-left asymmetry by replacing bent support shaft	50
Figure 4.9: Testing the effect of different inject orifice heights	52
Figure 4.10: Testing the effect of flow straighteners.....	53
Figure 4.11: Testing different baffles combinations.....	54
Figure 4.12: Inner vs. Outer AccuSETT® Flow	55
Figure 4.13: Inner/Outer AccuSETT® Calibration with 6/9/6 baffles	55
Figure 4.14: Inner/Outer AccuSETT® Calibration with 7/7/7 baffles	56
Figure 4.15: Main/Slit valve flow calibration.....	58
Figure 4.16: Increasing the main H ₂ flow changes the Si thickness uniformity (6/9/6, 1/4" orifice, no flow straighteners)	58
Figure 4.17: Uniform deposition at T=1000°C	59
Figure 4.18: DCS thickness and %Ge profiles (300/300)	60
Figure 4.19: Lifetime trends in oxygen-doped Si _{1-x} Ge _x films, for 0.15< <i>x</i> <0.31. The open symbols represent lifetime data from the <i>p</i> ⁺ - <i>i-n</i> diodes, while the closed symbols represent lifetimes extracted by simulating data for Si/Si _{1-x} Ge _x HBTs. The shaded region indicates the approximate sensitivity limits for determining the oxygen content and lifetime in these <i>p</i> ⁺ - <i>i-n</i> diodes [9].	61
Figure 4.20: Oxygen content versus 9.1μm absorption coefficient [37].	61
Figure 4.21: Resistivity versus impurity concentration in Si at 300K [6]	62
Figure 4.22: GeH ₄ purifier manifold	63
Figure 4.23: Saturation of Aeronex GateKeeper® Hydride Gas Purifier	63
Figure 4.24: SIMS profile of Ge-containing film deposited at decreasing wafer temperatures	64

Figure 5.1: Results of SEG experiments mapped in the process space; open diamonds indicates deposition on oxide, closed diamonds indicates no deposition on oxide	67
Figure 5.2: Poly SiGe on nitride.....	70
Figure 5.3: Poly SiGe on oxide	70
Figure 5.4: Poly SiGe on nitride.....	70
Figure 5.5: Poly SiGe on oxide	70
Figure 5.6: C suppresses the diffusion of B in the SiGe lattice	72
Figure 5.7: Increasing SiCH ₆ flow leads to strain compensation. Pseudomorphic growth is maintained, as seen by the well-defined fringe pattern.	73
Figure 5.8: Complete strain compensation is realized for higher SiCH ₆ flow rates. Films are no longer completely pseudomorphic.....	74
Figure 5.9: SIMS measurement of fully strained compensated SiGeC thin film.....	75
Figure 6.1: Two dimensional waveguide structure [24]. Compare with Figure 6.11.	76
Figure 6.2: Graphical solution of Equation 6.5 to determine the bounce angles θ_m of the modes of a planer dielectric waveguide. The RHS and LHS of Equation 6.5 are plotted versus $\sin \theta$. The intersection points, marked by filled circles, determine $\sin \theta_m$. Each branch of the tan or cot function in the LHS corresponds to a single mode. In this plot $\sin \theta_m = 8(\lambda / 2d)$, and there are 9 modes [24].....	78
Figure 6.3: The values of k_x and k_y for the waveguide modes are marked by dots [24].	79
Figure 6.4: Arbitrary waveguide modes [24]	82
Figure 6.5: Waveguide cross-section divided by the Marcatili method	84
Figure 6.6: Propagation constant for different modes and guides. ——— transcendental equation solutions; — — — closed form solution; —·—·— computer solution of the boundary value problem [39]. [38]	85
Figure 6.7: Electric field distribution in and around 2 μ m square cross-section waveguide: (a) 2D field distribution; (b) Contour map.....	87
Figure 6.8: Electric field distribution in and around 3 μ m square cross-section waveguide: (a) 2D field distribution; (b) Contour map.....	88
Figure 6.9: Change of γ^l with Ge fraction for 2 μ m and 3 μ m waveguides, $n_2=3.5$	89
Figure 6.10: Change of γ^l with waveguide height $n_1=3.52$ and $n_2=3.5$ for 2 μ m and 3 μ m waveguides.....	89
Figure 6.11: Waveguide process flow	92
Figure 6.12: Both the 2 μ m and 3 μ m core regions are in the metastable range	93
Figure 6.13: Symmetric XRD scans on 3 μ m thick, with no grade sample.....	94

Figure 6.14: Optical micrograph and Scanning electron micrograph of waveguide structure.....95

Figure 6.15: Optical micrograph showing defectivity near waveguide. Left image is 3.6X magnification, enlarged image is 36X.....95

Figure 6.16: SEM micrograph of sidewall roughness after DRIE.....96

Figure 6.17: Optical Loss Measurement Apparatus: (a) photograph; (b) diagram with ray tracing (not to scale).....97

Figure 6.18: Image of light being transmitted through SiGe waveguide. Compare with model in Figure 6.8. 3µm core, no grade.....99

Figure 6.19: Cutback measurement results on typical SiGe waveguides [34].....99

Figure 6.20: Variation in transmission loss with waveguide width.....100

Figure 6.21: Radial curves.....101

Figure 6.22: Directional coupler.....102

Figure 6.23: Y-branch splitter; both left branches extend to form long parallel lines102

Figure 6.24: Finite-Element Array that may be used to model beam profile a) along straight section & b) turning bends102

Figure 10.1: Electric and magnetic field in an electromagnetic wave115

Figure 10.2: Aeronex GateKeeper® Data Sheet-1 [31].....118

Figure 10.3: Aeronex GateKeeper® Data Sheet-2 [31].....119

List of Tables

Table 2.1: Useful parameters of atoms common in Si epitaxy; shaded atoms are intentional electronic dopants [4], [12], & [13].....	17
Table 2.2: Important Waveguide Structural Parameters. Compare with Table 6.1 on page 82.....	23
Table 2.3: Typical conditions for low pressure processing	35
Table 3.1: SIMS Conditions and Measurement Parameters	40
Table 4.1: Summary of results showing effects of changing AccuSETT® settings.....	56
Table 4.2: Thickness and %Ge uniformity experimental conditions and results (6/9/6 baffles)	59
Table 5.1: Effect of process parameters on selective epitaxial deposition	66
Table 5.2: Selective epitaxial growth experimental conditions and results; shaded condition exhibited growth on oxide.....	67
Table 5.3: AFM Images and Root-mean squared roughness of polySiGe on nitride and oxide.....	69
Table 5.4: FWHM of B peaks	72
Table 5.5: Growth conditions for samples shown in Figure 5.7 and Figure 5.8.....	74
Table 6.1: Important Waveguide Physical Parameters. Juxtapose this with Table 2.2 on page 23.	82
Table 6.2: n_{SiGe} critical angle, complementary critical angle, and core wavelength.....	83
Table 6.3: NA, θ_m , β_m , γ_m^{-1} , and the condition of Equation 6.7 for $n_1=3.52$ and $n_2=3.5$	83
Table 6.4: Deposition conditions for waveguide samples	92
Table 6.5: Parameter dimensions of structures and possible tests that may be performed using them	101

Chapter 1 Introduction

Homo sapiens are distinguished from every other species by its engineering ability to use tools and manipulate materials to improve its world. The epochs of mankind's history are named for the materials used: The Stone Age, The Iron Age, and The Bronze Age. By all standards, we now exist in the Silicon Age, and the most stringent demands are placed on the tools employed to create devices from this wondrous material. These demands are constantly becoming more difficult to achieve as device dimensions shrink, performance requirements increase, and the price-per-transistor decreases. Our present telecommunications network is on the verge of huge transition: trading sluggish electrons for light-speed photons. The revolution has already begun, the telecommunications backbone is already composed of optical fibers, but there are several bottlenecks in the systems. The transition has been hindered by the inability to integrate high speed III-V optoelectronic devices on the ubiquitously available silicon substrates. SiGe heterostructures offer the solution. They can be better lattice matched to Si and compositionally tuned to obtain the necessary refractive index for photon confinement. Designing tools to fabricate the next-generation of electrical and optical devices requires a clear understanding of semiconductor material science and device operation physics, with an open ear to possible products, present and future.

One purpose of this thesis is the optimization of Applied Materials' Epi Centura® low-pressure chemical vapor deposition system (LPCVD) for the fabrication of SiGe waveguides. Modifications to the chamber's hardware were implemented to improve wafer uniformity and decrease incorporated impurities. The processing capabilities of the chamber were also characterized with the goal of controllable SiGeC deposition. This thesis provides the science of chemical vapor deposition as a context for the reader, a description of the experiments performed, and the results and conclusions that were achieved.

Light has an information-carrying capacity 10,000 times greater than the highest radio frequencies, and is capable of carrying signals over long distances with little or no heat generation. Additional advantages of optical over electrical transmission include low error rates and immunity to electrical interference. Optical waveguides fabricated on silicon substrates can be directly coupled with optical fibers, for signal multiplexing. Another purpose of this thesis is to study the feasibility of using SiGe

LPCVD epitaxial films to produce silicon photonics. An emerging application of semiconductor materials involves the monolithic integration of optical components on silicon substrates. Optoelectronic devices fabricated from III-V elements have demonstrated their superiority for photonic applications, however they are limited because they cannot be fabricated directly on silicon substrates. Silicon is the industrial standard base material for electronic device fabrication, but because of the large lattice mismatch between it and III-V compounds, deleterious threading dislocations form which prevent their integration. SiGe, on the other hand, can be better lattice matched to Si. The index contrast between Si and SiGe also make it ideal for applications involves optical confinement. It will be shown that it is possible to use this optical confinement to produce low attenuation SiGe waveguides. The basic equations for optical transmission in waveguide structures are presented and solved in this thesis for square cross-section SiGe strip waveguides. Simple Si/SiGe/Si waveguide strips were fabricated and characterized to determine the optimum processing conditions. Loss measurements confirm that low attenuation transmission is possible using SiGe waveguides fabricated directly on a silicon substrates.

In Chapter 2, the science of silicon epitaxy is presented to provide the reader with a context for later discussions of chamber improvements. A brief overview of the applications of SiGe thin films in the microelectronic and photonic arena is provided so that the reader might understand the impetus for chamber development. Chapter 2 concludes with a description of the particular chamber that this work was conducted on, the Epi Centura®.

Chapter 3 describes the metrology tools used to measure the effects of the chamber improvements done in Chapter 4 and Chapter 5. Chapter 4 presents the hardware changes implemented to improve temperature and flow uniformity for achieving controllable deposition of low impurity epitaxial films. Once the optimum hardware configuration has been determined, the processes used to deposit SiGeC are characterized in Chapter 5. Experiments were performed to demonstrate that SiGe could be selectively deposited at low temperatures. The roughness of SiGe polycrystalline films on nitride and oxide surfaces was measured. B diffusion was shown to be suppressed by the incorporation of C on the SiGe film. Conditions for complete strain compensation in SiGe films by allowing with C are also identified.

With the LPCVD chamber optimized and characterized, Chapter 6 describes the use of the chamber to fabricate optical waveguides. The equations for optical transmission are presented and solved to determine the mode profiles. The procedures used for fabricate the SiGe waveguides are presented, and the results of the optical loss measurements identify which are the optimal processing conditions. This chapter concludes with a description of waveguide structures that have been designed to test coupling effect between adjacent waveguides.

Chapter 2 Background

Section 2.1 Epitaxial Films

The primary use of Si epitaxy today is to deposit the atomic layers in which CMOS and bipolar transistors are built. These layers range in thickness from several nanometers to a few microns and serve as either active or passive elements. Emerging applications employ epitaxial films in MEMS devices and optoelectronic systems, the latter of which will be discussed in detail in Section 2.2.

Epitaxial deposition is the process of applying layers of crystalline matter on a surface or substrate. Heteroepitaxy is the deposition of a material on a dissimilar substrate; conversely, homoepitaxy is the deposition on a similar substrate. Heteroepitaxial films generally do not have the same in-plane lattice parameter as the substrate, giving rise to strain fields in the film—common theory assumes all strain is accommodated in the (thin) epilayer and not in the (relatively thick) substrate.

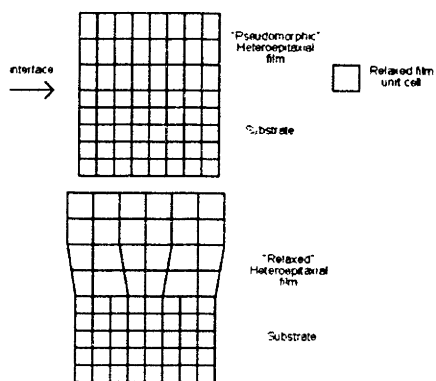


Figure 2.1: Pseudomorphic and relaxed heteroepitaxy. Film relaxes by forming misfit dislocations at interface. (Adapted from [17])

Dislocations are the extra plane of atoms originating at the interface (Figure 2.1). At high enough temperatures, dislocations can quickly travel to the edge wafer and be annihilated. The lattice parameter is the edge length of a unit cell (Figure 2.3). If the in-plane lattice parameter of the epilayer, a_{epi} , is smaller than the in-plane lattice parameter of the substrate, a_s , the film experiences tensile strain. If the epilayer lattice parameter is larger than the substrate parameter, the film experiences compressive strain. This is expressed as the total misfit of the system:

$$f = \frac{a_s - a_{epi}}{a_{epi}} = \varepsilon + \delta$$

Equation 2.1

where ε and δ are the elastic and plastic strain, respectively. If $\delta=0$ the film is totally elastically strained (“coherent” or “unrelaxed”) to conform to the substrate. However, if $\delta \neq 0$ then plastic deformation “relaxes” the film by misfit dislocation formation. Although the formation of dislocations relieves the elastic strain energy with plastic deformation, energy is required to create them. An equilibrium condition can be written to determine the onset of dislocations. Matthews derived an expression for the critical pseudomorphic thickness, h_c , beyond which it becomes energetically favorable to introduce misfit dislocations:

$$h_c = \frac{D(1 - \nu \cos^2 \alpha)(b/b_{eff})[\ln(h_c/b) + 1]}{2Yf}$$

Equation 2.2

where D is the average shear modulus of the interface, Y is Young’s modulus under biaxial stress, b is the magnitude of the Burger’s vector of the dislocations, ν is Poisson’s ratio for the epilayer ([16]). This expression is often visualized as a phase diagram showing dislocated and non-dislocated regimes as a function of mismatch (Figure 2.2). The lowest curve gives the theoretical equilibrium (Equation 2.2), whereas the experimental curve is for a carefully grown metastable layer grown at 550°C by Molecular Beam Epitaxy.

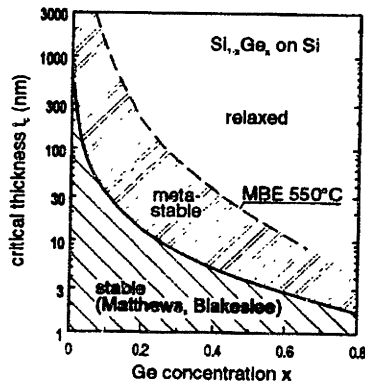


Figure 2.2: Critical thickness vs. composition for $\text{Si}_{1-x}\text{Ge}_x$ on Si [3].

Dislocations disrupt the crystalline symmetry and are damaging to both electronic and photonic devices. Dislocations in the active regions of transistors act as decrease minority carrier lifetimes, reducing gain. They are especially deleterious in photonic devices, since they increase surface roughness. However, the absence of dislocations in a lattice-mismatched film implies that the film is completely strained, and this itself can be detrimental to SiGe waveguides. The strain in pseudomorphic films cause birefringent effects for propagating electromagnetic fields, distorting the electrical and magnetic fields. For lattice mismatched films, films that have two regions, an area in which the lattice is relaxed and a region in which the relaxed material is free from dislocations is ideal.

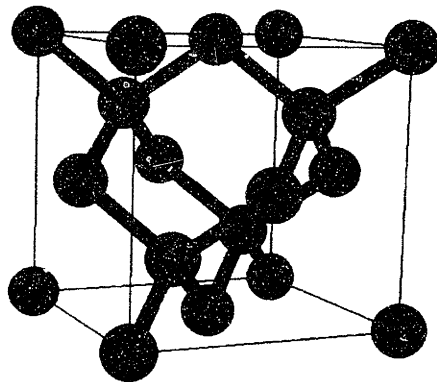


Figure 2.3: Diamond-lattice crystal structure of Si.

In solid form, Si forms a cubic diamond-lattice structure shown in Figure 2.3. The diamond lattice consists of two interpenetrating face-centered cubic Bravais lattices, displaced along the body diagonal of the cubic cell by one quarter the length of the diagonal. It can also be represented as a face-centered cubic

lattice with the two point bases $\hat{0}$ and $(a/4)(\hat{x} + \hat{y} + \hat{z})$. There are eight atoms per unit cell and each atom has four nearest neighbors. The lattice parameter, or edge cell length, of this unit cell is $a_{Si}=5.4309\text{\AA}$. Since there are 8 atoms per unit cell, of volume a_{Si}^3 , it follows that there are 5×10^{22} atoms/cm³ for Si. In crystallographic terminology, an atom is termed *substitutional* if it occupies a lattice site shown in Figure 2.3, but is considered *interstitial* if it resides in the spaces between these sites. For dopants to be electrically active in a controlled way, they must reside on substitutional sites. Although atoms on both type of site affect crystalline strain, the effect is greatest for substitutional atoms.

Alloying Si and Ge in any proportion yields a stable alloy of the $Si_{1-x}Ge_x$ binary system, and the alloy is completely miscible for Ge concentrations. The $Si_{1-x-y}Ge_xC_y$ system, however, is not; there are ranges for x and y that produce stable alloys, and larger ranges of concentrations in which metastable alloys are produced beyond which SiC precipitates may form. Within those ranges C and Ge can be incorporated substitutionally on the Si lattice without creating vacancies or interstitials, and are useful in changing the lattice parameter of the resultant lattice. Due to its larger atomic radius, substitutional Ge incorporation in the Si lattice increases the lattice parameter, resulting in compressive strain in the epilayer when deposited on a Si substrate. The increase is a nearly-linear change from a_{Si} to a_{Ge} . Conversely, substitutional C incorporation decreases the lattice parameter, resulting in tensile strain in the epitaxial film. This increase is linear only for small fractions of C. It will be shown that when C and Ge are both incorporated, these opposing strains can offset each other to produce a strain-free film of high Ge fraction. This layer can itself be an active layer, or be used as a substrate for relaxed active SiGe layers.

The advantages of alloying Si with Ge and C go beyond strain management. Another important effect of adding Ge to Si is the steady decrease of the energy bandgap from 1.12eV for pure Si to 0.67eV for pure Ge, while adding C increases it towards 5.5eV (Figure 2.4). The band gap is the amount of energy required to raise an electron from the valence band to the conduction band of a semiconductor. Once in the conduction band, the electron may contribute to the bulk conductivity (the opposite is true for holes, which conduct in the valence band). The top curve gives the band gap energy for unstrained (cubic) alloys, which show a crossover from the Si-like to the Ge-like band structure at $x=0.85$. The two lower curves are for pseudomorphic $Si_{1-x}Ge_x$ layers on a cubic Si substrate, which leads to a splitting of the valence band. By

aligning the mid-gap energy level, it can be seen that most of this decrease occurs in the valence band, making SiGe attractive for hole conduction.

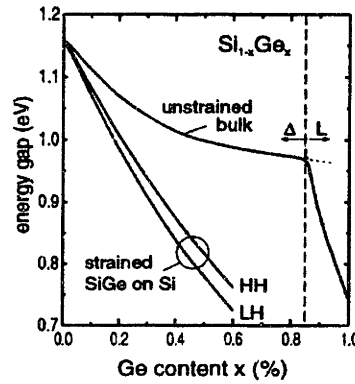


Figure 2.4: Band gap variation of $\text{Si}_{1-x}\text{Ge}_x$ alloys against composition [3].

Additionally, the addition of small amounts of Ge significantly impacts the growth rate. As Si is deposited, the H atoms from the Si precursor (SiH_4 or SiCl_2H_2) coat the wafer surface, slowing further Si growth. It is theorized that Ge facilitates H desorption from the surface, thus freeing more sites for Si deposition. This allows for the same film thickness to be grown in the same amount of time, but at a lower temperature (Figure 2.5).

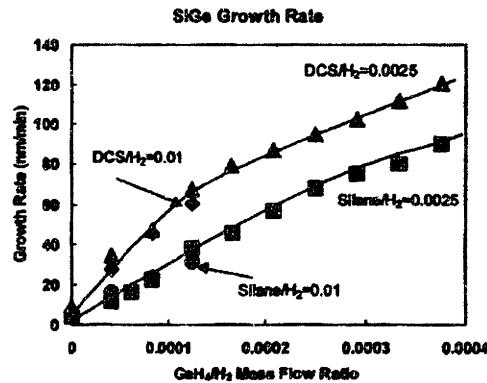


Figure 2.5: Increasing the Ge fraction strongly increases the growth rate [23]

The interstitial incorporation of Carbon acts to suppress the diffusion of Boron at high temperatures. B atoms move by an interstitial mechanism. An interstitial Si atom reacts with a substitutional B atoms to create a B/Si interstitialcy, where Si and B share the same site. This species is highly mobile, and moves rapidly through the lattice causing sharp junctions to broaden. The ion implantation of B creates excess Si

interstitials, which enhance B diffusion. C reduces B diffusion by acting as a trap for Si interstitials. This is desirable since the formation of well-defined electrical junctions in tiny devices requires that the dopant profiles do not shift during subsequent annealing steps [36]. One advantage that is particularly relevant to this thesis is the slight increase in the refractive index with increasing Ge fraction (Figure 2.9), and is discussed the next section. Table 2.1 summarizes several useful atomic parameters for the atoms common to Si epitaxy.

Table 2.1: Useful parameters of atoms common in Si epitaxy; shaded atoms are intentional electronic dopants [4], [12], & [13].

	Atomic Number	Atomic Mass (g/mol)	Atomic Radii (pm)	Dopant Type in Si	E_g (eV) $T=300K$	Diamond Lattice Parameter (Å)	Refractive Index $\lambda=1.55\mu m$
C	6	12.010	70	Isoelectronic	5.5	2.4640	-
Si	14	28.0855	110	Isoelectronic	1.12	5.4309	3.5
Ge	32	72.61	125	Isoelectronic	0.67	5.6575	4.25
[REDACTED]							
O	8	15.9994	60	n ⁻ type			

Section 2.2 Photonic devices and SiGe

Silicon has been the substrate of choice for microelectronics fabrication since the birth of the semiconductor industry. It is readily available in high purity crystalline wafers, and is a relatively inexpensive material that is easy to work with. Silicon-based microelectronics have shrunk in size and increased in speed at an exponential rate to handle the demands of higher performance, lower power consumption, and larger bandwidth. Future generations of telecommunications systems, however, demand extremely high-speed applications that push the performance limits of conventional microelectronic circuitry, stimulating their replacement with optical components. The number of hosts on the Internet, a measure of the volume of information, has steadily increased at an exponential rate since 1991 to over 130million, and this trend is expected to continue for the foreseeable future [20]. The current telecommunication system is strained to keep pace with this tremendous growth. Although the backbone of the Internet is comprised of high-bandwidth optical fibers, there are still places where the interface between the electrical and optical transmissions acts as a bottleneck. The “last mile” of data transmission between individual end-users to the Internet, and data switching of optical fibers for metropolitan

telecommunication networks are two very relevant examples. Replacing the current electrical/optical hybrid network with an all-optical network would significantly enhance data transmission speeds and increase network bandwidth.

An optical waveguide is a photon conduit with a higher index core surrounded by a lower index cladding that functions much like an optical fiber, but is manufactured directly on a wafer substrate. Planar waveguides are already common components in optical communication systems, though they suffer from large signal attenuation. Waveguides may be passive elements, serving only to transfer a signal from emitter to detector, or may be active elements which split, combine, and switch signals in response to an electrical or optical stimulus. The final goal is to integrate the waveguide into an optical circuit with emitting diodes, detectors, and couplers to interface with optical fibers (Figure 2.6).

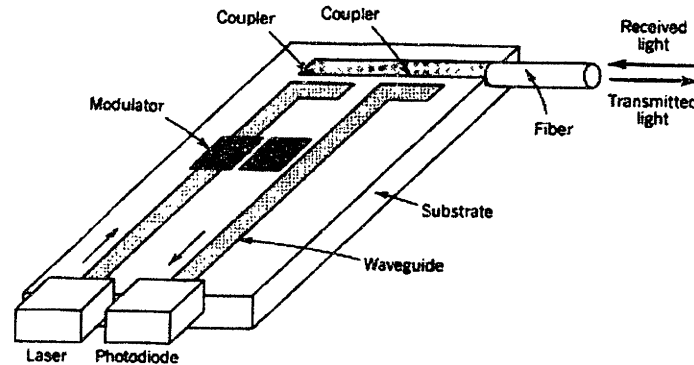


Figure 2.6: An integrated optical system [24]

One particularly attractive application of waveguide circuitry is the array waveguide grating (AWG). An AWG, also called an optical waveguide router or waveguide grating router, is a device capable of routing many optical signals from by their wavelength (Figure 2.7).

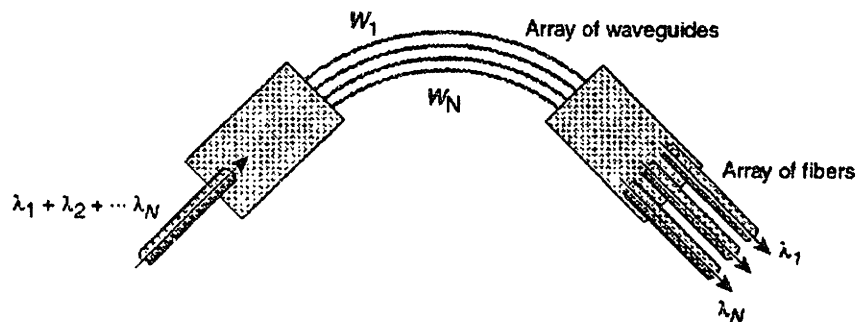


Figure 2.7: Arrayed waveguide grating [25]

AWGs are based on diffraction principles. An AWG consists of an array of curved-channel waveguides with a fixed difference in the path length between adjacent channels. The waveguides are connected to cavities at the input and output, so that when light enters the input cavity, it is diffracted as it enters the waveguide array. There, the optical length difference of each waveguide causes phase delays in the output cavity, where an array of fibers is coupled. The process results in different wavelengths having maximum interference at different location, which correspond to the output ports. The AWG switch has several advantages intrinsic to its all-optical nature. Since the AWG switch is completely passive and static, there is no power consumption and the likelihood of failure is reduced as compared to electronic switches. The throughput of the switch is limited only by the number of channels multiplied by the modulation data rate. Workers in the field have demonstrated a 12.5Gb/s data rate with a typical 80x80 AWG to achieve 1Tb/s packet switch rate, which the potential scalability to 128Tb/s [10]. It is necessary to minimize crosstalk between the different channels and to reduce the losses associated with insertion from the laser into the waveguide.

In this work, the feasibility of fabricating passive strip-waveguide structures using an LPCVD chamber was investigated. The waveguide design under investigation includes a square cross-section SiGe core surrounded by a Si cladding (Figure 6.1 on page 76). Fabricating waveguides using SiGe is a particularly attractive solution since both optical and electronic devices can be easily integrated on a single silicon substrate. This design capitalizes on the widespread availability of high quality, low cost silicon substrates. The optical properties of SiGe, particularly the refractive index, can be increased by increasing the Ge concentration (Figure 2.9 & Equation 6.17 on page 83). Furthermore, since Si and SiGe are transparent to infrared light, they can easily transmit the 1.3 μ m and 1.55 μ m wavelengths already employed in optical fiber telecommunications with low material absorption. The energy band gap of Figure 2.4 can be viewed as describing an optical band gap by using:

$$\lambda_r (\mu m) = \frac{1.24}{E_g (eV)}$$

Equation 2.3

Quantum mechanics state that photons of wavelength, λ , also have energy of $E=h/\lambda$, where h is Planck's constant (6.626x10⁻³⁴J/s). Photons incident on a material create electron-hole pairs, if their energy

is greater than the energy band gap, E_g , or if their wavelength is less than the λ_g . This is the principle of photodetection and is used for detecting light, because the electron-hole pair increases the conductivity of the exposed material. The energy band gap values in Table 2.1 can be translated into the optical band values of $\lambda_g(\text{Si})=1.107\mu\text{m}$ and $\lambda_g(\text{Ge})=1.85\mu\text{m}$. In an analogous fashion to the increase energy band gap, this parameter can also be increased by alloying with Ge.

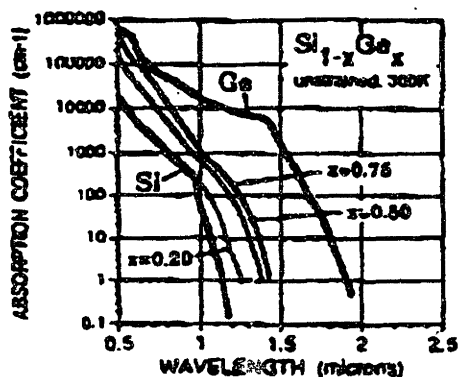


Figure 2.8: Absorption co-efficient versus wavelength for Si and Ge.

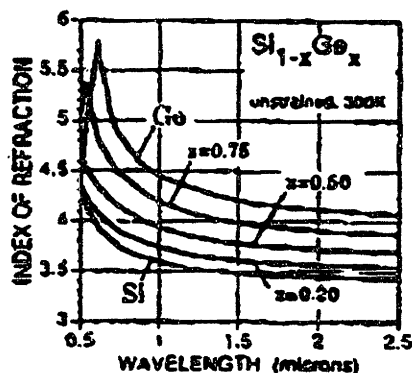


Figure 2.9: Dispersion of refractive index for Si, Ge, and SiGe alloys of Figure 2.8 [32]

Although SiGe structures have many advantages for optical applications, fabrication of useful structures requires overcoming several challenges. Firstly, there is the issue of lattice mismatch: the lattice constant of Ge is 4.16% larger than for Si. Since the SiGe core of the waveguide is surrounded by Si, this strain is accommodated primarily in the core region. The Ge concentration and core thickness must be chosen such that the structure does not have many dislocations in the core to increase the optical losses. Secondly, the growth of SiGe films is known to increase the incorporation of contaminants in the film. Impurities, especially elemental oxygen, act as optical scattering points, increasing material absorption.

To understand the connection between Ge fraction and refractive index, the following model is presented from [42]. Two assumptions are made in this model. First, it is assumed that the Si strain-optic tensor is equal to that of Si with small amounts of Ge, so the Si tensor is used. Second, it is assumed that there is no strain at all in the Si cladding. While both of these assumptions are somewhat unrealistic, relaxing them significantly complicates the model.

In the SiGe core there is an in-plane biaxial stress such that $\sigma_1 = \sigma_2$, where σ is the stress tensor, and 1, 2, and 3 refer to the principal axes of the crystal ($\sigma_3=0$). The lattice mismatch between Si and Ge is 4.16%, so the strain $\epsilon_1 (= \epsilon_2)$ is $\epsilon_1 = -0.0416x$. The strain is related to the stress by the compliance tensor, S_{ij} :

$$\varepsilon_i = S_{ij} \sigma_j$$

Equation 2.4

Therefore, the relationship between ε_1 and ε_3 is

$$\varepsilon_1 = \varepsilon_2 = (S_{11} + S_{12})\sigma_1,$$

Equation 2.5

$$\varepsilon_3 = 2S_{12}\sigma_1 = \frac{2S_{12}\varepsilon_1}{S_{11} + S_{12}}$$

Equation 2.6

since in the compliance tensor for Si, $S_{13}=S_{23}=S_{12}$. Substituting the numerical values $S_{11}=0.7691 \times 10^{-12}$ cm²/dyne, and $S_{12}=-0.2142 \times 10^{-12}$ cm²/dyne into Equation 2.6 gives $\varepsilon_3=-0.772\varepsilon_1$. The dielectric permeability tensor, B , and the strain-optic tensor, p , relate the strain to the refractive index. p relates the strain in the crystal to a change B :

$$\Delta B_i = p_{ij} \varepsilon_j$$

Equation 2.7

The change in refractive index is then derived from the dielectric permeability tensor

$$\delta n_i = -0.5n^3 \Delta B_i$$

Equation 2.8

The coefficients for the strain-optic tensor are $p_{11}=-0.094$, $p_{12}=0.0017$, and $p_{44}=-0.051$ [43]. Using $n_{\text{SiGe}}=3.52$, from Equation 6.17 for 2% Ge, and Equation 2.8,

$$\delta n_1 = \delta n_2 = 1.965\varepsilon_1, \text{ and}$$

Equation 2.9

$$\delta n_3 = -2.325\varepsilon_1$$

Equation 2.10

The strain-induced refractive index changes for the transverse electric (TE) and transverse magnetic (TM) guided fields are given by δn_1 and δn_3 , respectively. Substituting for the value of ϵ_j , as a function of Ge fraction, x ,

$$\delta n_{TE} = -0.080x, \quad \delta n_{TM} = 0.095x$$

Equation 2.11

or,

$$n_{TM} - n_{TE} = 0.0175x$$

Equation 2.12

Equation 2.7 explains why adding Ge to the Si lattice, which increases the strain, causes a change in the refractive index. Equation 2.12 goes further to show that since this strain is not symmetrical, the refractive indices in the in-plane and perpendicular directions are not the same. This condition gives rise to *birefringence* for the guided modes in the SiGe core. It implies that the TM mode is more tightly bound ($n_{TM} > n_{TE}$ therefore TM experiences a larger index contrast with the cladding) than the TE mode. The SiGe/Si system exhibits significant birefringence, so this should be accounted for when designing devices that make use of both polarizations of light. The effects of birefringence do not affect the present work on passive waveguide because only the transverse electric field is utilized. The appendix of **Section 10.2** may prove instructive for newcomers to electromagnetism.

A process flow for waveguide fabrication is given in **Figure 6.11** on page 92 that includes multiple blanket depositions of uniform and graded compositional layers on bare Si substrates. The useful structures are then formed by patterning and etching, but it is also possible to form these structures by selective deposition of on pre-patterned substrates. In this application, the regions for formation of the waveguides would exist as Si windows surrounded by a patterned oxide layer, and the selective deposition would occur only on the Si surfaces. The oxide regions would then be stripped by away by an HF dip.

Table 2.2: Important Waveguide Structural Parameters. Compare with Table 6.1 on page 82.

Structural Parameter	Aspects	Effect
<i>Point defects</i>	- Impurities - Vacancies - Interstitials	Variable effects in active devices Most often a source of scattering in waveguides
<i>Line/Area defects</i>	- Dislocations - Grain boundaries	Extra plane of atoms refract light Strongly dependent on crystallographic orientation Induce surface roughness
<i>Strain</i>	- Birefringence - Relaxation	Birefringence distorts electric field vs. magnetic field in electromagnetic wave Relaxed structures do not have strain, and hence no birefringence
<i>Composition</i>	- Lattice matching with Si - Ubiquity of Si	III-V optoelectronics cannot be epitaxially grown on Si Low-defect SiGe epitaxy is possible Economics of scale. Easy availability of low-cost, high quality Si wafers

Section 2.3 Microelectronic Devices and SiGe

Moore's Law summarizes the remarkable growth of the semiconductor industry: the density of transistors on an integrated circuit will double every 18 months. A transistor is a versatile switching and amplification device that is used as the basis for logic gates, memory storage, linear op-amps, rectifiers, and laser diodes. The 2GHz Intel Pentium 4 Processor released August 2001 has 42 million transistors [7]. Milestones in the semiconductor industry are measured as the minimum feature size of a single transistor; Pentium 4 is 0.18 μm -technology [7]. Transistors can be built in two ways: field-effect transistors (MOSFETs) or bipolar transistors (HBTs). The design, technology, and operations of these two important transistor types are presented, with focus given to the uses of SiGe to improve their performance.

Sub-Section 2.3.1 MOSFETs

The Metal-Oxide-Semiconductor Field-Effect Transistor (MOSFET) is the dominant transistor technology used in the semiconductor industry today. It is commonly used in the dynamic random access memory (DRAM) cell, which incorporates a charge storage element (a capacitor or *pn* junction) and a MOSFET as a switch in logic devices. DRAM cells are fabricated by the millions on today's integrated

circuits-“The 1-T DRAM cell is the most abundant man-made object on this planet earth” [26]. The MOSFET has a simpler geometry than HBTs. It can also be more easily fabricated at smaller dimensions, for greater density. A MOSFET consists of doped source and drain islands, which are electrically isolated from the oppositely doped substrate by reversed-biased p-n diodes. In the p-channel MOSFET shown in Figure 2.10 below, the dominant charge carriers in the channel are holes moving from source to drain (electrons are the dominant carriers in n-channel MOSFETs). A gate electrode, separated by an insulator, covers the region between source and drain, and controls whether the transistor is on or off. When the MOSFET is inversion biased ($V_G > V_{\text{threshold}}$), an inversion layer, or channel, is formed beneath the gate. By applying a positive voltage to the drain (V_D), current is made to flow in the channel to the source (I_D); the magnitude of this current is then regulated by the channel created by the gate voltage (V_G). CMOS means “complementary MOS” which refers to the combination of n-channel and p-channel MOSFETs working in tandem to make an inverter, or logical NOT gate. CMOS circuits are commonly used in logic circuits because of their low power consumption and symmetry of design.

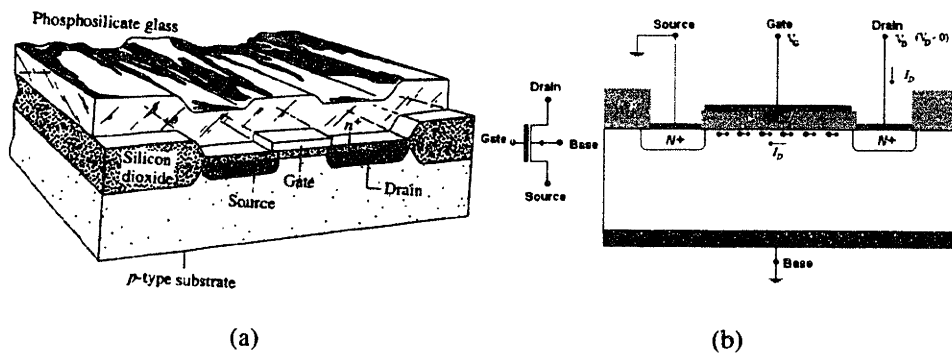


Figure 2.10: The basic MOSFET structure. (a) Idealized cut-away view of a p-channel MOSFET and corresponding circuit symbol. (b) Simplified cross-sectional view showing the terminal designations, carrier and current flow directions, and standard biasing conditions

Keeping pace with Moore’s law leads to increasingly shallow source and drain junctions to avoid unnecessary short channel effects. Short channel effects occur when the depletion regions surrounding the source and drain consumes the majority of the channel region under the gate, thus diminishing the effectiveness of the gate to control current flow. Making shallow junctions minimizes short channel effects because their geometry reduces the junction area near the channel. To electrically contact to these shallow junctions a thin layer of metal (Ti, W, Pt, or Ta) is sputtered onto the source and drains, and then reacted in

a rapid thermal-processing step. This silicidation reaction consumes some of the source/drain silicon. Though small, this fraction accounts for more and more of the total junction thickness as the transistor size shrinks. The silicide contact thickness has also been decreased to minimize leakage current from the proximity of the silicon/silicide contact to the channel region. However, the popular self-aligned silicide process (SALICIDE), which is reliably used to produce uniformly thin silicide layers without excessive increases in sheet and contact resistance, limits contact scaling. The combination of a thin silicide contact and a shallow junction increases the parasitic series resistance of the device. Parasitic resistance refers the capacitive impedance caused by time-varying electric fields within the device. The International Technology Roadmap for Semiconductors suggests that the parasitic resistance should account for less than 10% of the channel resistance for the 0.1 μm -technology and below [1].

The “elevated source/drain” (ESD) technique involves raising the level of the source and drain by selective epitaxial growth (SEG) on these junctions (Figure 2.11).

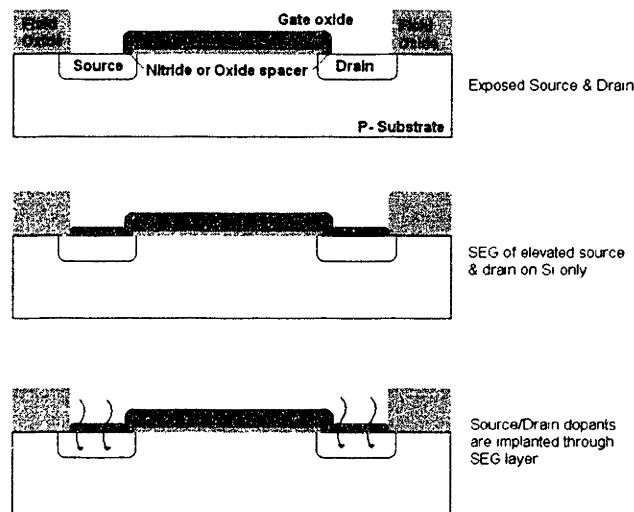


Figure 2.11: Extended Source/Drain to produce shallow junctions

The ESD technique is capable of fabricating well-defined source and drain regions while also providing a sacrificial layer for silicidation consumption. ESD increases the process margin for silicidation while providing extended latitude for contact junction design. Together, these advantages result in lower parasitic resistance in the device and reduced source & drain junction leakage. Ge is added to increase

dopant incorporation, lower the sheet resistance, and decrease the thermal budget due to increased growth rate [2].

Sub-Section 2.3.2 HBTs

A bipolar junction transistor (BJT) is the second most common transistor technology, but is dwarfed by the number of CMOS devices produced. An HBT is a common case involving different semiconductors (*heterojunction transistor*). HBTs find major application in telecommunications where high frequencies or low powers are needed. A BJT is a 3-terminal transistor device comprised of 2 PN junctions. The PN junctions can be arranged in the N^+PN or P^+NP configuration, of which the former is more prevalent (Figure 2.12). Bi-CMOS circuits combine the high-frequency performance of HBTs and the logic functions of CMOS devices.

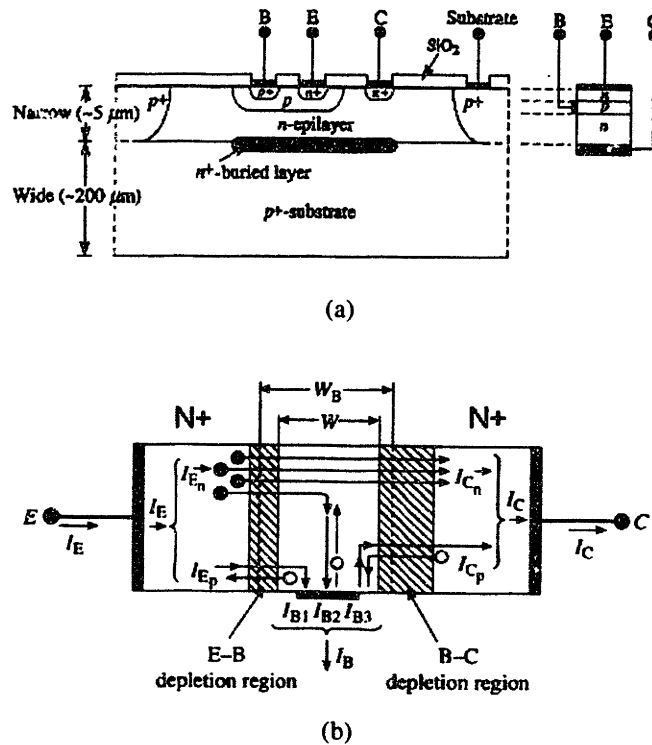


Figure 2.12: (a) the basic N^+PN BJT physical structure
(b) spatial visualization of diffusion currents under active mode biasing [6]

HBT circuitry involves a common emitter, such that current is applied to the base (I_B) and voltage is applied across the emitter and base (V_{EB}); output current is from the collector (I_C) and the output voltage is across the emitter and collector (V_{EC}). Under normal operation (active biasing), E-B junction is forward-biased and the C-B junction is reverse-biased. Electrons are injected from the emitter into the base, where they diffuse across the quasineutral base to the C-B depletion region where the accelerating electric field sweeps them into the collector. Once in the base, these electrons are the minority species, subject to recombination with holes. The fraction of minority carriers injected into the base, I_{En} , that successfully diffuse across the base region to enter the collector, I_{Cn} , is known as the *base transport factor* (α_T).

$$\alpha_T = \frac{I_{Cn}}{I_{En}}$$

Equation 2.13

The d.c. gain, α_{dc} , of the transistor is directly affected by recombination events

$$\alpha_{dc} = \gamma\alpha_T$$

Equation 2.14

$$\text{, where } \gamma = \frac{I_{En}}{I_E}$$

Equation 2.15

The emitter efficiency, γ , can be viewed as the emitter current that is composed of electrons moving from emitter to base divided by the total emitter current. $1 - \gamma$ is equal to the emitter current contributed from holes injected from the base back into the emitter divided by the total emitter current. In the ideal N⁺PN HBT, the emitter current is dominated by electrons traveling from emitter to collector ($\gamma=1$) and there should be not be any holes injected back into the base.

In SiGe NPN HBTs, a thin pseudomorphic SiGe layer is the base region because its bandgap is less than that of Si, with the major offset in the valence band. Since holes are the majority species in the base, the valence band offset prevents them from moving from the p-doped SiGe base back into the n-doped emitter. The electron current gain of NPN HBTs increases because of the decrease of holes being injected in the reverse direction (from base into emitter) Equation 2.14 and consume electrons.

Maximum BJT amplification occurs when α_T is unity, but recombination in the quasineutral base decreases I_{Cn} , and hence lowers the base transport factor. Recombination in the base is measured in terms of the *minority carrier lifetime*, defined as the average length of time a minority carrier will exist in a sea of majority carriers before a recombination event occurs. Grading the Ge concentration through the base layer in HBT structures, in which the Ge concentration increases with distance from the emitter interface, causes the band gap to vary spatially in the base, producing a drift electric field. This field serves to accelerate electrons to their saturation velocity, giving SiGe HBTs the highest operating frequency of any Si bipolar device. Adding large amounts of Ge increases the strain, so this epitaxial layer must be kept extremely thin, (200 to 300Å), to avoid exceeding the critical thickness. Additionally, since the amount of Ge in the base is graded in a triangular composition profile, there is no massive heterojunction effect at the emitter base region since there is not an abrupt Ge increase from the emitter to the base. This high-frequency performance can be traded for lower power consumption, depending on the application.

To improve carrier concentration, the base layer is also heavily doped ($>10^{19}\text{cm}^{-3}$ Boron), but preserving this sharp doping profile has challenges. Dopant diffusion is a thermally-activated process (Equation 2.17), which as a result of subsequent high temperature processing steps can lead to profile broadening. It will be shown in **Sub-Section 5.3.1** that adding small amounts of C limits the diffusion of B. Adding C is also shown to increase the critical thickness (**Sub-Section 5.3.2**), however adding too much C has deleterious effects. Firstly, adding too much C will cause SiC precipitates to form. Secondly, adding C actually increases the band gap, thus counteracting some of the effects of adding Ge. Clearly, the fractions of Ge and C must be balanced to achieve an optimum structure.

Non-selective SiGe deposition is used in the fabrication the base contact, both the base region itself and the base electrode are formed simultaneously, the former being epitaxial, and the latter is polycrystalline because it formed over oxynitride insulator (Figure 2.13). If the film is not continuous from the epitaxial base region to the polycrystalline electrode, necking and islanding might occur causing problems with the electrical contact. It is also desirable to have this film as smooth as possible to avoid problems when performing the subsequent photolithography steps necessary to form the emitter.

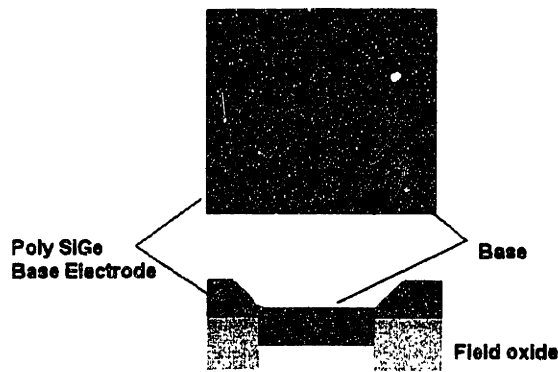


Figure 2.13: Simultaneous deposition of epitaxial base contact and polycrystalline base electrode

Section 2.4 Basics of Chemical Vapor Deposition

Chemical vapor deposition (CVD) is the preferred production method for the deposition of high quality epitaxial thin films. CVD chambers come in many flavors: Batch or Single wafer reactors, Cold-walled or Hot-walled CVD, Atmospheric-Pressure, Low-Pressure or Ultra-High Vacuum CVD, and even Metal-Organic CVD and other chambers that use exotic precursors, etc. The Epi Centra® is a single-wafer, low-pressure, cold-walled chemical vapor deposition (LPCVD) reactor that uses standard Si and Ge precursor gases. The basic processes of chemical vapor deposition are presented in this section as a context for the experiments described later.

In the CVD process, reactant gases are introduced into the chamber, where they undergo chemical reactions to form a non-volatile solid that deposits atomistically on the substrate (Figure 2.14).

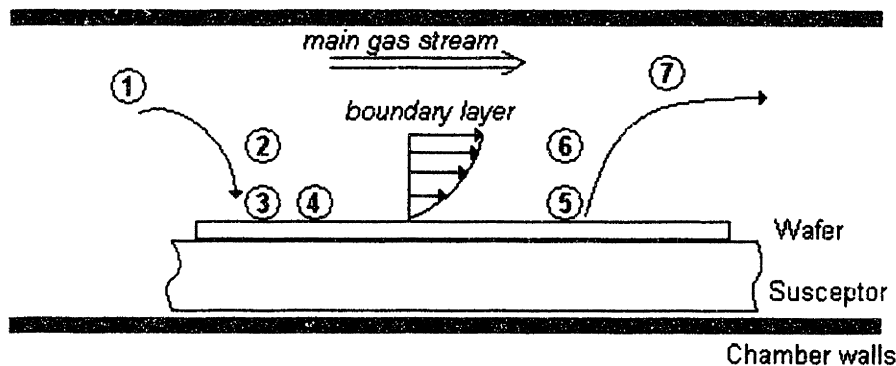


Figure 2.14: CVD Processes: (1) Reactant transport to wafer region; (2) Reactant diffusion through boundary layer to wafer surface; (3) Reactant adsorption on surface; (4) Reactant decomposition and diffusion along surface; (5) Desorption of reaction byproducts from wafer surface; (6) Byproduct diffusion through boundary layer; (7) Byproducts exit the system via exhaust

The important steps in this process are:

1) *Transport of reactants to wafer region by forced convection*

Source gases are introduced to the chamber via a complex inject manifold system that endeavors to deliver a uniform flow rate across all points on the wafer. Owing to the circular geometry of 200mm wafers, the wafer is rotated to further increase uniform deposition. This rotation distorts the laminar flow from inlet to exit producing a whirlpool-like effect. Accommodations are made in chamber design to account for these effects.

2) *Diffusion of reactants through the boundary layer to the wafer surface*

The Navier-Stokes' equation of momentum conservation predicts the existence of a boundary layer, of thickness δ , of decreasing velocity in the flowing gas above the wafer:

$$\rho \frac{Dv}{Dt} = -\nabla P + \eta \nabla^2 v + \rho g$$

Equation 2.16

Within this boundary layer, the velocity is only in the direction parallel to the wafer; the material flux diffuses according to Fick's First Law:

$$F_{diff} = -D_g \frac{\partial C(x,t)}{\partial x} = \frac{D_g}{\delta} (C_g - C_s)$$

Equation 2.17

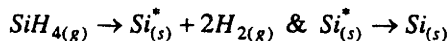
D_g is the diffusion coefficient of the reacting species across the gas phase boundary layer, C_g and C_s are the concentrations of the growth species in the gas and on the surface of the wafer, respectively.

3) *Adsorption of reactants onto the surface*

Once at the wafer surface the reactants must have sufficient energy to "stick" – reactants that do not stick may "re-emit" and deposit on trench sidewalls causing coverage issues.

4) *Decomposition of reactants and diffusion of reaction products along surface*

A common route for Si epitaxy involves the following reaction:



Equation 2.18

The energetic Si atom moves along the surface until it finds a lattice location at an atomic-level ledge or kink and becomes part of the growing film. The rate of source species consumed, F_{rxn} , follows the simple first-order rate law:

$$F_{rxn} = k_s C_s$$

Equation 2.19

where k_s is the chemical surface reaction rate (=[cm/sec). The reaction rate is a thermally-activated property that increases exponentially with temperature, so precise control of wafer-surface temperature is important (Equation 2.22).

5) *Desorption of reaction byproducts from surface*

The reaction byproducts leave the wafer surface. Incomplete desorption can prevent further adsorption of incoming species by occupying lattice sites leading to poor coverage.

6) *Diffusion of byproducts through the boundary layer and back into the main stream*

This movement also follows Fick's First Law in Equation 2.17 except D_g , C_g , and C_s are values for the product species.

7) *Transport of reaction products to exhaust*

A negative pressure facilitates the rapid removal of byproducts from the process chamber through the exhaust manifold to the scrubber equipment to be quenched and neutralized.

The Deal model is the simplest model used to describe growth from the vapor phase. The flux of the deposition species across the boundary layer, F_{diff} (=[molecules cm⁻² s⁻¹), is equated to the flux of reactant consumed by the growing surface, F_{rxn} [8]:

$$F_{diff} = h_g (C_g - C_s) = k_s C_s = F_{rxn}$$

Equation 2.20

The mass transport coefficient is a function of the diffusivity through the boundary layer and the boundary layer thickness,

$$h_g = \frac{D_g}{\delta}$$

Equation 2.21

The temperature dependence of the surface reaction rate follows the Arrhenius law:

$$k_s = k_0 e^{\left(\frac{-E_s}{kT}\right)}$$

Equation 2.22

where k_0 , E_s , k , and T are the reaction constant, activation energy, Boltzmann's constant, and temperature, respectively.

It can be shown that

$$C_s = C_g \left(1 + \frac{k_s}{h_g}\right)^{-1}$$

Equation 2.23

and that the growth rate, R ([=] $\mu\text{m}/\text{min}$) is

$$R = \frac{k_s h_g}{k_s + h_g} \left(\frac{C_g}{N}\right) \text{ or } R = \frac{k_s h_g}{k_s + h_g} \left(\frac{C_i}{N}\right) Y,$$

Equation 2.24

$$\text{where } Y \equiv \frac{C_i}{C_T}$$

Equation 2.25

N is the number of atoms incorporated per unit volume of the film ($5 \times 10^{22} \text{ cm}^{-3}$ for Si), C_T is the concentration of all molecules in the gas phase ([=] cm^{-3}), Y is the mole fraction of the incorporating species in the gas phase. From Equation 2.7, it can be seen that the growth rate is determined by the smaller of k_s or h_g , which leads to two limiting cases. If $h_g \ll k_s$, then

$$R = h_g \left(\frac{C_g}{N}\right)$$

Equation 2.26

and film growth is *limited by the mass transfer* across the boundary layer and is strongly dependent on the flow conditions in the chamber. The surface reaction rate is, therefore, much faster than the mass transfer rate through the gas boundary layer. If, instead $k_s \ll h_g$, then

$$R = k_s \left(\frac{C_g}{N} \right)$$

Equation 2.27

and growth is *limited by the surface reaction rate* and is strongly dependent on the wafer temperature. In this case, the surface reaction rate is sluggish compared to the mass transfer rate and therefore dominates the growth rate. Figure 2.15 shows both of these regimes for Si deposition.

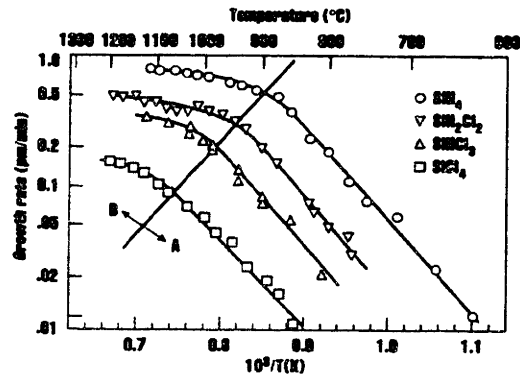


Figure 2.15: “Classic” plot of the regime transition [13].
 (A) Reaction-rate limited regime; (B) Mass flow-limited regime.
 This should be compared with Figure 4.1 on page 44.

Reducing the pressure in the gas stream increases the boundary layer diffusion and extends the reaction-controlled regime to higher temperatures (Figure 2.16). Equation 2.24 can also be written as

$$R = \frac{k_s h_g}{k_s + h_g} \left(\frac{C_T}{N} \right) \frac{P_g}{P_T}$$

Equation 2.28

where P_g and P_T are the partial pressure of the species in the gas phase and total chamber pressure, respectively. The diffusivity in Equation 2.17, is inversely proportional to the total pressure,

$$D_g \propto \frac{1}{P_T}$$

Equation 2.29

Lowering the total pressure reduces the total concentration of gases in the main stream but does not by itself decrease the concentration of the reactant gases, so D_g increases. For example, reducing from atmospheric to 1 Torr increases D_g by 760 times while increases the d by 3-10 times, causing a net increase

in h_g by 100 times. Since h_g is much larger, the mass transport rate through the boundary layer becomes less influential than the surface reaction rate in determining the overall deposition rate, thus extending the temperature-controlled regime (Figure 2.16).

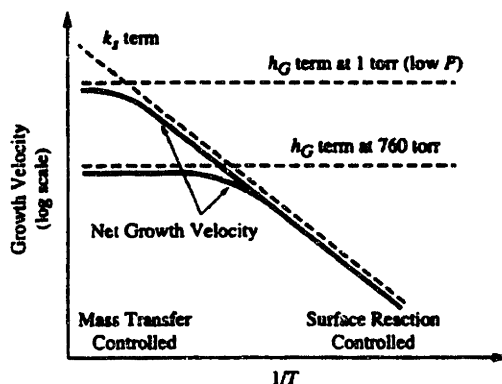


Figure 2.16: Growth velocity vs. $1/T$ for atmospheric and reduced pressure conditions. The lower total pressure (with P_g and C_g remaining fixed) shifts the h_g curve upward, extending the surface reaction regime to higher temperatures [11].

This overview is sufficient to familiarize the reader with the basics of the CVD process, though much of the important details have been omitted for brevity. Good sources of information on this high-throughput, industry-standard technique and its many permutations are available ([11], [12], & [13]).

In the next section, the particular LPCVD chamber on which the waveguides were fabricated is introduced.

Section 2.5 Applied Materials' Epi Centura®¹ LPCVD

In January 1993, Applied Materials released the Epi Centura® system, a Low-Pressure CVD single-wafer reactor specializing in the epitaxial deposition of low-defect Si, $\text{Si}_{1-x}\text{Ge}_x$, and $\text{Si}_{1-x-y}\text{Ge}_x\text{C}_y$ films that may be in-situ doped with B, P, or As. These films can be reliably deposited in thin layers of constant composition or graded structures of varying composition to maintain dislocation-free structures through programmable software recipes. The primary use of epitaxial films is as the intrinsic Si layer in device fabrication, but also finds special application in depositing strained SiGe for use in MOSFET and HBT

¹ Epi Centura® is a registered trademark of Applied Materials, Inc.

devices. These devices are used in applications requiring greater oscillation frequencies and/or lower power operation, such as high-speed wireless communications

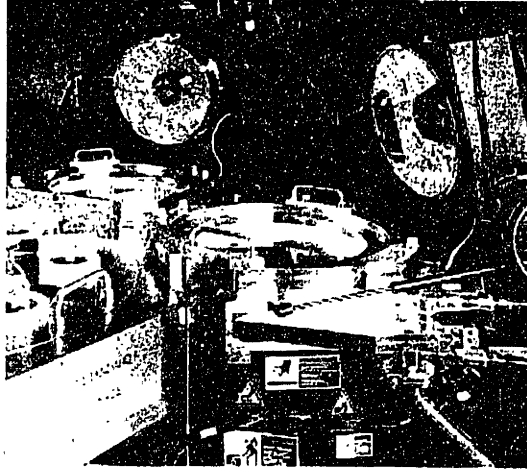


Figure 2.17: Epi Centura® LPCVD reactor

The process window for the Epi Centura® is broad; making it a versatile platform for a wide variety of experimental conditions (Table 2.3). The formation of SiGe electronic and photonic devices require high quality, dislocation free deposition. To form useful structures, the deposition is often done on patterned surfaces, or structures that will be patterned.

Table 2.3: Typical² conditions for low pressure processing

Pressure (Torr)	Temperature Range (°C)	Si source gases	Main/Slit H ₂ flow (slm)	Common Dopant gases
1-100	580-900	SiH ₂ Cl ₂ , SiH ₄ , SiHCl ₃	20-40/2-5	GeH ₄ , SiCH ₆ , BH ₄ , AsH ₄ , PH ₃

The LPCVD technique was chosen for its ability to deposit Si and SiGe films of uniform and controllable thickness. It allows for the precise management of the incorporated Ge fraction, which is necessary for controlling strain and index contrast. In addition, the low-pressure conditions reduce the contaminants incorporated in the films.

² All of these parameters are strongly dependent on the particular process.

Chapter 3 Metrology Tools

As can be seen from the brief overview in the previous chapter, the thickness and composition of thin films needs to be controlled with great precision on the nanometer scale. These metrics placed on the thin films create stringent chamber performance standards. As previously mentioned in **Section 2.4**, these tight metrics will, in turn, place tight specifications on the temperature control and flow of gases in the LPCVD chamber. A variety of metrology tools was used to characterize the wafers produced in the chamber. Without these tools, it would be impossible to determine if the thin films produced in the development stage were achieving the desired metrics demanded by the devices in the marketplace. An understanding of the physical processes that govern these techniques is invaluable in interpreting the results presented later. Presented in this chapter are brief descriptions of what these techniques measure and how measurements are made.

Section 3.1 XRD – Film Strain & Composition

X-Ray Diffraction (XRD) is an important technique for obtaining structural information on an atomic scale from both crystalline and amorphous materials. XRD is nondestructive and can be successfully applied to determine microstructures of metals and alloys for deriving such information as lattice strain, chemical composition, and crystallography. Monochromatic X-rays of a known wavelength are targeted at the sample, and by measurement of the reflected diffraction pattern of constructive and destructive interference the spacing between parallel atomic planes can be determined using Bragg's Law.

X-rays are moving oscillations of electric and magnetic fields-electromagnetic waves, whose wavelength is on the order of the interatomic spacing. If an electron happens to be in the way of this wave, it is forced to vibrate by the periodically changing the electric field of the x-rays. When oscillating in-phase, this electron becomes itself a source of an electromagnetic wave of the same frequency and wavelength as the original wave. By this interaction, the electron is said to scatter the original x-ray wave. X-rays are scattered by all the electrons of all the atoms in the surface layers of the material; hence, the scattering power of a certain atom depends on the number of electrons it has, i.e., on its atomic number. In crystalline samples, the atoms are regularly spaced in crystallographic planes; each of them scatters the

incoming wave individually, producing a new set of spherical waves. The combination of all these wavelets is diffraction. Bragg's Law states that the diffraction condition as

$$n\lambda = 2d \sin \theta$$

Equation 3.1

where d is the spacing between crystal planes, θ is the Bragg angle between the incident beam and the plane required for constructive interference, n is an integer, and λ is the wavelength (Figure 3.1).

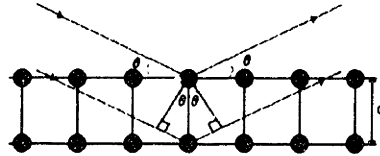


Figure 3.1: Bragg Diffraction

XRD was done using a Bede Scientific, Inc. X-Ray Diffractometer, which uses radiation emitted from the K_{α} transition in Cu, $\lambda=1.54056 \text{ \AA}$. For increased resolution, the Bede XRD employs double crystal X-Ray diffraction. The X-rays leave the source, and are reflected off a reference crystal to condition it before it impinges on the sample. To completely measure the strained state of an epilayer, comparison of the lattice constant parallel to and perpendicular to the substrate are needed. The (004) diffraction peak measures the spacing between planes perpendicular to the substrate (symmetric scan). If the thin film has a larger relaxed lattice constant than the substrate, but is completely strained, it will undergo biaxial compression. This biaxial compression causes a Poisson distortion extending the spacing perpendicular to the substrate. Thus, by measuring the strain in (004) direction one can determine the Ge concentration. The (115) diffraction peak measures the spacing between planes at an angle of 8.05° to the substrate (asymmetric scan). By comparison, of this spacing with the (004) spacing, one can determine the lattice constant parallel to the substrate. If the parallel lattice constant is equal to the lattice constant of cubic Si, then the film is completely strained.

XRD is therefore an indirect method for measuring dislocation densities. If the total misfit, f , is known and XRD measures the elastic strain, ϵ , Equation 2.1 can be used to calculate the plastic strain. It must be noted that for XRD measurements many dislocations must be present in the epilayer to generate a detectable amount of plastic strain. This means that XRD measurements should not be used to detect the onset of dislocation formation, and information about critical thickness gleaned from them tends to be

overestimated. Scanning luminescence techniques are able to detect single dislocations and should be used instead for precise measurements of h_r [16].

Atoms in a lattice may reside either on a lattice site, one of the positions shown in **Figure 2.3**, or in the spaces between those positions, substitutional and interstitial sites respectively. Dopant atoms residing on substitutional sites cause a measurable strain on the lattice—larger atoms cause the epitaxial lattice to be compressively strained while smaller atoms cause tensile strain. Since the $\text{Si}_{1-x}\text{Ge}_x$ system is completely miscible, the strain is directly proportional to the incorporated fraction of Ge.

The XRD software uses the separation between the substrate and SiGe peak to obtain the Ge concentration of the film. The further apart the film peak is from the substrate peak, the greater the strain. From the loci of the thickness fringes and the FWHM of the SiGe layer peak, the film thickness is calculated. If the film is completely pseudomorphic, with no dislocations, all the parallel crystalline planes refract the incoming X-rays at their Bragg angles, resulting in a well-defined constructive interference pattern. This pattern manifests itself as a sharp film peak, surrounded on either side by symmetrically spaced fringes. If the film is partially relaxed, or in the extreme, amorphous, the film peak broadens and the fringes as less intense, or absent all together.

Section 3.2 Ellipsometry – Thickness & Composition Uniformity

Ellipsometry is an optical technique that uses polarized light to probe the dielectric properties of a sample. Through the analysis of the change in polarization of the light that is reflected from the sample, ellipsometry can yield extremely accurate information about material and thin film optical properties. Depending on what is already known about the sample, the technique can probe a range of properties including the layer thickness, morphology, or chemical composition.

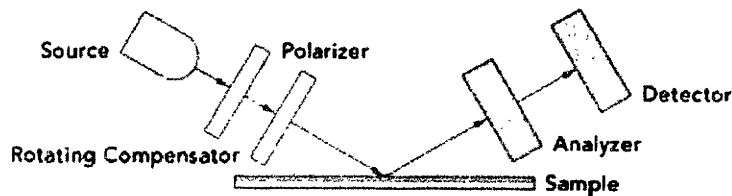


Figure 3.2: Ellipsometry apparatus

Spectroscopic ellipsometry, as opposed to single wavelength or multiple angle ellipsometry, adds the capability of simultaneous determination of multiple parameters: for example both thickness and composition of multilayer thin film stacks. Composition is calibrated against SIMS measurements on standard samples. Ellipsometers are generally used to measure thin films and complicated film stacks. Ellipsometry measurements in this thesis were performed using a NanoMetrics 8300XSE Ellipsometer.

Section 3.3 SIMS – Accurate Concentration Profiling

Secondary Ion Mass Spectrometry (SIMS) is a technique for producing high-resolution depth profiles of dopant and impurity elements in semiconductor samples. The detection limits are in the ppm to ppb range while the lateral spot size is about 100 μ m. Though the probed depth can range from thousands of angstroms to several microns, the resolution is often measured in nanometers. The precision of SIMS makes it a useful measurement for metrology equipment calibration, judging chamber performance and as a contrast with XRD, which measures only substitutional elements affecting lattice strain.

SIMS measures the mass and charge of ions of ejected from the sample by a primary sputtering beam of energetic ions or neutral beams. For semiconductor analysis, the primary beam is either energetic Cs or O ions in the keV range. Upon impact with the sample's surface, the primary beam ejects photons, electrons, neutral atoms, atomic clusters, molecules, and in small fraction, ionized species. These *secondary* ions are sorted first by a focused electrostatic analyzer and mass-filtered by a magnetic sector analyzer to determine the mass flux. After passing through the analyzers, the flow of ions is detected as a current, giving the charge flux. This mass/charge ratio is the element's signature. This data is recorded in real-time and is plotted versus a measurement of the depth taken by a stylus profilometer. It is common practice to raster the beam across the surface, but to detect only from a small circle in the center; this eliminates measuring atoms from the crater's walls.

An outside company that uses Quad HDR-SIMS, which has greater depth resolution 5 nm than ordinary SIMS, performed SIMS measurements. A table of conditions and measurement parameters is given in Table 3.1 below.

Table 3.1: SIMS Conditions and Measurement Parameters

Measurement Conditions		Detection Limits (atoms/cm ²)				Primary Ion Depth
Primary ions	Ion Energy	C	O	B	Ge	
Cs ⁺	2keV	1x10 ¹⁶	1x10 ¹⁷	7x10 ¹⁵	Matrix ³	1000s Å
	5keV	4x10 ¹⁶	8x10 ¹⁶	-	Matrix	Few microns

The accuracy of SIMS depth resolution is limited, among other factors, by the so-called “mixing effect.” This effect arises because high-energy ions push sample atoms deeper into the sample. These atoms are then ejected when the primary beam hits them more directly, however the system registers them as originated from an artificially deeper level. In order to reduce the mixing effect, lower beam energy can be used to produce depth profiles that are more accurate. Lower energy beams tend to be used on more shallow samples since the sputtering rate is less, whereas higher energy beams are used for thicker samples in order to decrease the measurement time. Using larger Cs atoms decreases the sensitivity of the scan compared to the lighter O atom because although the sputtering rate is higher, there is a greater tendency for atomic clusters to be removed from the surface (Figure 3.3).

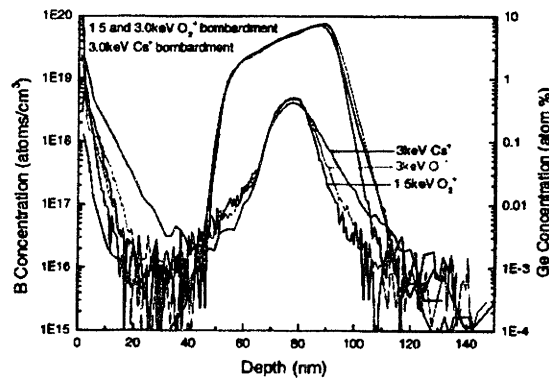


Figure 3.3: SIMS profiles obtained to show the “mixing effect”

It is therefore important to balance the desired sensitivity and the expected depth of the scan against the amount of time the scan takes; time which translates into extra cost for the analysis.

³ SIMS analysis uses a calibrated standard to compute the Relative Sensitivity Factor, which acts as a conversion between counts/sec to atoms/sec. Since changes in the analytical conditions during or between analyses may cause slight changes in an element’s RSF, comparison to the standard is necessary to give reliable results. The RSF for C and O do not change as much as for B and Ge, so archived RSF values are often used. The RSFs for B and Ge were computed by concurrent analysis of a B-doped Si and SiGe standard, respectively.

Section 3.4 FTIR – Film Thickness

Fourier Transform InfraRed (FTIR) spectroscopy is an accurate and quick method used to determine the thickness of an epitaxial film. FTIR is non-destructive and non-contact; it was most commonly used to measure the thickness profile of a wafer to determine deposition uniformity. The basis of FTIR is the detection of the refraction index contrast between different epitaxial film occurring in the infrared wavelengths. Silicon is transparent to infrared radiation, however the index of refraction depends on the free carrier concentration. Infrared reflectance from a lightly doped or intrinsic film on a heavily doped substrate shows interference patterns with fringes decaying towards higher frequencies. A model that is calculated from first principles is fit to the measured data (Figure 3.4). One of the fit parameters is the layer thickness.

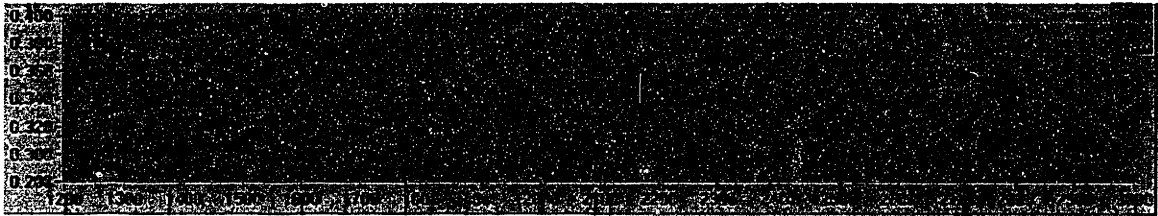


Figure 3.4: FTIR measured spectrum overlaid on model spectrum. This particular fringe pattern corresponds to a 4.232 μm thick epilayer of intrinsic Si on p⁺ substrate.

FTIR analysis was performed on an ADE EpiScan™ 1000 FTIR measurement tool. This tool can measure film thickness from 0.3 μm to 25 μm . It is capable of measurement repeatability $1\sigma \leq 0.008\mu\text{m}$ for 0.3-0.6 μm and $1\sigma \leq 0.004\mu\text{m}$ for 1.0-25 μm . Measurements are taken from a 6.0mm diameter spot on the wafer surface.

Section 3.5 AFM – Surface Roughness

Atomic Force Microscopy (AFM) is high-resolution technique for imaging a surface. The atomic force microscope includes a microcantilever with a fashioned stylus at the tip (Figure 3.5). The stylus point can be made from the (111) crystallographic planes of a Si lattice. The stylus is brought within close proximity to the surface and rastered across the sample. The cantilever responds to the electrostatic forces

on the sample's surface by undulating. This displacement can be detected in many ways; the simplest is by means of a targeting laser that is aimed at the cantilever head. The accuracy of the AFM tool is unmatched, being sensitive enough to discern individual atoms. For the measurements in this paper, the surface was probed in $2 \times 2 \mu\text{m}$ and $20 \times 20 \mu\text{m}$ squares. The AFM used was a Veeco™ DI7000.

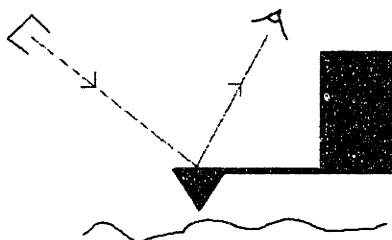


Figure 3.5: AFM principle of operation

The AFM produces a periodically varying signal, $s(t)$. Mathematically, the squared signal is $s^2(t)$ and the “mean squared” signal is the integral of $s^2(t)$ over an entire period divided by the period. The “root mean squared” (R_{ms}) is the square root of this value and provides a convenient way to characterize an “average” value of this varying signal. Roughness values are quoted in terms of their R_{ms} value.

Chapter 4 LPCVD Hardware Modifications

The continual development of the Epi Centura® LPCVD chamber has included countless design iterations, many of which were done before my personal involvement. My contribution has been to improve the ability of the chamber to fabricate waveguide structures through additional hardware modifications. Common electrical microcircuitry is fabricated on single dies, many to a wafer, and then diced into chips. For optical circuitry, it would be desirable to use the entire wafer surface for unit optical circuits. Large-scale systems, such as AWGs, can be used to route signals from many input optical fibers to many output fibers. The uniformity requirements are not that different for these systems. If the wafer is to be cut into dies, across-wafer uniformity is a goal to improve yield, but if the entire wafer is to be used, across-wafer uniformity must be achieved to have consistent waveguiding properties. The chamber must be able to deposit Si and SiGe films in uniform thickness, otherwise the waveguiding properties will be variable. The composition of the films must also be as even as possible across wafer surface. The index contrast of the waveguide is directly affected by the substitutionally incorporated Ge fraction. Impurities, such as O, in the core act as scattering points that increase waveguide loss, it also increases the free carrier concentration, which changes the refractive index. Control of the film microstructure is needed to produce low dislocation density epitaxial layers. Film strain causes birefringence in waveguides, distorting the electric and magnetic fields. Dislocations act as scattering planes if they exist in the waveguide core, but have little effect when in the cladding far from the core interface. They also increase surface roughness, which detracts from the transmission properties of the waveguide. To produce these high-quality films specialized hardware was installed to improve the gas flow and heating pattern. Gas purifiers were added to decrease the impurity levels in the chamber.

For a fabrication tool the full process space is defined by the extent the each physical knob can be turned and adjusted, but is most severely bound by three intertwined restrictions: cost, heat, and time. Achieving high throughput for a low thermal budget means balancing heat and time. The *thermal budget* for a process is the time-spent-at-temperature and the *thermal history* is the sequence of all thermal budgets to produce a finished device. Fortunately, the addition of Ge dramatically increases the growth rate, allowing Si depositions to be done at a lower thermal budget. The diffusion of atoms in a solid, and associated junction movement, and the thickness of a depositing film are both strongly dependent on time

and temperature. Thermal budgeting is, therefore, a paramount concern in planning a device process flow: higher temperature steps tend to precede lower temperature ones. From a developmental perspective, the time spent developing a product must be weighed against the fiscal advantage lost by delayed commercialization. For the following improvements, the process space available is not fully mapped, but rather particular conditions are selected and as few tests as possible are conducted that determine the optimum solution for a specific application as quickly as possible. The appendix in **Section 10.1** provides definitions for some of the terms used in the section.

Section 4.1 Achieving Uniform Chamber Conditions

IC manufacturers wish to minimize the thermal budget of epitaxial depositions in order to decrease diffusion of previously implanted dopants and prevent breaches in the shallow trench isolation that separates devices. Consequently, most LPCVD processes are done in the regime where growth rate is reaction rate-limited, and is a strong function of the surface temperature (**Figure 2.15** & **Figure 4.1**). The activation energy for GeH_4 is lower than for Si precursor gases, so GeH_4 decomposes easily so the Ge incorporation rate is strongly dependent on the local surface temperature. Uniform film thickness across the surface of the wafer therefore requires a corresponding uniformity in the heating of the wafer, so thickness profile is a direct measurement of the temperature profile in this regime. It is desirable to have thickness and compositional uniformity $1\sigma \leq 1\%$.

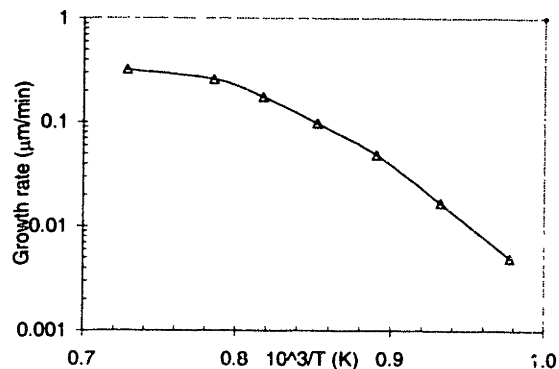


Figure 4.1: Empirically determined LPCVD growth rate data for 200slm SiH_2Cl_2 (DCS) 20Torr. This should be compared with **Figure 2.15** on page 33.

In this section, the effects of a 3-zone lamp module are explored to provide uniform heating. Flow uniformity is also achieved by changing the way process gases are introduced to the chamber.

Sub-Section 4.1.1 Temperature Calibration

Uniform heating across a 500 μ m-thick, 200mm-diameter wafer is plagued by three primary issues: uniform exposure, edge effects, and gas convection and conduction (Figure 4.2). For a finite array of heating lamps, the edge of the wafer receives less direct illumination and tends to be, on average, further from the lamp bank than the center. The edge of the wafer also has a greater un-illuminated surface area-to-volume ratio than the interior so more heat is lost to the ambient. Convective gaseous motion near the wafer surface acts to cool the edges more efficiently than the center.

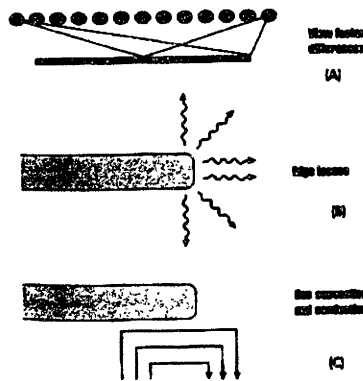


Figure 4.2: Causes of thermal non-uniformity include: (a) reduced view factor to the lamp array for large r , (b) very small view factors along the wafer edge, and (c) non-uniform gas phase heat transfer [13].

The chamber uses pyrometry to measure the temperature at the center of the wafer. Pyrometry is a non-contact optical technique that determines temperature, T , by the measuring the radiant energy at a particular wavelength, λ , emitted from the wafer surface, a gray body. Plank's radiation law gives the spectral radiant exitance, $M_k(T)$, as

$$M_k(T) = \varepsilon(\lambda) \frac{c_1}{\lambda^5 (e^{c_2/\lambda T} - 1)}$$

Equation 4.1

where $\varepsilon(\lambda)$ is the wavelength-dependent emissivity of the gray body, and c_1 and c_2 are the first and second radiation constants given by $3.7142 \times 10^{-16} \text{W}\cdot\text{m}^2$ and $1.4388 \times 10^{-2} \text{m}\cdot\text{K}$ respectively. Uncertainty in the

surface emissivity is a major source of uncertainty in pyrometric measurements. It is crucial that the measurement wavelength is selected to exclude reflected radiation from the lamps, hot gases, and chamber walls, while minimizing the effect of emissivity uncertainty on the temperature reading. Differentiating Equation 4.1 with respect to T , and assuming that M and λ are fixed, so $e^{c_2/\lambda T} \gg 1$, gives:

$$\frac{dT}{T} = -\frac{\lambda T}{c_2} \frac{d\varepsilon}{\varepsilon}$$

Equation 4.2

For a given wafer temperature and a 1% uncertainty in the emissivity value, a pyrometer receiving at a higher wavelength produces a greater temperature uncertainty than one receiving at a lower wavelength.

An alternative method for measuring temperature is by thermocouple. A thermocouple operates by the Seebeck effect that states that the junction between two metals generates a voltage that is a function of temperature. Through a cold junction, a voltmeter is used to measure this voltage. For standard thermocouples, tables exist which convert this voltage to a temperature. Pyrometry is preferred over thermocouple temperature measurement for many reasons. The thermocouple must be in physical contact with the wafer or susceptor and this causes heat loss through the contact point. Thermal impedances induced by the point contact result in a substantial temperature difference between the thermocouple and contact point. Reactions between the thermocouple and the contact point contaminate the chamber and can lead to drift in the characteristics of the thermocouple. Finally, introducing the thermocouple leads disturbs the flow pattern in the chamber. However, obtaining accurate pyrometric readings are not without problems. In addition to emissivity concerns, the thickness of the thin windows, which shield the sensitive pyrometric device from the heated process gases, must be accurately known to account for attenuation. Furthermore, these windows may become coated during deposition cycles thus changing their transmission properties. Absorption in the near-IR by the chamber gases, which is a function of temperature, pressure, composition reduces the apparent temperature of the wafer. For these reasons, pyrometers are calibrated using thermocoupled-wafers.

The pyrometers were calibrated by using a special wafer with 9 standard Type K (chromel-alumel) thermocouples bonded to its surface along the diameter, each 2.2 cm apart as shown in Figure 4.3. The thermocouples are connected to wires that extend from inside the process chamber to a multichannel digital

meter. Type K thermocouples have a sensitivity of $41\mu\text{V}/^\circ\text{C}$ in the -200° to 1200°C range, and have a resolution of 0.025°C in the -20 to 1150°C range.

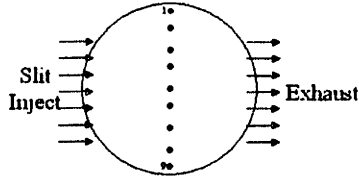


Figure 4.3: Orientation of thermocoupled wafer in process chamber

Using this thermocoupled-wafer, the local temperature on the wafer can be accurately measured under different heating and flow conditions. Emissivity values were determined as the factor needed to match the pyrometer measurement to the center point thermocouple measurement. Of course, since the thermocouple wires are bonded to the wafer, the wafer is not rotated, nullifying the beneficial averaging effect this has during actual deposition. Process gases are not introduced because of the damage it would cause to the thermocouples.

At different lamp powers, the intensity at the receiving wavelength changes causing the intensity received by the pyrometer to also change. The functional dependence of the emissivity on the delivered lamp power is given in Figure 4.4.

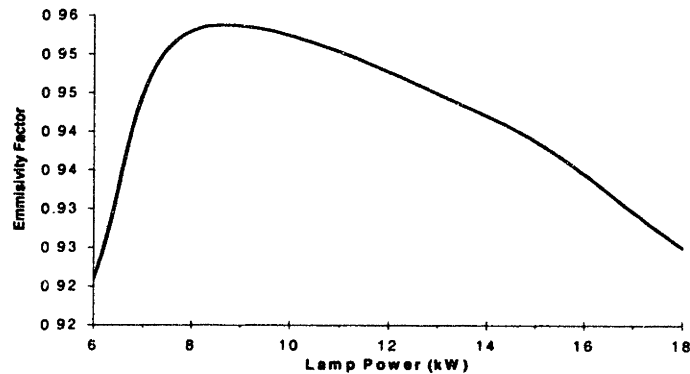


Figure 4.4: Lower Pyrometer Calibration (20Torr)

The center point temperature expectedly increases with delivered lamp power (Figure 4.5). This is a very useful plot because it allows the process engineer to obtain a specific wafer temperature by changing lamp power.

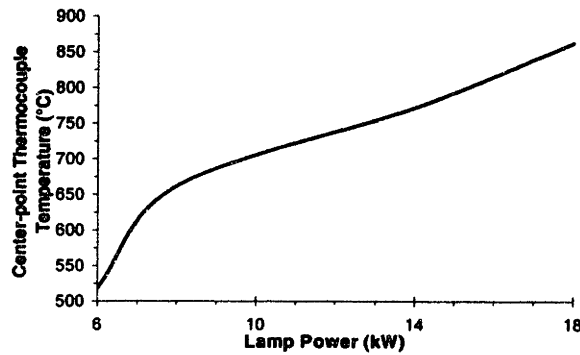


Figure 4.5: Center-point thermocouple temperature vs. delivered lamp power (20Torr)

This LPCVD is a cold-walled chamber that supplies heat to the wafer by means of two lamp banks located above and below the SiC-coated graphite susceptor (Figure 4.6).

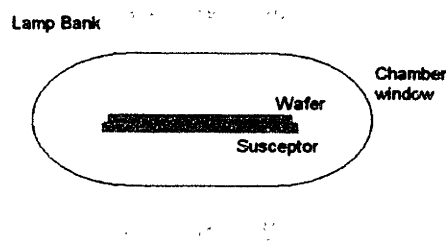


Figure 4.6: Diagram showing lamp bank illuminating wafer and susceptor

Normally, each lamp belongs to either an “inner” or an “outer” zone that directs the radiative energy to the respective section of the wafer. In this experimental design, a 3-zone lamp reflector module that divides the lamps into “inner,” “middle,” and “outer” zones is being tested.

The following lamp power distribution ratios were considered: 20/20/60, 30/30/40, 0/40/60, and 40/0/60. By counting the number of lamps in each set, the 20/20/60 configuration delivers equal power to each individual lamp. Figure 4.7 shows a sample temperature profile. The asymmetry of these plots

indicates a significant problem with this chamber design that is addressed later. The change from 40/0/60 to 0/40/60 should produce center-hot and middle-hot profiles respectively, but this is not the case. Instead, the effect is to increase the average wafer temperature without affecting its distribution. This suggests that heat is rapidly conducted from the center to the greater volume near the edges, causing the average wafer temperature to be greatest when the most power is delivered to the inner lamps. Nevertheless, the 40/0/60 does produce a hotter center temperature with respect to the edge temperature as compared with 0/40/60. However, increasing the “middle” power (0/40/60), does not proportionally raise the middle point temperature (Positions 3 & 7).

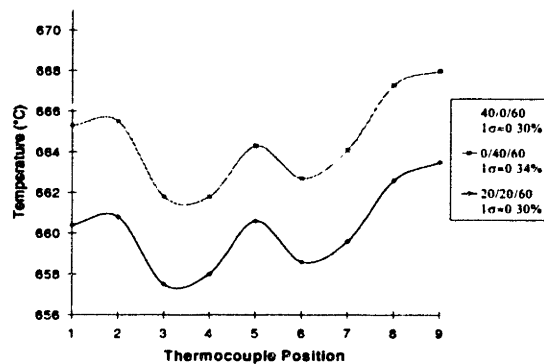


Figure 4.7: Inner/Middle/Outer lamp power distribution calibration

The temperature asymmetry indicated in Figure 4.7 above causes similar asymmetry in the thickness profile and dopant incorporation profile. This asymmetry could be caused by a tilt in the susceptor, bringing the one side closer to the lamps or moving it further from the regions of highest gas flow would both serve to increase the temperature. Even if the susceptor is perfectly planar in the chamber, one of the lamp reflectors might be misaligned causing more heat to be delivered to one side of the wafer than to the other. In Figure 4.8, DCS deposition was performed in the mass-flow controlled regime to correct flow asymmetries in the chamber; heating non-uniformities would not be detectable in this regime.

The chamber was opened so that the susceptor alignment could be checked and corrected. It was found that quartz support shaft which holds the susceptor was bent, causing the susceptor to tilt. Figure 4.8 shows the improvements achieved by replacing this part. These plots were obtained by depositing thick silicon epilayers from DCS without wafer rotation. The thickness profiles were measured using FTIR

along the important axes of the chamber: inlet-exhaust & left-right. Clearly, the bent shaft was causing the right/inlet end of the susceptor to be closer to the lamp bank. Replacing this part significantly improved deposition uniformity.

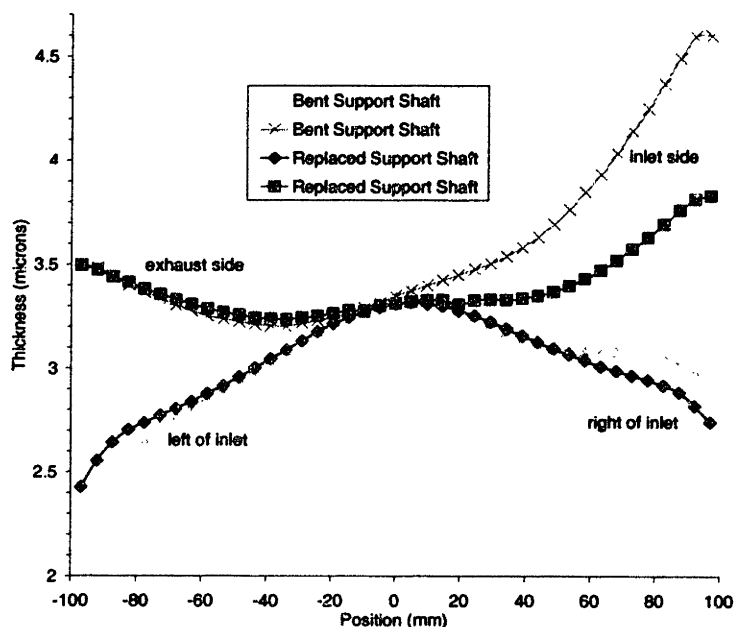


Figure 4.8: Reducing right-left asymmetry by replacing bent support shaft

Figure 4.8 gives insight into the flow pattern inside the chamber. A full description of the mass flow pattern is lengthy and complex, but is governed by many factors. It is desirable to maintain laminar flow conditions throughout the chamber, to achieve uniform deposition. Gas passes through the chamber by moving from the smaller cross-sectional inlet to the larger cross-section of the chamber and finally to the smaller cross-sectional exhaust. When the cross-sectional area increases, the gas expands and the flow rate decreases. The reverse occurs when the gas contracts near the exhaust. At lower flow rates, the residence time of the precursor molecules in the volume above the wafer is longer. Thus, the gas velocity is lowest in the center of the wafer and the film thickness may be higher. Recirculation cells, in which part of the gas flow has a significant velocity in the opposite direction of the intended flow, may also form when the cross-sectional areas changes abruptly. The presence of these cells significantly increases the molecular residence time. If these cells form near the exhaust, the gas stream contains a higher fraction of reaction byproducts, which may redeposit on the wafer surface. As the gas stream flows across the wafer,

deposition reactions reduce the fraction of precursor molecules and increase the fraction of byproduct molecules. This gas depletion effect would cause the exhaust side of the un-rotated wafer to be thinner than the inlet side. To minimize the impact of these effects, the wafer is rotated during deposition, which averages out the inlet/exhaust asymmetries, but also introduces a swirling motion in the gas flow, which further complicates the gas flow. Additionally, the non-uniform heating of the chamber affects the flow pattern. The lamp bank is designed to heat the wafer and susceptor surfaces to high temperatures, while the chamber linings and body are water and air cooled. This causes temperature gradients inside the gas stream, which lead to natural convective flows. At different pressures, natural or forced convective flows dominate, however many LPCVD deposition processes occur in the transition regime.

Sub-Section 4.1.2 Improving Flow Uniformity

To achieve uniform deposition, it is desirable to have the same laminar flow conditions above the boundary layer for every point on the wafer. However, since the wafer is circular a direct left-to-right flow does not provide this, instead the flow is introduced through an arc-shaped inlet orifice, and exits through a similar exhaust arc. The gas flows, both above and below the wafer, affect the downstream conditions. As process gases flow through the chamber decomposition reactions change the downstream gas composition and flow rate. Finally, the addition of wafer rotation (~30rpm) can create vortices in the chamber.

Flow uniformity is explored in high temperature regimes because the growth rate is mass-flow limited (**Figure 2.15** & **Figure 4.1**). The hardware options considered were the inject orifice height, the presence or absence of flow straighteners, and the type of baffles used. For finer tuning, it is possible through software to vary the ratio of gas delivered to the inner and outer regions by AccuSETT® valves and the flow of the carrier gas may be increased or decreased by mass flow controllers. Gas is introduced into the chamber through an arc-shaped inject orifice in the chamber liner; two size orifices were tested 1/4" and 1/8". Flow straighteners are arc-shaped quartz parts with 1/8" tall parallel vanes inserted in the inject orifice. In previous chamber designs, the edges did not receive enough flow so flow straighteners were designed. Based on computer models of chamber flow, straighteners should keep the lines of flow parallel, thus directing more flow to the edges of the wafer than to the center. By geometry, the use of a 1/4" orifice with flow straighteners reduces the opening to 1/8". Baffles are arc-shaped stainless steel parts

with holes machined into them of different sizes that direct flow either to the edge or center regions depending on the size, number and spacing of the holes. Baffles were tested that had 6, 7, or 8 holes on both edges, and baffles with 5, 7, or 9 holes in the center. Tracing the path of gas flow from the delivery lines to the exhaust is instructive to understand the impact of these different hardware modifications:

- 1) The amount of carrier gas is controlled by mass flow controllers in the delivery line
- 2) Process gases are mixed with the carrier gas
- 3) Gas flows through the delivery lines to the AccuSETT® valves
- 4) Gas then flows through the inner and outer baffles holes
- 5) Next, the gases pass through the inject orifice, interacting with the flow straighteners, and into the chamber

It is the goal of these hardware modifications to arrive at a configuration that delivers the greatest uniformity across the wafer, without compromising the tunability available to the operator by adjusting the AccuSETT® valves and carrier gas flow. A full set of experiments was conducted to test each possible hardware configuration, but only the relevant results are presented here. Deposition was performed using 0.2sccm DCS for 600s at 1000°C, and thickness was measured using FTIR.

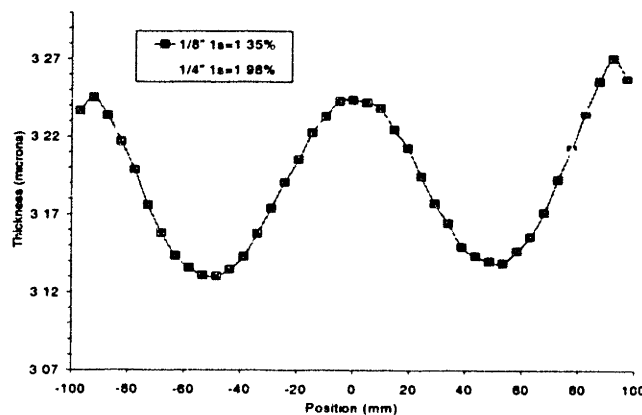


Figure 4.9: Testing the effect of different inject orifice heights

Figure 4.9 shows that increasing the orifice size from 1/8" to 1/4" decreases the flow directed to the center of the wafer. This experiment was conducted using the 6/9/6 baffles with no flow straighteners. The best thickness uniformity is achieved using the 1/8" orifice height.

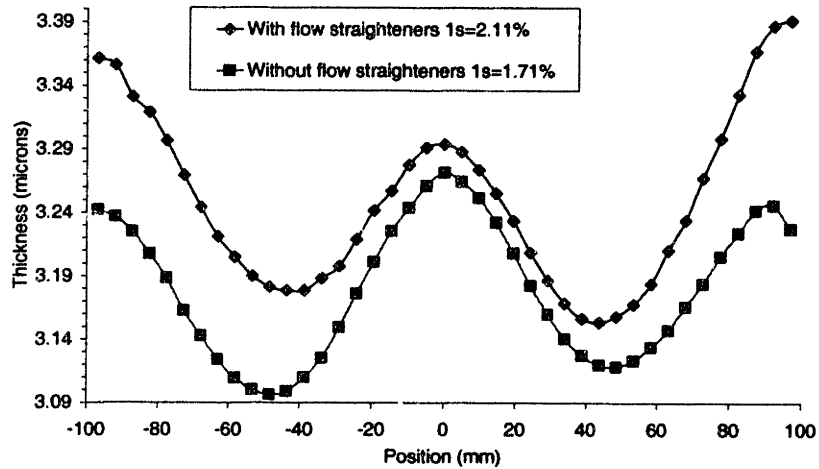


Figure 4.10: Testing the effect of flow straighteners

Figure 4.10 shows that adding flow straighteners does indeed direct more flow to the edges of the wafer, but this is to the detriment of overall uniformity. This experiment was conducted using the 8/5/8 baffles with 1/8" orifice height without the flow straighteners, and 1/4" with the flow straighteners. The best uniformity was produced without using flow straighteners.

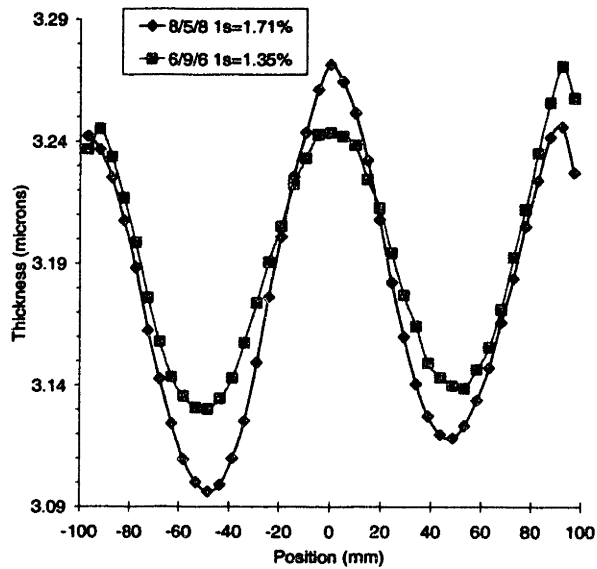


Figure 4.11: Testing different baffles combinations

Figure 4.11 shows that changing the inner/outer baffle combination has an effect on the thickness uniformity. The best uniformity was produced using the 6/9/6-baffle combination. This experiment was conducted using the 1/8" orifice height without flow straighteners. The conclusion from these experiments is that the 6/9/6 baffle combination and 1/8" orifice height without flow straighteners is the optimum hardware configuration. Using this champion hardware configuration, will now be seen if tunability is still available using the AccuSETT® valves and main carrier gas flow.

Sub Section 4.1.2-A Fine Tuning: AccuSETT® Valves

The LPCVD chamber is fitted with mass flow controllers that control the amount of gas flow to the chamber. It is also equipped with AccuSETT® valves that divide the flow between inner and edge sections of the wafer, allowing for extra flow tunability in the chamber. The degree to which they are open is measured in arbitrary units where 300 is fully open and 0 is fully closed and is controllable within the operating software.

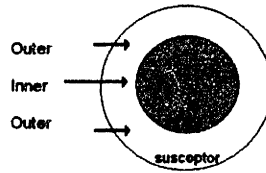


Figure 4.12: Inner vs. Outer AccuSETT® Flow

Using the champion hardware configuration Si depositions were conducted at 1000°C to observe the effects on thickness by changing the AccuSETT® valves. The main/slit valve flow was set to the default 30/3 and the lamp heating distribution was set to 30/30/40. The thickness profiles as measured by FTIR are shown in Figure 4.13 below.

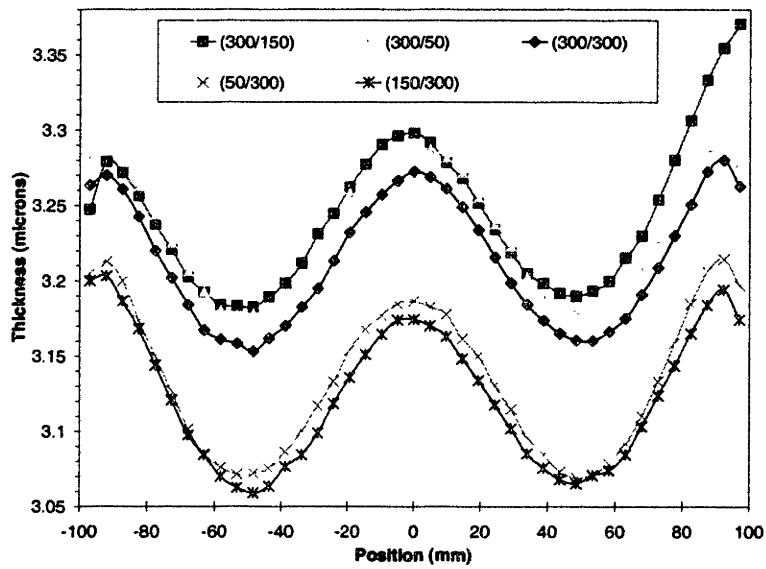


Figure 4.13: Inner/Outer AccuSETT® Calibration with 6/9/6 baffles

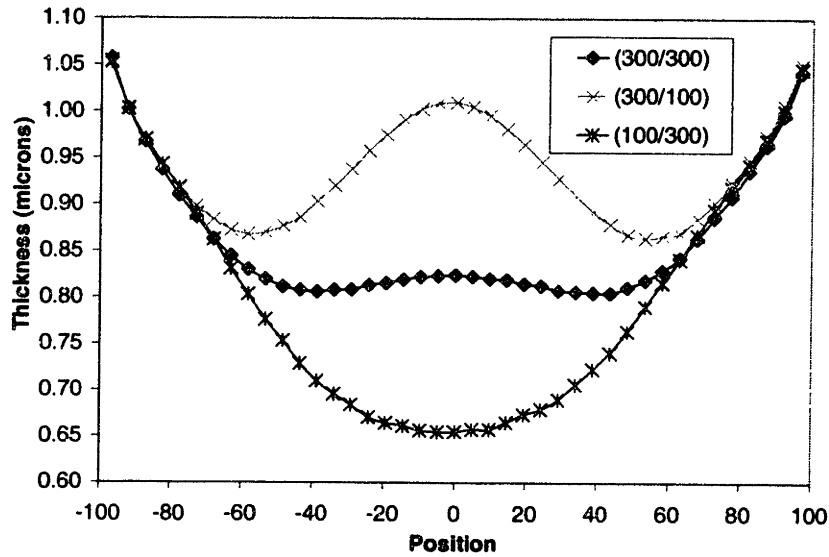


Figure 4.14: Inner/Outer AccuSETT® Calibration with 7/7/7 baffles

In addition to the 1σ parameter for measuring uniformity, it is useful to consider the $CE\%$ parameter defined in Equation 4.3 to characterize the effect of changing AccuSETT® valves.

$$CE\% = \frac{Thickness_{edge} - Thickness_{center}}{Thickness_{mean}}$$

Equation 4.3

Table 4.1: Summary of results showing effects of changing AccuSETT® settings

Baffles	AccuSETT® Setting	Mean Thickness	CE%	1σ
6/9/6	(300/50)	3.24 μm	-0.33%	1.30%
	(300/150)	3.24 μm	-1.56%	1.50%
	(300/300)	3.21 μm	-0.28%	1.31%
	(150/300)	3.12 μm	0.82%	1.46%
	(50/300)	3.14 μm	0.58%	1.54%
7/7/7	(300/100)	0.937 μm	4.30%	5.95%
	(300/300)	0.861 μm	25.4%	8.28%
	(100/300)	0.796 μm	49.1%	15.9%

Figure 4.13, Figure 4.14 and the data in Table 4.1 show that changing the AccuSETT® settings does have an effect on the thickness uniformity, but that the magnitude of this effect is hardware dependent. For the 6/9/6 baffles, the AccuSETT® tuning has little effect on the thickness profile. Since the 1σ value is low for all combination of valve setting, it is concluded that the baffle hole distribution is optimal for

producing uniform films. For the 7/7/7 baffles, the effect of changing the AccuSETT® valves is tremendous, the *CE%* value changes over an order of magnitude. Increasing the proportion of the flow directed to the inner zone increases the center thickness, and decreasing the flow directed to the outer zone has the strongest effect on the middle zone thickness and little effect on the edge points. (300/300) with 6/9/6 baffles was determined to produce the most uniform flow because of the low 1σ value of 1.31% and nearly zero *CE%* of -0.28%.

Sub Section 4.1.2-B Fine Tuning: Carrier Gas Flow

Process gases are introduced to the chamber diluted in a H₂ carrier gas flow. This flow is introduced to the chamber as main and slit valve H₂, flow though the slit flow does not contain process gases. The main H₂ flow is directed parallel to, and just above the wafer surface. Too high H₂ flows tend to create a “W” shape in thickness across the wafer and too low H₂ flows tend to create an “M” shape. Typical main H₂ flows are 20-40slm. The slit valve flow is directed through the slit valve tunnel, and flows beneath the susceptor. The main purpose of the slit valve flow is to prevent susceptor and lower dome coating. It is kept small, otherwise it will negatively impact the thickness uniformity, particularly at the edge of the wafer. The range of typical slit H₂ flows is 2-5slm.

The following main/slit inlet H₂ flow (slm) distributions were considered: 15/3, 24/3, and 35/3. Increasing the magnitude of this flow increases the cooling effect the moving gas stream has on the wafer. The temperature profile across the wafer at for different flow distributions is given in Figure 4.15. The non-uniformity of these plots gives information about the chamber. The center of the wafer is cooler than the edges, as previously predicted. Also, there is an asymmetric insertion of gas into the chamber, with lower flow on the right-hand side. Ignoring the right-left asymmetry, the uniformity increases with decreasing main flow magnitude.

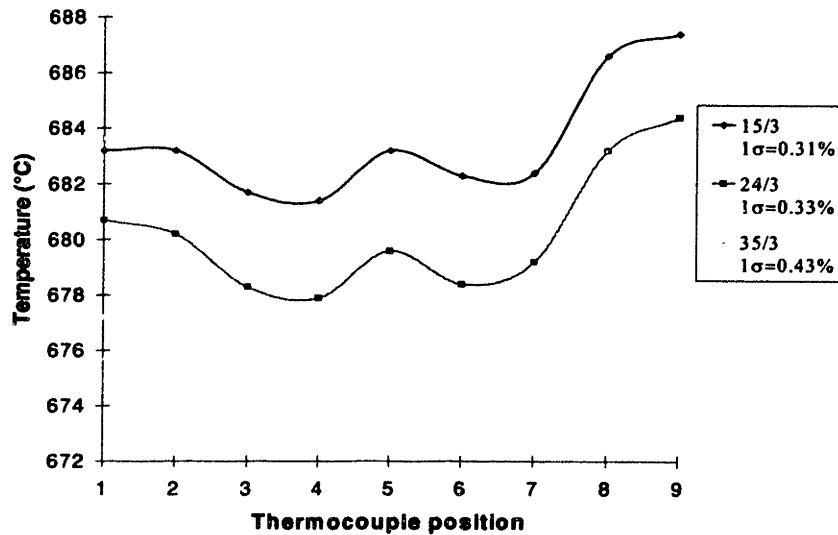


Figure 4.15: Main/Slit valve flow calibration

Figure 4.16 shows that it is possible to vary the carrier gas flow rate to increase the thickness at the center of the wafer and match it to the end-points. Increasing the carrier gas flow rate decreases the precursor gas concentration causing the average thickness to be lower. It is also observed that increasing the carrier gas flow rate preferentially increases the center-point thickness. This can be explained because the main injection for the carrier gas is directed more towards the center of the wafer than to the edge.

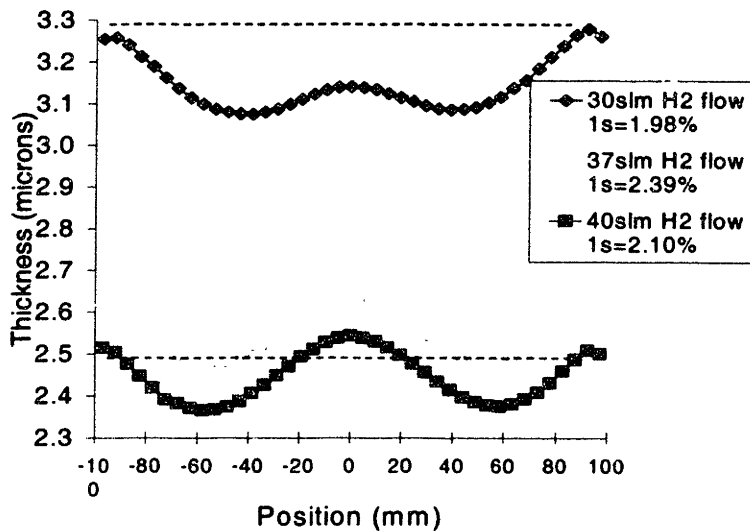


Figure 4.16: Increasing the main H₂ flow changes the Si thickness uniformity (6/9/6, 1/4" orifice, no flow straighteners)

The best uniformity data at T=1000°C was achieved using the 7/7/7 baffles with 1/8" orifice height and no flow straighteners. Additional flow tuning, using the AccuSETT® valves and main H₂ flow, and temperature tuning, using the lamp power distribution ratios was able to achieve 1σ=0.58%.

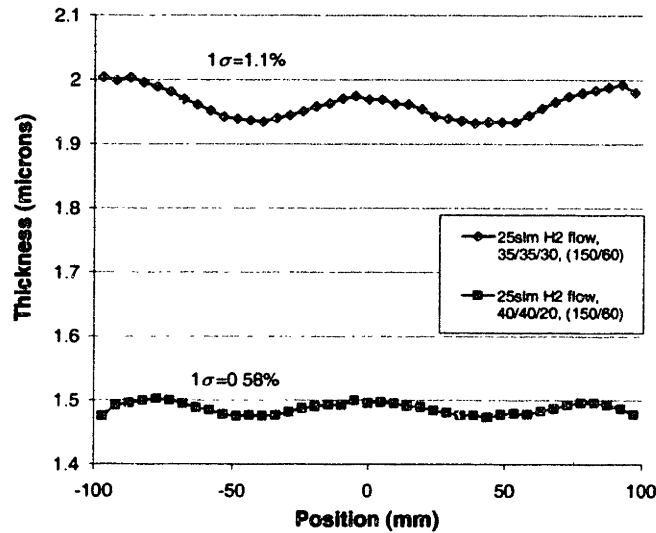


Figure 4.17: Uniform deposition at T=1000°C

Sub-Section 4.1.3 Improving Deposition Uniformity

Depositions using DCS were performed to determine the effectiveness of the 3-zone configuration in producing a uniform deposition profile at low temperatures. The power distribution ratios presented in Table 4.2 were explored and the resulting profiles of Figure 4.18 were measured by FTIR.

Table 4.2: Thickness and %Ge uniformity experimental conditions and results (6/9/6 baffles)

Power Setting	Deposition Temperature	Relative DCS flow	Relative GeH ₄ flow	Thickness 1σ	[Ge] 1σ
15/15/70	680°C	6.62x10 ⁻³	9.92x10 ⁻⁵	2.94%	4.51%
20/20/60				1.36%	3.26%
24/24/52				2.10%	1.50%
22/22/56				1.91%	1.55%
21/21/58				1.75%	1.61%

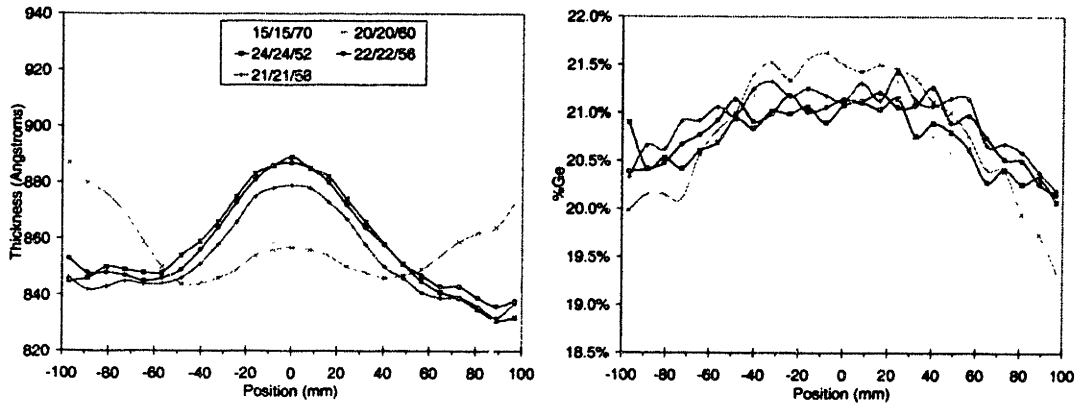


Figure 4.18: DCS thickness and %Ge profiles (300/300)

This data indicates that 20/20/60 achieves the best thickness uniformity, and 24/24/52 achieves the best %Ge uniformity, however taking both thickness and %Ge into account 21/21/58 had the lowest 1σ value. The profiles in Figure 4.18 show two important problems with SiGe deposition: Ge lowest where thickness is highest, and the Ge profiles do not match the thickness profiles. The first of these results from lower Ge incorporation rates at higher temperatures (see also Figure 4.24), and suggests that additional flow tuning is necessary to deliver more germane to the outer regions of the wafer. Since these depositions are done at 680°C the growth rate is limited by the surface reaction rate, and not the flow conditions, so this additional flow should not affect the thickness profile. This point is reinforced by the observation that the changes in lamp power distribution are reflected only in the thickness profile, and not in %Ge profile. Clearly, the Ge incorporation is more sensitive to gas flow conditions than temperature conditions.

Section 4.2 Purifying Process Gases

Eliminating the impurities in high-quality deposited films requires very pure gas supplies. Despite the best efforts of gas suppliers, individual tanks can contain intolerable levels of H₂O, O₂, and CO₂ for low temperature, extremely high quality films. These oxidation by-products arise from the manufacturing process, transfer into, and degradation of the storage container, and contact with the gas delivery system. Of particular importance in deposited Si and SiGe films is the reduction of the O impurity concentration. To reduce the thermal budget, many deposition processes are conducted at lower temperatures, which

implies a slower growth rate. Slower film growth means more impurities incorporated into the film for a given flux of impurities. This slower growth rate also results in a higher Ge incorporation since the thermal activation for GeH_4 is lower than $\text{SiH}_4\text{-GeH}_4$ breaks down more easily at lower temperatures. Unfortunately, the GeO species is very volatile so that when GeO lands on the surface more oxygen is incorporated. The result is that lower temperatures processes are more susceptible to increased oxygen impurities.

For waveguide applications, reducing the oxygen concentration is also critical since high levels increase the absorption coefficient leading to higher losses. One of the possible mechanisms of the absorption increase is the formation of defects, such as grain boundaries or dislocations, that disrupt the lattice. The increase of the absorption coefficient with increasing oxygen content is illustrated in Figure 4.20 for $\lambda=9.1\mu\text{m}$, and a similar trend of decreasing absorption coefficient for decreasing oxygen concentration is expected to hold at $\lambda=1.55\mu\text{m}$.

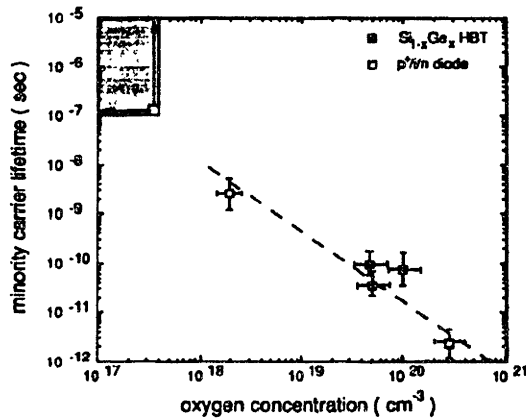


Figure 4.19: Lifetime trends in oxygen-doped $\text{Si}_{1-x}\text{Ge}_x$ films, for $0.15 < x < 0.31$. The open symbols represent lifetime data from the $p^+ - i - n$ diodes, while the closed symbols represent lifetimes extracted by simulating data for $\text{Si}/\text{Si}_{1-x}\text{Ge}_x$ HBTs. The shaded region indicates the approximate sensitivity limits for determining the oxygen content and lifetime in these $p^+ - i - n$ diodes [9].

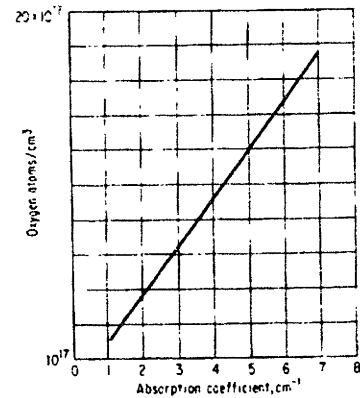


Figure 4.20: Oxygen content versus $9.1\mu\text{m}$ absorption coefficient [37].

In $\text{Si}/\text{Si}_{1-x}\text{Ge}_x/\text{Si}$ HBTs, O acts as a recombination site in the base. It has been shown that the minority-carrier lifetime is increased by at least four orders of magnitude as the O concentration is reduced from 3×10^{20} atoms/ cm^3 to below 3×10^{17} atoms/ cm^3 (Figure 4.19). The electron and hole concentrations in a doped semiconductor are related by the equation:

$$N_e N_h = N_i^2$$

Equation 4.4

where N_i is the intrinsic charge concentration (for Si, $N_i=10^{10} \text{ cm}^{-3}$). Since O is in Group VI it is an n-type dopant in Si, donating 2 electrons/atom when incorporated substitutionally on the Si lattice. Reducing the O concentration from 10^{20} cm^{-3} to 10^{17} cm^{-3} decreases the conductivity of Si by 2 orders of magnitude (Figure 4.21).

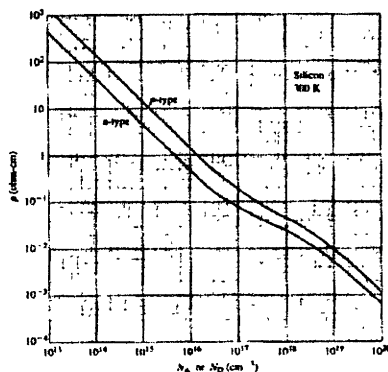


Figure 4.21: Resistivity versus impurity concentration in Si at 300K [6]

This change is most significant in Si intentionally p+ doped because the carriers added by background O cancel the desired hole concentration. The 1999 SIA Roadmap states that for 200mm processing the O surface concentration should be $<1 \times 10^{14} \text{ atoms/cm}^2$ or $<1 \times 10^{18} \text{ atoms/cm}^3$ [1]. Addressing the issue of O contamination is therefore of primary importance in the chamber development.

The GateKeeper® Hydride Gas Purifier Model 35K by Aeronex, Inc. was tested for its effectiveness at removing O_2 from the GeH_4 gas supply (for product specifications sheet see Section 10.3). The purifier was inserted in the gas manifold as shown in Figure 4.22 so that it could be easily activated and deactivated. Before testing, the purifier was saturated with germane by flowing at least 150,000 sec of GeH_4 through it. This saturation is necessary otherwise, the purifier will remove germanium as in impurity. This saturation process was monitored by simultaneously depositing SiGe and measuring the germanium fraction by XRD (Figure 4.23).

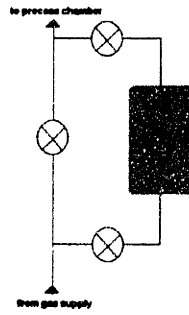


Figure 4.22: GeH₄ purifier manifold

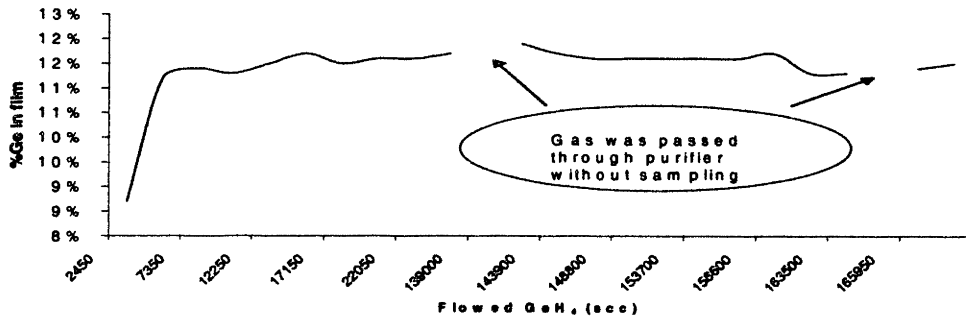


Figure 4.23: Saturation of Aeronex GateKeeper® Hydride Gas Purifier

To test the ability of the saturated purifier to remove O₂ at various processing temperatures, a recipe was run with the purifier in-line and out-of-line that deposited a SiGe film at increasingly lower temperatures. From $T_{\text{sust}}=900^{\circ}\text{C}$ to 500°C ($T_{\text{wafer}}=876^{\circ}\text{C}$ to 472°C), alternating layers of SiGe with Si spacer layers were deposited and analyzed by SIMS using 5keV Cs. A 1 μm thick Si capping layer was deposited above the alternating layers to prevent O diffusion from the surface from interfering with the SIMS measurement of the in-line purifier sample. The results clearly show the need for an inline purifier (Figure 4.24). The detection limit using SIMS for O is 2×10^{17} atoms/cm³, so our true values for incorporated O are likely to be lower than reported.

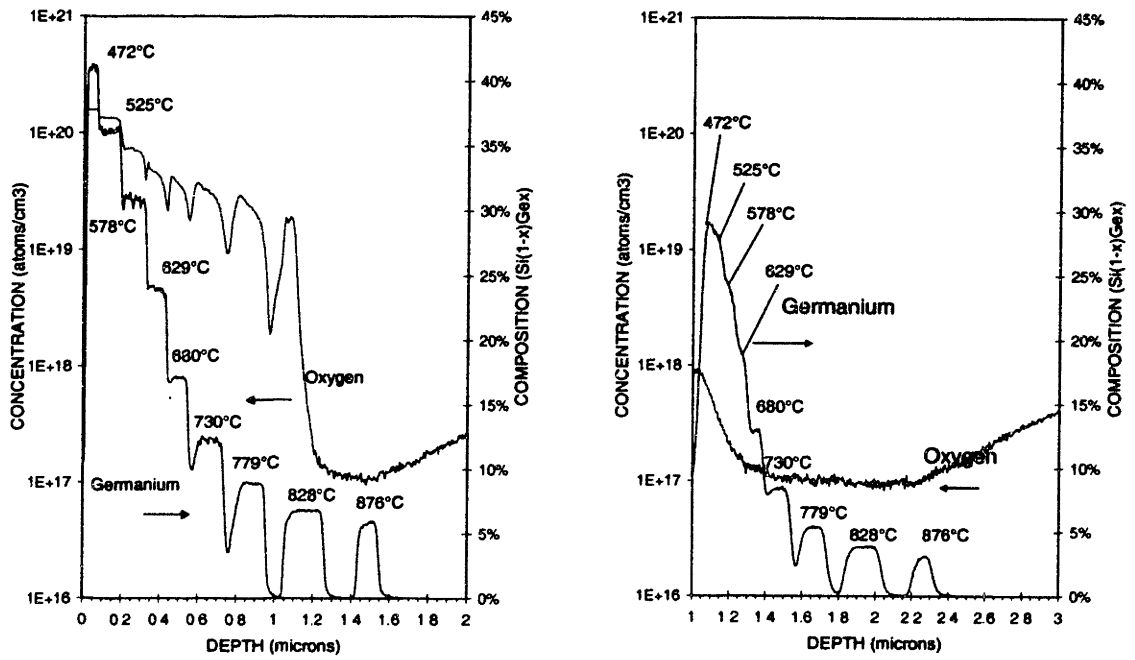


Figure 4.24: SIMS profile of Ge-containing film deposited at decreasing wafer temperatures

Before purification

After purification

Chapter 5 LPCVD Process Characterization

In this section, characterization is performed on some of the processes that are executed by the LPCVD chamber. These processes are not limited to those necessary for waveguide fabrication, but instead cover applications for transistor and capacitor fabrication also.

Section 5.1 explores ability for the LPCVD reactor to deposit selective epitaxial Si. Selective deposition can be used in the fabrication of waveguide structures on patterned oxide masks, but it is most commonly used to deposited the extended source and drain regions necessary to continue the miniaturization of MOSFET structures. Section 5.2 explores the ability of the LPCVD reactor to deposit smooth polycrystalline SiGe films, which are used to form the base contact in non-selective HBT device fabrication. Section 5.3 concludes with a look at the advantages of alloying SiGe films with C. Firstly, it examines the effect C has towards suppressing B diffusion, which is important for maintaining the sharp dopant profiles throughout the chip process flow. Secondly, the effect of C on reducing the strain in SiGe epitaxial films is explored. This is useful because it demonstrates that C alloying is an extra degree of freedom that may be used to engineer SiGe films of a desired strain and bandgap.

Section 5.1 Selective Epitaxial Growth

Selectivity is possible because of the higher nucleation rate of Si on Si, versus Si on SiO₂. Though the nucleation rate is lower on SiO₂, once a layer of Si is present on the oxide, the growth rate would be as if the substrate were Si. Gas-phase nucleation and surface nucleation suppressed by adding chlorine to the chamber chemistry. By increasing the Cl/Si ratio, the growth goes from blanket deposition, to selective deposition, to etching. To achieve a higher Cl partial pressure SiH₂Cl₂ (DCS) is used instead of SiH₄ as the Si source; adding HCl also improves selectivity by etching any islands that nucleate on the SiO₂ surface. As might be inferred from the etching effects of Cl atoms, the growth rate of DCS is less than SiH₄ (**Figure 4.1**). Increased HCl flow also depresses the epitaxial growth rate. For long deposition times, the difference in nucleation rates can be translated into an “incubation time.” It is desirable to engineer this incubation time such that it is longer than the deposition time resulting in selective growth. The effects of other process parameters are summarized in the table below.

Table 5.1: Effect of process parameters on selective epitaxial deposition

Process Parameter	Effect of Change
Lower Temperature	Decreases growth rate (Figure 4.1) Increased selectivity, lower thermal budget
Lower Pressure	Decreases "loading effect", more selective
Higher DCS flow rate	Increased growth rate, decreased selectivity
Higher HCl flow rate	Increased selectivity, decreased growth rate

Experiments were performed to determine the capability of the LPCVD chamber to selectively deposit Si on Si substrates without growth on SiO₂. Baseline substrates were prepared by growing 4μm of intrinsic silicon on p+ (100) Si substrates. Thermally grown 1000Å silicon oxide wafers were used as test substrates. Pre-growth was done on the baseline substrate at 950°C for 4 minutes using 300slm of SiH₄, preceded by a standard high temperature prebake step, to produce an uniform epilayer. For SEG with DCS and HCl gases were used as precursors diluted in H₂ carrier gas. Experiments were conducted in the low-temperature ($T_{sur} \leq 750^\circ\text{C}$) and low-pressure ($P_{chamber} \leq 20\text{Torr}$) regime to achieve a desired thickness of 300-400Å, suitable for ESD applications. Using the experimental condition in Table 5.2, additional growth on the baseline substrates was compared against any growth on the test substrates to determine selectivity.

External contaminants on the surface of the wafer can act as heterogeneous nucleation sources. To insure that external contaminants are not introduced into the chamber, many measures are taken produce system cleanliness. Among these are a depressurized pre-chamber load-lock, which is backfilled with N₂ before insertion in the process chamber. In addition, the gas purifiers similar to those tested in Section 4.2 were employed on the DCS supply lines to reduce gaseous contaminants.

Under normal illumination, the change of color change of the oxide wafers with silicon growth is an obvious indicator of nonselective growth. The change of color can be considered an "all-or-none" phenomena. Although there is an energy barrier for the initial nucleation of a Si island on oxide, the time between nucleation and full coverage is very short. Smaller nucleation islands were sought using optical microscopy at the maximum magnification of 500x. This technique has limited sensitivity since even at this magnification, nucleation islands in the early stages of development may be undetectable. FTIR was used to measure the growth on the baseline substrates to extract growth rate data. If neither color change, nor nucleation islands were observed, the process was considered selective against oxide.

Table 5.2: Selective epitaxial growth experimental conditions and results; shaded condition exhibited growth on oxide

T_{susc} (°C)	P_{chamber} (Torr)	H_2 Flow Rate (slm)	DCS Flow Rate (slm)	Growth Rate on p+ Si (Å/min)
722	5	15	0.1	5.4
722	5	15	0.3	5.4
722	5	15	0.6	5.1
722	20	20	0.6	8
732	5	15	0.1	5.7
732	20	20	0.6	5.7
747	5	15	0.1	10.2
747	20	20	0.6	4.2

Deposition on oxide was observed for the shaded conditions. Clearly the experiments conducted at $T_{\text{min}} = 722^\circ\text{C}$ are of most interest, since they are low temperature and selective. However, further work is needed to identify higher throughput, low-thermal budget conditions. These results, shown in Table 5.2, can best be viewed as points in process space Figure 5.1. Here it can be seen that non-selectivity occurs in the high-temperature/high DCS flow rate/high H_2 flow rate regime. This is expected because at high temperatures, the thermally activated surface reaction rate, k_{sm} , is accelerated (**Equation 2.19 & Equation 2.22**) leading to greater deposition. In addition, at higher DCS flow, the concentration of Si in the gas phase, C_g , is higher, so the flux diffusion is higher causing more reactive species to be delivered to the wafer surface (**Equation 2.17**). At higher H_2 flow, the gas-phase concentration of the DCS decreases, and so the etching-effect of the Cl atoms is lessened. All three of these factors lead to non-selective deposition.

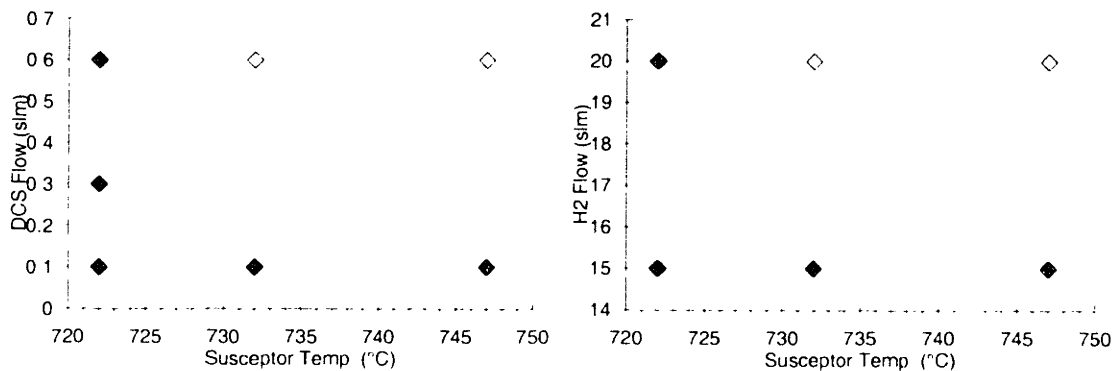


Figure 5.1: Results of SEG experiments mapped in the process space; open diamonds indicates deposition on oxide, closed diamonds indicates no deposition on oxide

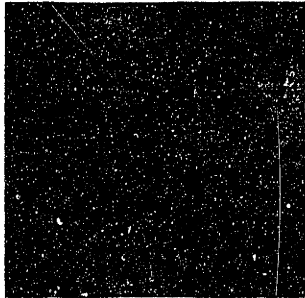
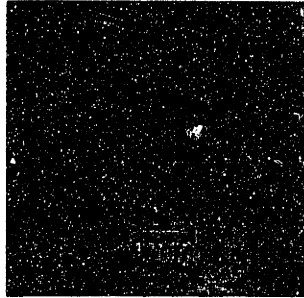
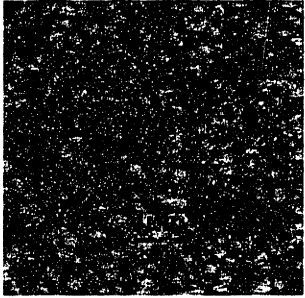
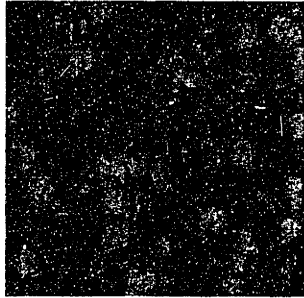
Section 5.2 Polycrystalline SiGe on Oxide and Nitride

In simultaneous deposition of epitaxial and polycrystalline SiGe for HBT devices, the quality of the poly film is as important as that of the epi film. In this section, the ability of the LPCVD chamber to deposit smooth polycrystalline SiGe and SiGeC on oxynitride surface is explored. Since wafers with oxide and nitride layers pre-grown on them are readily available, roughness information was obtained using these. It is possible to interpolate for depositions on oxynitride using these two extremes.

Deposition was conducted at $P_{chamber}=100\text{Torr}$ and $T_{sus}=650^\circ\text{C}$ for 150s using 0.05slm SiH_4 , 500sccm GeH_4 , and 5sccm SiCH_4 where applicable. Given a growth rate of approximately $500\text{\AA}/\text{min}$, this should yield about 1000\AA of polycrystalline thickness. AFM analysis was performed on a $20\times 20\mu\text{m}$ and a $2\times 2\mu\text{m}$ -square at the center of on wafers processed at each condition.

The surfaces are shown at different magnification in Figure 5.2 to Figure 5.5 (the colors in the image are false and result from the polarization lens in the microscope). The results from the AFM analysis are shown in Table 5.3 below.

Table 5.3: AFM Images and Root-mean squared roughness of polySiGe on nitride and oxide

AFM Raster size	Nitride	Oxide
2 μm x2 μm	 <p data-bbox="651 610 803 637">$R_{\text{ms}}=4.678\text{nm}$</p>	 <p data-bbox="993 610 1145 637">$R_{\text{ms}}=81.840\text{nm}$</p>
20 μm x20 μm	 <p data-bbox="651 973 803 999">$R_{\text{ms}}=5.289\text{nm}$</p>	 <p data-bbox="993 973 1145 999">$R_{\text{ms}}=110.75\text{nm}$</p>

These results show that the film deposited on the oxide surface is much rougher than that on nitride. This most likely caused by a differential interaction with the substrate. Both polycrystalline films exhibit intolerable roughness levels. Much work remains to optimize this LPCVD chamber for the deposition of smooth polycrystalline films.

Optical Microscope Images of polycrystalline SiGe surface

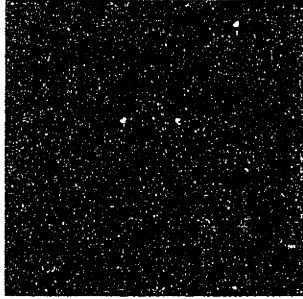


Figure 5.2: Poly SiGe on nitride

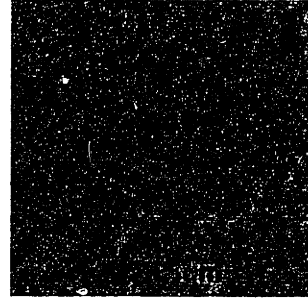


Figure 5.3: Poly SiGe on oxide

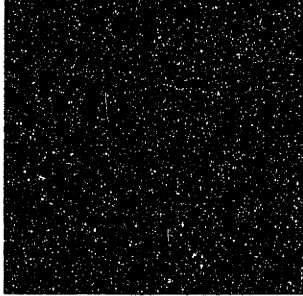


Figure 5.4: Poly SiGe on nitride

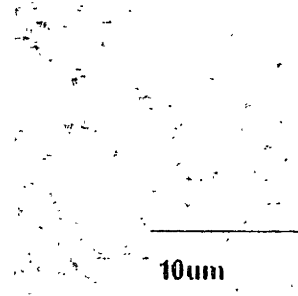


Figure 5.5: Poly SiGe on oxide

Section 5.3 SiGeC Epitaxial Films

Incorporating C in SiGe epitaxial films has a number of useful effects for device fabrication. C atoms generate a conduction band offset in tensile-strained Si/SiC systems that can be used for high mobility two-dimensional electron gases in the channel of NMOS devices [29]. In addition, substitutional C atoms on the SiGe lattice reduce the lattice constant, making it closer to that of Si. This diminishes film strain allowing for thicker SiGe film without relaxation by dislocation formation.

Sub-Section 5.3.1 Effect of C on B Diffusivity

The base region in SiGe NPN HBTs is heavily doped with boron to increase the hole concentration. To further increase transistor frequency this base region is designed very thin, with abrupt changes in the doping profile at the collector and emitter interfaces. The boron doping can occur during epitaxial growth, or as post-growth ion implantation. However, to be made electrically active, the B atoms must reside substitutionally on lattice sites. This is done by a rapid thermal-annealing step, known as "activation." In the case of ion implantation, the step also serves to repair lattice damage caused during

implantation. As device dimensions shrink, improved performance requires the SiGe base to be thinner and more heavily doped, placing severe budget constraints on the heat treatment needed to activate the dopant.

The incorporation of substitutional C acts to suppress the diffusion of B in SiGe lattice. The suppression of boron diffusion has been explained by the coupled diffusion of C and Si self-interstitials. Since boron diffuses via an interstitial mechanism, the diffusion of C from the base depletes the area of Si self-interstitials. This reduces the boron diffusion coefficient, which is proportional to the normalized concentration of self-interstitials [28].

In order to explain this diffusion reduction effect, two separate wafers were processed under identical conditions, except one was subjected to an annealing step after deposition. The identical portions of the recipe deposited SiGeC:B at 650°C. Four B spikes were formed by flowing B₂H₆ separated by SiGe deposition without B₂H₆. For the deepest two spikes, SiCH₄ was flowed but was turned off after the end of the second spike. At the end of the recipe, a capping layer of silicon was deposited. The test wafer was annealed at 950°C for 40s following the capping. The depth profiles of both wafers were measured using SIMS.

The results obtained are presented together in Figure 5.6 and Table 5.4. It is evident that the addition of C to SiGe does act to reduce the diffusion of B at elevated temperatures. The figure of merit used to measure peak broadness is the full-width-at-half-maximum (FWHM) and is defined as the width of the peak at half the maximum peak value. The FWHM of the annealed peaks deposited without C is 71.67% larger than the FWHM for the annealed peaks whose diffusion was suppressed by C, but is 224.6% larger than the unannealed peaks with C.

Figure 5.6 also shows that despite the suppressing effects of C, the annealed B peaks broaden by 89.06% compared to the unannealed peaks with C. Even without the 40s anneal, the B peaks deposited without C demonstrate minor broadening compared to those with C; the FWHM increases by a slight 18.17% as a result of the subsequent deposition temperature treatments.

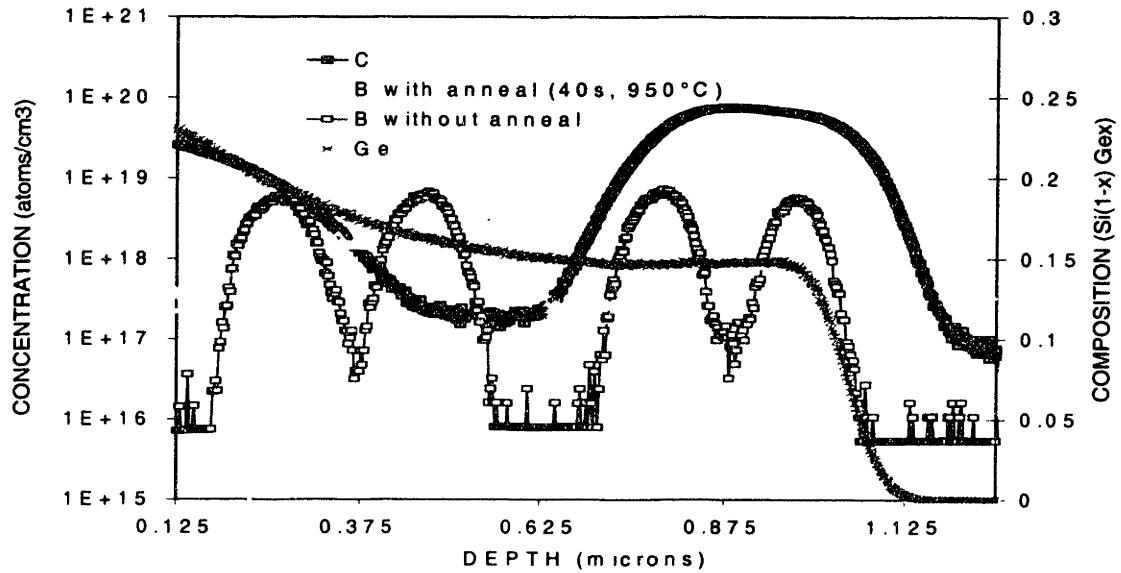


Figure 5.6: C suppresses the diffusion of B in the SiGe lattice

Table 5.4: FWHM of B peaks

Annealed w/o C	Annealed w/C	Unannealed w/o C	Unannealed w/C
0.438 μ m	0.255 μ m	0.159 μ m	0.135 μ m

Sub-Section 5.3.2 SiGeC Strain Compensation

Carbon is isoelectronic with Si and Ge and is also capable of forming sp^3 bonding structures like Si and Ge. The lowest-energy position of C in Si is the substitutional site, and the observed activation energy for the diffusion of substitutional carbon (3.04eV) is quite large [18]. However, because of its smaller size, when it is incorporated substitutionally of the SiGe lattice, it acts to decrease the strain of the film relative to Si, without changing the carrier concentration. Several workers in the field have shown that the fraction of C incorporated substitutionally decreases at higher deposition temperatures ([19] & [21]). For the purposes of this present study, the percentage of substitutional C for a given flow, x , of $SiCH_6$ will be estimated using the following equation:

$$\%C_x^{subs} = \frac{\%Ge_{SiCH_6, flow=0}^{XRD} - \%Ge_{SiCH_6, flow=x}^{XRD}}{9}$$

Equation 5.1

Several depositions were conducted to explore the processing conditions necessary to achieve strain compensation for a given Ge fraction. Figure 5.7 shows XRD scans of SiGeC films grown at $T_{susc}=700^\circ\text{C}$ using the same SiH_4 and GeH_4 flow values and increasing SiCH_6 flows. The significant feature of Figure 5.7 is that the SiGe peak moves steadily towards the substrate peak with increasing SiCH_6 flow values, while the fringe pattern remains unchanged. This shows that increasing the C concentration decreases the mismatch between the Si and SiGeC lattice parameters, still allowing for epitaxial deposition without relaxation. Using this effect it is possible to grow high Ge concentration pseudomorphic SiGeC layers which are thicker than the predicted critical thickness for SiGe without dislocation formation.

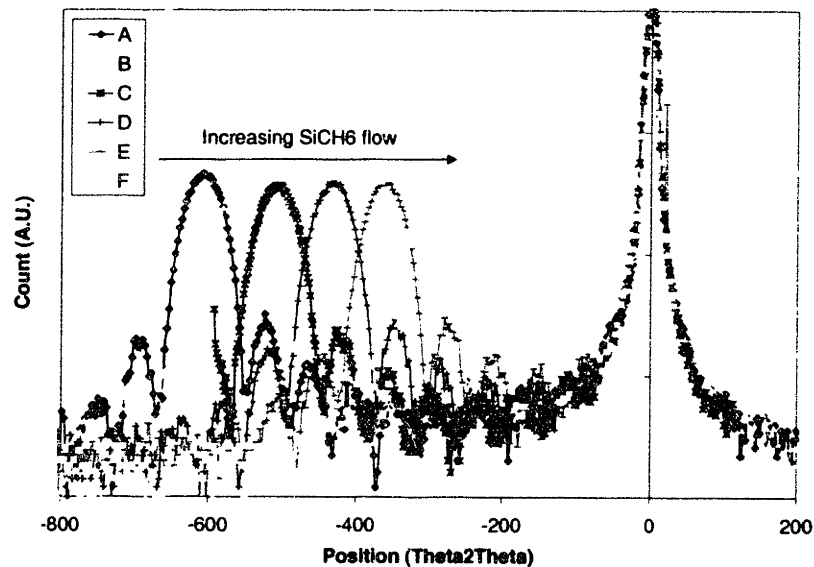


Figure 5.7: Increasing SiCH_6 flow leads to strain compensation. Pseudomorphic growth is maintained, as seen by the well-defined fringe pattern.

Figure 5.8 shows that this trend can be extended to allow for complete strain compensation. In this case, the SiGe peak is shifted until it coincides with the substrate peak, indicating that there is no longer any lattice mismatch between the film and the substrate. The absence of well-defined fringes indicate that some relaxation has occurred, so the film is no longer completely pseudomorphic. When the relative flow rate of SiCH_6 is 0.091, the film is fully strain-compensated. Figure 5.9 is the SIMS profile for

this sample showing that $\text{Si}_{0.965}\text{Ge}_{0.027}\text{C}_{0.00786}$ is the composition that is lattice matched with Si. This makes it very useful for growing thick, strain-free epitaxial films. For all samples, it was observed that the growth rate was not affected by alloying with C, and instead remained high.

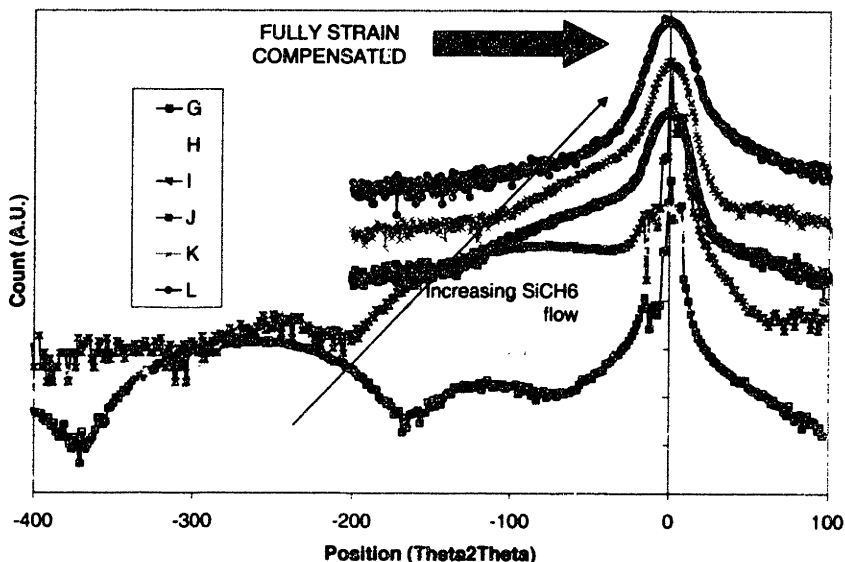


Figure 5.8: Complete strain compensation is realized for higher SiCH_6 flow rates. Films are no longer completely pseudomorphic.

Table 5.5: Growth conditions for samples shown in Figure 5.7 and Figure 5.8

Sample	Relative GeH_4 flow	Relative SiCH_3 flow	$\% \text{Ge}^{\text{sub}}$	$\% \text{C}^{\text{sub}}$	Growth Rate ($\text{\AA}/\text{min}$)
A	1.42×10^{-4}	0	5.8%	0%	215.3
B		2.85×10^{-6}	5.4%	0.044%	212.4
C		5.70×10^{-6}	5.0%	0.088%	205.9
D		8.55×10^{-6}	4.2%	0.177%	205.6
E		1.14×10^{-5}	3.4%	0.267%	208.5
F		1.42×10^{-5}	2.9%	0.322%	210.1
G	3.71×10^{-5}	0	2.5%	0%	124.3
H		4.99×10^{-6}	1.8%	0.077%	122.1
I		9.98×10^{-6}	1.4%	0.122%	124.1
J		1.14×10^{-5}	SiGe peak too close to substrate to resolve		125.9
K		1.28×10^{-5}			130.6
L		1.43×10^{-5}	(see Figure 5.9)	(see Figure 5.9)	132.4

For sample L, SIMS analysis was performed to determine the total atomic concentrations. For this case, since the strain is fully compensated the value for $\% \text{C}^{\text{sub}}$ as predicted by Equation 5.1, is just the Ge concentration divided by 9, which gives 0.3%. However, from the SIMS analysis, C accounts for 0.784%

of the film composition. Clearly, most of the C has assumed interstitial sites, and only 38% of the total C resides on substitutional sites.

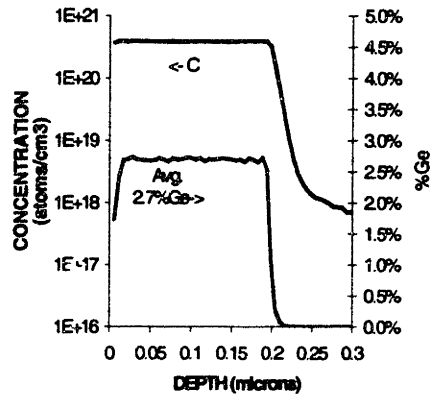


Figure 5.9: SIMS measurement of fully strained compensated SiGeC thin film

Chapter 6 Application: Waveguides

Silicon germanium has a refractive index that is larger than Si, a property that can be used for guiding light in Si/SiGe/Si structure and making optical devices. These devices can be fabricated using the same equipment and technologies as those utilized for Si-based integrated circuits. This chapter begins by solving the relevant propagation equations for this waveguide design (section Section 6.1 & Section 6.2). Next, the methods for fabricating and testing straight waveguide structures are presented in section Section 6.3. Optical loss measurements were performed on these waveguides and the results are given in Section 6.4. Future designs that are being considered to investigate the effects of signal coupling are presented in Section 6.5.

Section 6.1 Waveguide Equations

In this section, the bounce angles of the waveguide modes are derived, from which the propagation constants, and field distributions are derived for the two dimensional dielectric waveguide shown in Figure 6.1. Particularly important equations are enclosed in boxes. The derivation presented here follows closely to that given by Saleh & Teich [24].

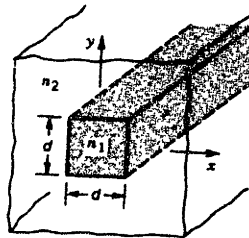
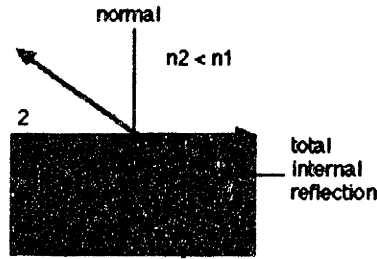


Figure 6.1: Two dimensional waveguide structure [24]. Compare with Figure 6.11.

When light is incident on a dielectric boundary, the angle of reflection, or transmission with respect to the normal, is determined by the familiar Snell's Law:



$$n_1 \sin \theta_1 = n_2 \sin \theta_2$$

Equation 6.1

If the ratio of indices is such that $\theta_2 > 90^\circ$ then the light is *totally internally reflected* back into the originating material, at $\theta_2=90^\circ$ the light is transmitted along the boundary and $\theta_1=\theta_c$, the *critical angle*. Optical fibers and waveguides contain light by using the index contrast between the higher index core and the lower index cladding to cause total internal reflection at every “bounce,” θ_i , of the light as it is transmitted along the z direction. It will be useful to also define the complement of the critical angle, $\bar{\theta}_c$.

$$\theta_c = \theta_c = \sin^{-1}\left(\frac{n_2}{n_1}\right) \qquad \bar{\theta}_c = \frac{\pi}{2} - \theta_c = \cos^{-1}\left(\frac{n_2}{n_1}\right)$$

Equation 6.2

The field inside the core is assumed to be a monochromatic TEM plane wave of wavelength $\lambda=\lambda_0/n_1$ bouncing back and forth at an angles $\theta < \bar{\theta}_c$ between the cladding core interfaces at $-\frac{d}{2} < x < \frac{d}{2}$ and $-\frac{d}{2} < y < \frac{d}{2}$. The wave travels with phase velocity $c_1=c_0/n_1$, has wavenumber $k=n_1k_0$, with wavevector components $k_x=n_1k_0 \sin\theta$, $k_y=n_1k_0 \sin\theta$, and $k_z=n_1k_0 \cos\theta$. To determine the modes a self-consistency condition is imposed that a wave reproduces itself after each round trip. There is also a phase shift known as the Goos-Hanschen shift, φ_r , introduced by each total internal reflection at the dielectric boundary. For self-consistency, the phase shift between the two waves must be zero or a multiple of 2π .

$$\left(\frac{2\pi}{\lambda}\right)2d \sin \theta - 2\varphi_r = 2\pi m, \qquad m=0, 1, 2, \dots$$

Equation 6.3

where m is the *mode number*.

φ_r can be shown to be a function of the angle θ and $\bar{\theta}_c$. It also depends on the polarization of the incident wave, but this effect will not be expounded on further. In the TE case, this shift is given by

$$\tan \frac{\varphi_r}{2} = \left(\frac{\sin^2 \bar{\theta}_c}{\sin^2 \theta} - 1 \right)^{\frac{1}{2}}$$

Equation 6.4

So that φ_r varies from π to 0 as θ varies from 0 to $\bar{\theta}_c$. Combining Equation 6.3 and Equation 6.4 gives the self-consistency condition for transverse electric fields:

$$\tan \left(\pi \frac{d}{\lambda} \sin \theta - m \frac{\pi}{2} \right) = \left(\frac{\sin^2 \bar{\theta}_c}{\sin^2 \theta} - 1 \right)^{\frac{1}{2}}$$

Equation 6.5

This is a transcendental equation of the variable $\sin \theta$ whose solutions yield the bounce angle θ_m associated with m . The θ_m values are quantized. A graphical solution is helpful for understanding this relation. The right- and left-hand sides of Equation 6.5 are plotted in Figure 6.2 below.

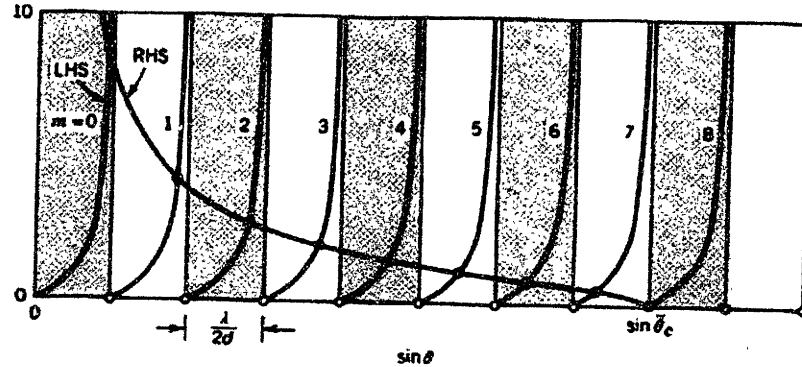


Figure 6.2: Graphical solution of Equation 6.5 to determine the bounce angles θ_m of the modes of a planer dielectric waveguide. The RHS and LHS of Equation 6.5 are plotted versus $\sin \theta$. The intersection points, marked by filled circles, determine $\sin \theta_m$. Each branch of the tan or cot function in the LHS corresponds to a single mode. In this plot $\sin \bar{\theta}_m = 8(\lambda/2d)$, and there are 9 modes [24].

The angles θ_m lie between 0 and $\bar{\theta}_c$. They correspond to wavevectors with components $(n_1 k_0 \sin \theta_m, n_1 k_0 \cos \theta_m)$. The z component is the propagation constant for the given mode

$$\beta_m = n_1 k_0 \cos \theta_m$$

Equation 6.6

These components must satisfy the condition

$$k_x^2 + k_y^2 \leq n_1^2 k_0^2 \sin^2 \bar{\theta}_c,$$

Equation 6.7

so that k_x and k_y lie in the area shown in Figure 6.3.

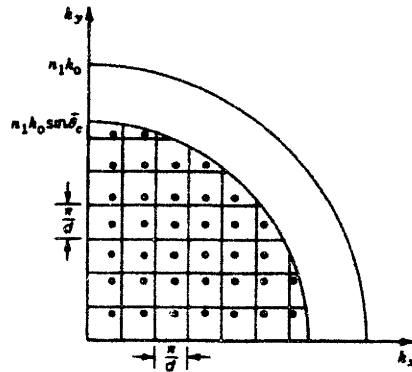


Figure 6.3: The values of k_x and k_y for the waveguide modes are marked by dots [24].

Assuming an average spacing of πd , the number of modes, M , can be approximated by

$$M \approx \frac{\pi (n_1 k_0 \sin \bar{\theta}_c)^2}{4 (\pi/d)^2} = \frac{\pi (2d)^2}{4 (\lambda_0)^2} NA^2$$

Equation 6.8

With

$$NA = \sqrt{(n_1^2 - n_2^2)} = n_1 \sin \alpha$$

Equation 6.9

being the numerical aperture of the waveguide. The numerical aperture is an expression of extent of the fiber's ability to accept non-normal incident rays, geometrically it is the sine of the vertex angle of the largest cone of meridional rays that can be guided in the core, multiplied by the refractive index of the core (see Figure 6.17b). This approximation for the number of modes is only good when M is large, and so

will not be found to be tremendously useful for our particular case. Instead, for our case, the allowable modes must be determined from Equation 6.5 and checked to see that they satisfy the Equation 6.7 condition.

The mode profiles may be exactly determined only for a slab waveguide structure: the core (n_1) is an infinite plate in the x - z plane of constant thickness d sandwiched in the y -direction between the substrate below (n_2) and the cladding above (n_2). Our waveguide has a square-cross section (n_1) in the x - y plane, and surrounded on all sides by cladding (n_2) so the Marcatili method will be used in Section 6.2 to determine the mode profiles [38]. In both guides, the wave propagates in the z -direction.

The internal field of the slab waveguide is composed of two transverse electromagnetic (TEM) waves traveling at angles θ_m and $-\theta_m$ with the z axis with wavevector components $(0, \pm n_1 k_0 \sin \theta_m, n_1 k_0 \cos \theta_m)$. They have the same amplitude and a phase shift $m\pi$ (half of that round trip) at the center of slab. Though consideration of both the electric (TE) and magnetic (TM) fields is necessary to fully characterize the wave, only the TE mode is computed here. The field distributions for the TM modes may be determined in a similar manner. The electric field complex amplitude can be given by

$$E_x(y, z) = a_m u_m(y) u_m(x) e^{-j\beta_m z}$$

Equation 6.10

Where a_m is a constant, and

$$u_m(y) \propto \begin{cases} \cos\left(\frac{2\pi \sin \theta_m}{\lambda} y\right), & m = 0, 2, 4, \dots \\ \sin\left(\frac{2\pi \sin \theta_m}{\lambda} y\right), & m = 1, 3, 5, \dots \end{cases} \quad -\frac{d}{2} \leq y \leq \frac{d}{2}$$

Equation 6.11

Note that although the field is harmonic it does not vanish at the core/cladding boundary. As m increases, so does $\sin \theta_m$ causing the higher-order modes to vary more rapidly with y (Figure 6.4).

The external field must match the internal field at all boundary points $y \pm \frac{d}{2}$. It must therefore vary with z as $e^{-j\beta_m z}$. Substituting $E_x(y, z) = a_m u_m(y) u_m(x) e^{-j\beta_m z}$ into the Helmholtz equation $(\nabla^2 + n_2^2 k_0^2) E_x(y, z) = 0$, one obtains

$$\frac{d^2 u_m}{dy^2} - \gamma_m^2 u_m = 0$$

Equation 6.12

Where

$$\gamma_m^2 = \beta_m^2 - n_2^2 k_0^2$$

Equation 6.13

Since $\beta_m > n_2 k_0$ for guided modes (see Figure 6.3), $\gamma_m^2 > 0$, so that Equation 6.12 is satisfied by the exponential functions $\exp(-\gamma_m y)$ and $\exp(\gamma_m y)$ in the y -direction. Since the field must decay away from the core,

$$u_m(y) \propto \begin{cases} \exp(-\gamma_m y), & y > \frac{d}{2} \\ \exp(\gamma_m y), & y < -\frac{d}{2} \end{cases}$$

Equation 6.14

The decay rate γ_m is known as the *extinction coefficient* and has units of inverse length. The wave existing in the cladding is called the evanescent wave associated with the propagating wave in the core. Substituting Equation 6.2 and Equation 6.6 into Equation 6.13 gives the extinction coefficient as

$$\gamma_m = n_2 k_0 \left(\frac{\cos^2 \theta_m}{\cos^2 \theta_c} - 1 \right)^{\frac{1}{2}}$$

Equation 6.15

As the mode number m increases, θ_m increases, and γ_m decreases. Therefore, higher-order modes penetrate deeper into the cladding. The inverse of the extinction coefficient, γ_m^{-1} , gives the length beyond the

interface that the intensity of the field drops by $1/e$. It is a very useful parameter for judging the depth of penetration.

To determine the proportionality constant in Equation 6.10 the internal and external fields must be matched at $y=\pm d/2$ and normalized by

$$\int_{-\infty}^{\infty} u_m^2(y) dy = 1$$

Equation 6.16

This gives an expression for $u_m(y)$ that is valid for all y and m as illustrated in Figure 6.4.

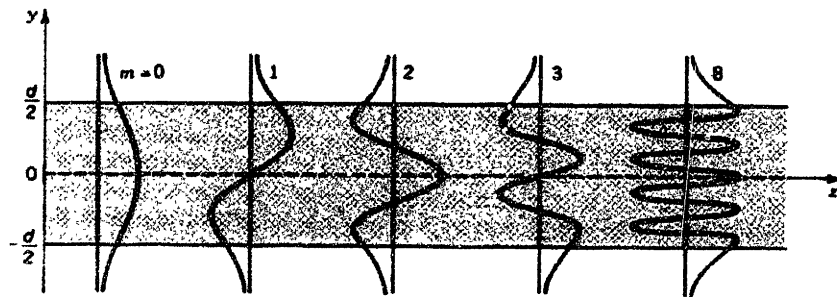


Figure 6.4: Arbitrary waveguide modes [24]

To summarize the equations presented in this section, the important parameters and their qualitative effects are given in Table 6.1.

Table 6.1: Important Waveguide Physical Parameters. Juxtapose this with Table 2.2 on page 23.

Physical Parameter	If this is larger...	It leads to...
Index Contrast	$\frac{n_1}{n_2}$	<ul style="list-style-type: none"> Greater field confinement in core region
Numerical Aperture	$\sqrt{(n_1^2 - n_2^2)}$	<ul style="list-style-type: none"> Larger angle of acceptance rays into waveguide core
Relative Length	$\frac{2d}{\lambda}$	<ul style="list-style-type: none"> More possible modes
Mode number	M	<ul style="list-style-type: none"> More change of field strength across core

In this present study, the goal is to produce fundamental mode ($m=0$) transmission of $\lambda=1.55\mu\text{m}$ wavelengths.

Section 6.2 Solution of Waveguide Equations

The solutions of the equations of the previous section, for our design specifications, are presented here. The refractive index of $\text{Si}_{1-x}\text{Ge}_x$ for a given Ge concentration depends strongly on the processing method, system cleanliness, and presence of dislocations. Index contrast measurements were performed to determine that the following condition holds our Si/SiGe/Si waveguides[34].

$$n_{\text{Si}_{1-x}\text{Ge}_x} = n_{\text{Si}} + 1.0(x)$$

Equation 6.17

Using Equation 6.17 and Equation 6.2, the values for the critical angle and complementary critical angle are given in Table 6.2.

Table 6.2: n_{SiGe} critical angle, complementary critical angle, and core wavelength

n_{SiGe}	θ_c	θ_c'	λ for $\lambda_c=1.55\mu\text{m}$
3.52	83.889°	6.111°	0.441 μm

Using these values, and solving equations Equation 6.5, Equation 6.6, Equation 6.9, and Equation 6.15 the values for the numerical aperture, bounce angle, propagation constant, and extinction coefficient are given in Table 6.3. The condition of Equation 6.7 limits the θ_m values, so the allowable values are shown in boldface type. Only single-mode propagation is permitted in these waveguides. This is a desirable result since higher order modes spatially divide the field intensity in the waveguide core, whereas the fundamental mode places the field maximum in the center of the guide. Multimode transmission is further complicated because each mode has its own propagation constant and velocity. This gives rise to modal dispersion as some modes lag and precede others, resulting in decreased transmission distance.

Table 6.3: NA, θ_m , β_m , γ_m^{-1} , and the condition of Equation 6.7 for $n_1=3.52$ and $n_2=3.5$.

d	2 μm	3 μm
NA	0.375	
M	0.732 \approx 1	1.646 \approx 2
m	0	0, 1
θ_m	3.701°	2.89° , 5.464°
RHS of Equation 6.7	1.516 μm^{-2}	2.298 μm^{-2}
β_m	14.21 μm^{-1}	14.22 μm^{-1} , 14.18 μm^{-1}
γ_m^{-1}	0.830 μm	0.749 μm , 1.476 μm

The Marcatili method was used to calculate the mode profile of the light traveling inside the waveguide [38]. In this method, the cross-section of the waveguide and neighboring cladding regions are subdivided as shown in Figure 6.5. Areas 1, 2, 3, and 4 have constant refractive index, n_2 , and the core in the center, has index n_1 . A rigorous solution of Maxwell's equations to this boundary-valued problem requires extensive computations [39], however it is possible to introduce a simplification that permits a closed form solution. For well-guided modes the field decays exponentially in areas 1, 2, 3, and 4 (Equation 6.14), and most of the field travels in the core (Equation 6.11), and even less travels in the un-numbered areas. Consequently, only a small error is introduced if the fields are only matched along the core's borders with the numbered areas—hence the refractive indices for the unnumbered areas are not specified. To match the fields at these four boundaries, the problem of a square cross-section waveguide is broken into that of two, perpendicular slab waveguides. The modes inside these slabs computed by the method given in Section 6.1 independent of each other. These solutions are then combined by simply assigning the value of the field in x-direction as that given by the slab with thickness d_1 , and the field in the y-direction is given by the slab of thickness d_2 . So, in the core the field varies sinusoidally in both x- and y- directions, in areas 2 and 4 it varies exponentially in the x-direction and sinusoidally in the y-direction; in area, and in areas 1 and 3 it varies sinusoidally in the y-direction and exponentially in the y-direction. The model does not apply in the un-numbered regions.

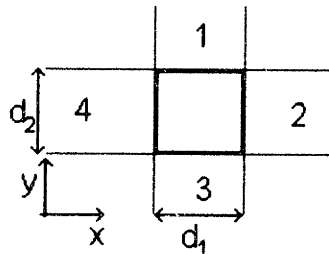


Figure 6.5: Waveguide cross-section divided by the Marcatili method

Marcatili presents a comparison of the results achieved by this method with other more exact methods of calculating the mode profile (Figure 6.6). The abscissa is the normalized height of the guide

$$\frac{2b}{\lambda} \sqrt{(n_1^2 - n_4^2)}$$

Equation 6.18

which the observant reader should recognize contains the numerical aperture from Equation 6.9 as a factor. The ordinate is a normalized function of the wavevector, given as

$$\frac{k_z^2 - k_4^2}{k_1^2 - k_4^2}$$

Equation 6.19

which varies between 0 and unity. It is 0 when $k_z=k_4$, describing a guide that is too small to support a mode, and the penetration depth is ∞ . It is unity when the guide is so large that $k_z=k_1$, and the entire field travels in the core, and the penetration depth is zero. The field components perpendicular to the axis of propagation (z-axis) are transverse electro-magnetic waves, E_{pq}^x and E_{pq}^y . The subindices, p and q indicate the number of extrema of the electric or magnetic field in the x and y directions, respectively. It can be shown that since

$$\frac{1}{n_1}(n_1 - n_4) \ll 1$$

Equation 6.20

the E_{pq}^x and E_{pq}^y modes are degenerate, so for the fundamental mode: $E_{11}^x = E_{11}^y$.

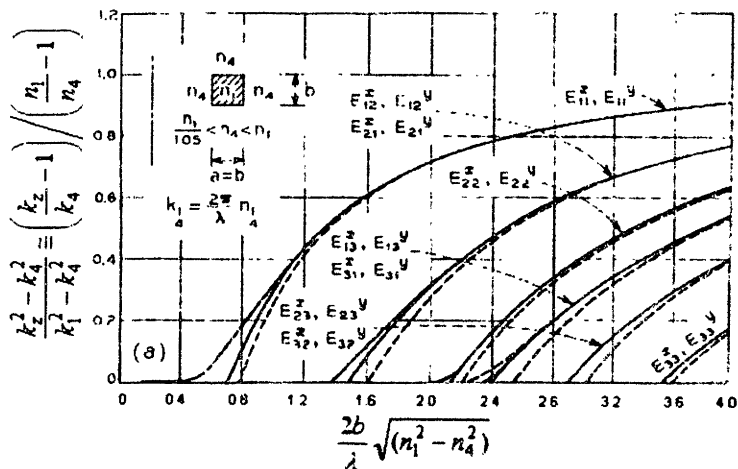
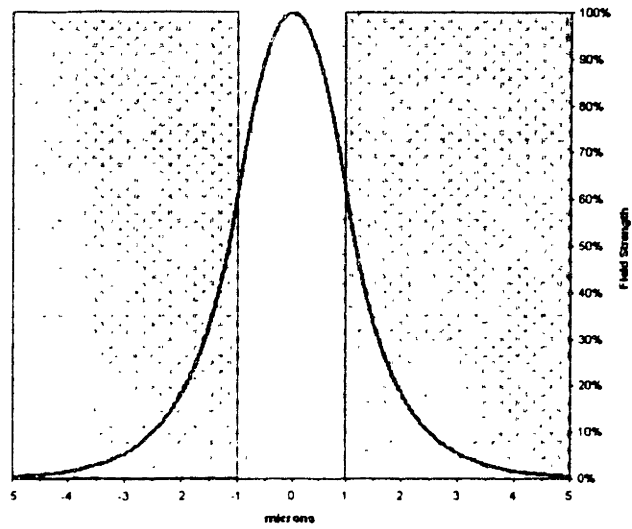


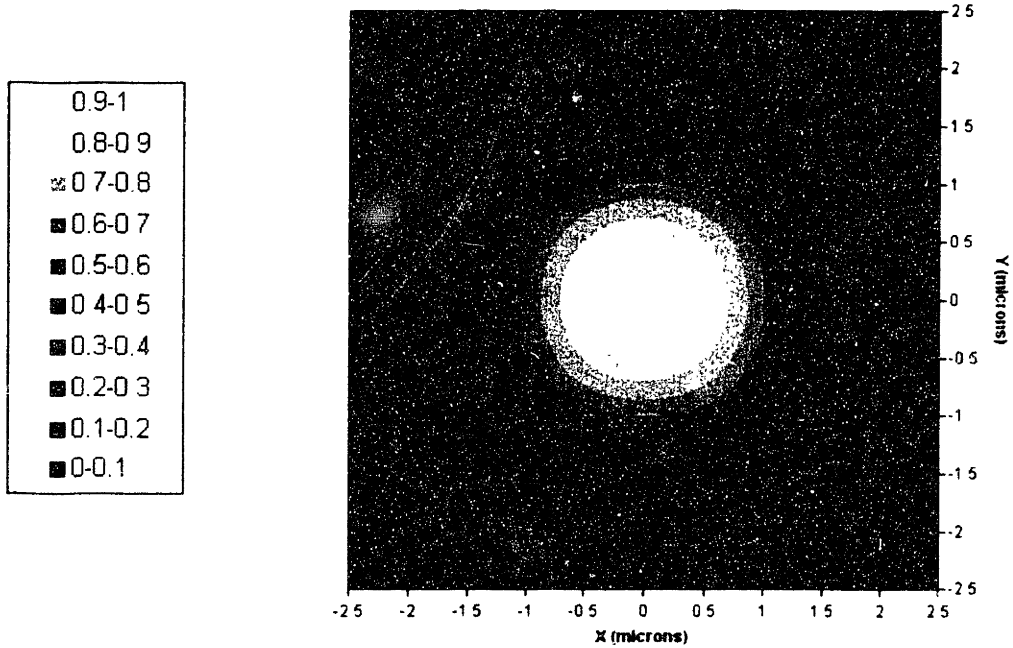
Figure 6.6: Propagation constant for different modes and guides. ——— transcendental equation solutions; - - - - - closed form solution; — · — · — computer solution of the boundary value problem [39]. [38]

The solid curves were obtained using the exact numerical solutions of the transcendental equations of [38] and the dashed curves are the result of the Marcatili method approximations. The dot-dashed lines represent the computer solutions of Maxwell's equations with the complete boundary conditions [39]. There is very good agreement between the all three solutions, so this method can confidently be used to yield satisfactory results for the present geometries.

Returning to the values given in Table 6.3, Figure 6.7 and Figure 6.8 plot the mode profile for the $2\mu\text{m}$ and $3\mu\text{m}$ square cross-section waveguide. These models represent the electric field profile for idealized un-graded waveguides. This data is presented as the profile along the x- or y-axis, passing through the center (Figure 6.7a and Figure 6.8a). It can also be viewed as contour map of the field strength as seen by looking down the z-axis of the waveguide (Figure 6.7b and Figure 6.8b). Here, each shade of gray is a 10% division of the field strength, with the maximum at the center. It can be seen that the field strength decays rapidly into the cladding for both size waveguides, but the larger, $3\mu\text{m}$ guide, contains a higher fraction of the field inside the guide. The bell shape is characteristic of the fundamental mode.

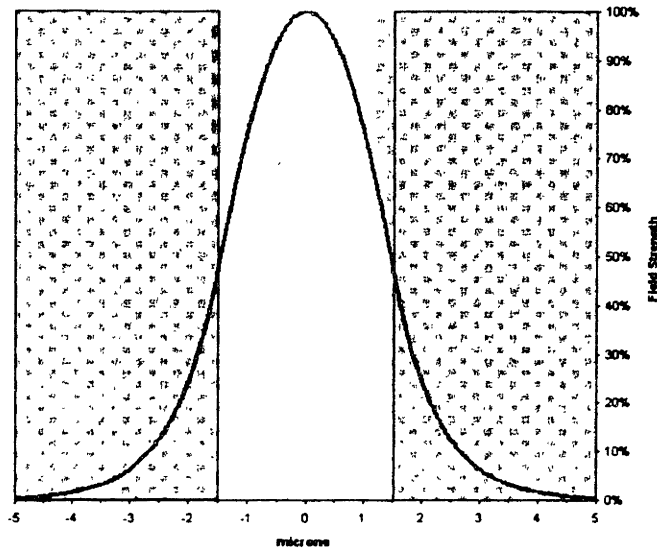


(a)

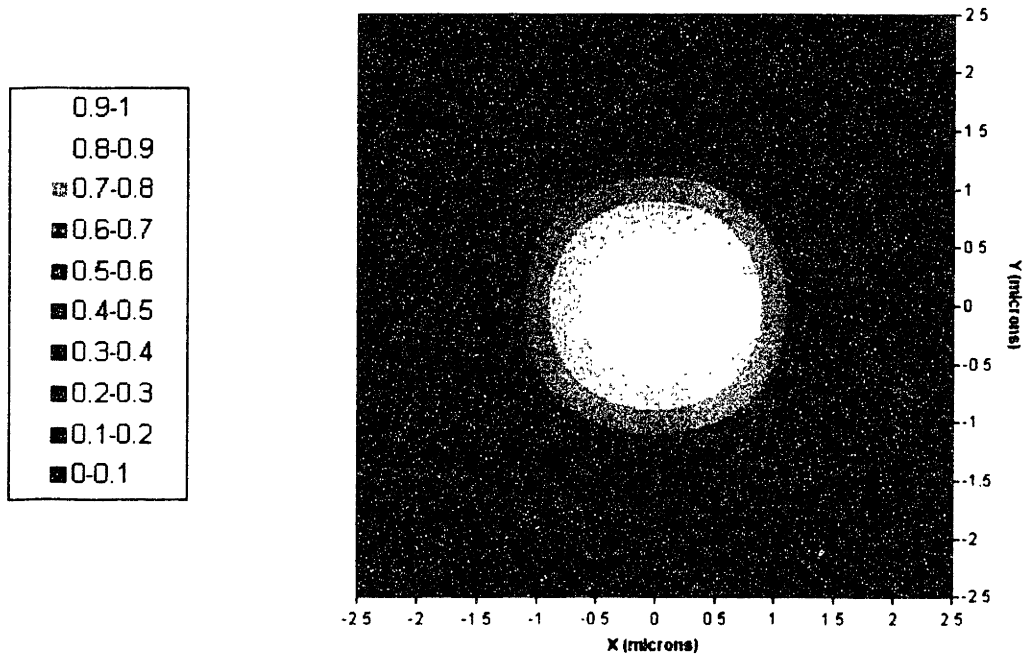


(b)

Figure 6.7: Electric field distribution in and around $2\mu\text{m}$ square cross-section waveguide:
 (a) 2D field distribution; (b) Contour map



(a)



(b)

Figure 6.8: Electric field distribution in and around $3\mu\text{m}$ square cross-section waveguide: (a) 2D field distribution; (b) Contour map

It is known from **Section 4.1** that the fraction of Ge incorporated into the film varies across the wafer for during deposition. Since the index contrast depends linearly on the Ge fraction by Equation 6.17, the variation in γ^l gives insight into how the decay of the evanescent field changes with Ge fraction.

Figure 6.9 charts this variation for a 3 μ m square cross-section waveguide embedded in an Si cladding of $n_1=3.5$.

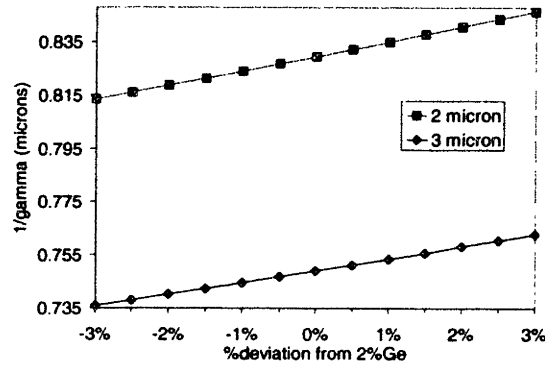


Figure 6.9: Change of γ^l with Ge fraction for 2 μ m and 3 μ m waveguides, $n_2=3.5$.

Section 4.1 discussed the issues associated with obtaining uniform, controllable thickness for SiGe layers. For non-selective deposition, the masking and lithography steps also introduce thickness non-uniformities in waveguide core and cladding layers. These variations correspond to distortions in the ideal square cross-sectional geometry. The effect of this on the extinction coefficient is more significant for the nominally smaller waveguide width, but is relatively minor overall, as can be seen from Figure 6.10,

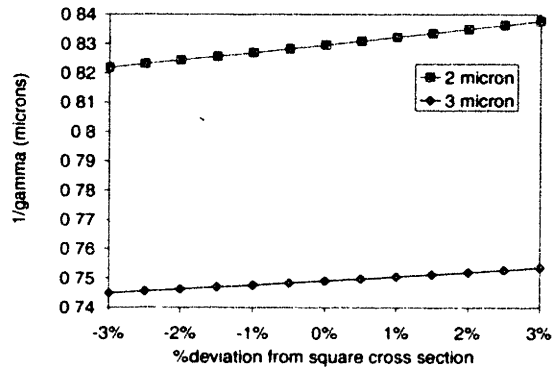


Figure 6.10: Change of γ^l with waveguide height $n_1=3.52$ and $n_2=3.5$ for 2 μ m and 3 μ m waveguides

In this section, the waveguide equations of section Section 6.1 have been solved for the square cross-section waveguide and low Ge fraction core using the Marcattili method. It has been shown that for this design the field intensity decays rapidly into the cladding layers, with most of the light being



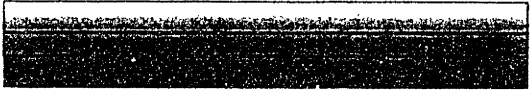


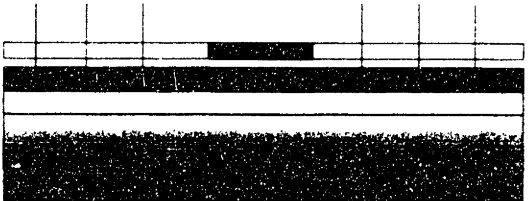

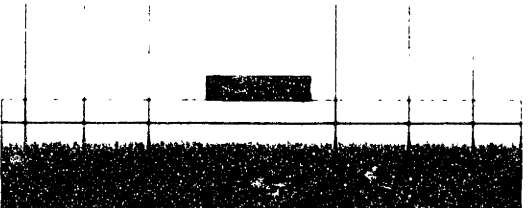
propagated along the core. The effect of changes in the Ge fraction and core thickness have been shown to have a small effect of the decay rate. The next section describes how the waveguides used in this research were fabricated.

Section 6.3 Waveguide Fabrication

The first round of research was conducted to determine the optimum growth conditions for the waveguides. The waveguide process flow is shown in Figure 6.11 for the matrix of growth conditions given in Table 6.4. As can be seen the matrix includes a variation in the thickness of the above and below graded layers, the thickness of the core and upper cladding layer. The grading in Ge concentration was done symmetrically by controlling the GeH_4 gas flow by mass flow controllers, so that the same thickness appeared above and below the ungraded layer, and the rate of variation was the same for both graded layers. For samples with graded layer, the grading rate was chosen to be $10\% \text{Ge}/\mu\text{m}$, such that the compressive strain is relaxed gradually so the growing graded layer always remains below the critical thickness as it grows. The endpoints of the grade were chosen such that they increased from the zero, at the lower or upper cladding boundary, to the Ge concentration at the boundary with the core. The range for the core thickness was chosen in response to the demands by the telecommunications industry for interfacing with optical fibers. The thickness of the lower cladding layer was chosen to be sufficiently thick to prevent the diffusion of contaminants from the substrate into the core region of the waveguide where they can contribute to the optical losses. The thickness of the upper cladding region was chosen to be much greater than the sum of the core and lower thicknesses, such that the light traveling in the waveguide sees the cladding in all directions as infinitely thick.

Waveguide Processing Step

Diagram (not to scale)

Bake starting Si wafer substrate to remove native oxide	
Deposit lower Si cladding layer	
Deposit lower $\text{Si}_{1-x}\text{Ge}_{0-x}$ graded layer (optional)	
Deposit $\text{Si}_{1-x}\text{Ge}_x$ core layer	
Apply backside anti-reflective coating and spin-on negative photoresist	
Expose photoresist through dark-field mask	
Remove exposed photoresist	
Deep reactive ion etch core & lower cladding using $\text{CF}_6/\text{C}_4\text{F}_8$ ions in a Decoupled Plasma Chamber	

Pattern $\text{Si}_{1-x}\text{Ge}_x$ core and lower cladding



Strip photoresist.

RCA clean:

75-80°C

a) 10-15mins, 5:1:1 $\text{H}_2\text{O}:\text{NH}_4\text{OH}:\text{H}_2\text{O}_2$

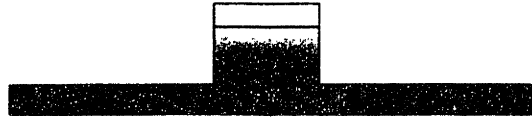
b) 15sec, 10:1 $\text{H}_2\text{O}:\text{HF}$

20sec, cold rinse

75-80°C

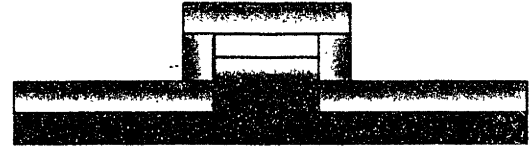
d) 10-15mins, 6:1:1 $\text{H}_2\text{O}:\text{HCl}:\text{H}_2\text{O}_2$

e) cold rinse and dry



Bake to remove oxide.

Deposit reverse upper $\text{Si}_{1-x}\text{Ge}_x \rightarrow 0$ graded layer
(used only if lower graded layer is used)



Deposit Si upper cladding layer.
A pyramid formed by crystal planes were observed
above the waveguide core.

Structure is now complete.

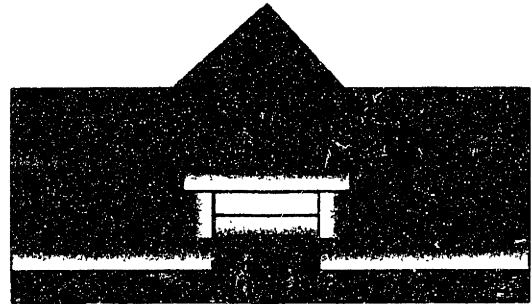


Figure 6.11: Waveguide process flow

Table 6.4: Deposition conditions for waveguide samples

Core	Symmetric Grade	Capping Layer	Total Thickness
2-3 μm	0-0.25 μm	6-9 μm	8-12 μm

The SiH_4 , GeH_4 , and H_2 gas flow rates and wafer temperatures were chosen to give a low germanium (2%Ge) concentration because the absorption coefficient and refractive index are close to silicon (Figure 2.8 & Figure 2.9). As importantly, the lower germanium concentration reduces the strain and increases the critical thickness and increases the critical thickness.

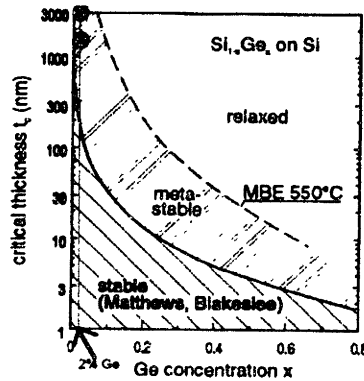


Figure 6.12: Both the $2\mu\text{m}$ and $3\mu\text{m}$ core regions are in the metastable range

The waveguide cores should be in the metastable phase. Figure 2.2 is reproduced above as Figure 6.12 with the approximate locations of the $2\mu\text{m}$ and $3\mu\text{m}$ cores, without grades. Films in the metastable phase are in a non-equilibrium state. Low-Pressure CVD is suited for generation of metastable structures, because deposition operates in the low temperature, kinetically-limited regime when non-equilibrium structures are formed. LPCVD employs fine temperature control and high system cleanliness to prevent the unwanted nucleation of dislocation. Dislocation density ($\text{dislocations}/\text{cm}^2$) is therefore expected to be low in this regime. Furthermore, compared to the wavelength of light there are expected to be very few interactions between the standing wave and any core dislocations.

XRD scans were taken to determine the substitutional Ge concentration and degree of relaxation. Figure 6.13 shows two such scans taken on a blank deposition of $3\mu\text{m}$ without a grade; one scan was taken at the center of the wafer, and the other 3mm from the edge. There is a variation in the Ge concentration across the wafer: 1.6% at the center and 1.4% at the edge, which is evident from the figure because the edge SiGe peak is closer to the substrate and therefore has less strain. By comparison with the asymmetric scan, it was determined that there was no relaxation in the film. This measurement does not mean there are no dislocations, however, because the sensitivity of XRD may not be enough to detect a low dislocation

density. However, after the remaining processing steps necessary to form the waveguide (patterning & high temperature bake), it is expected that film relaxation may occur.

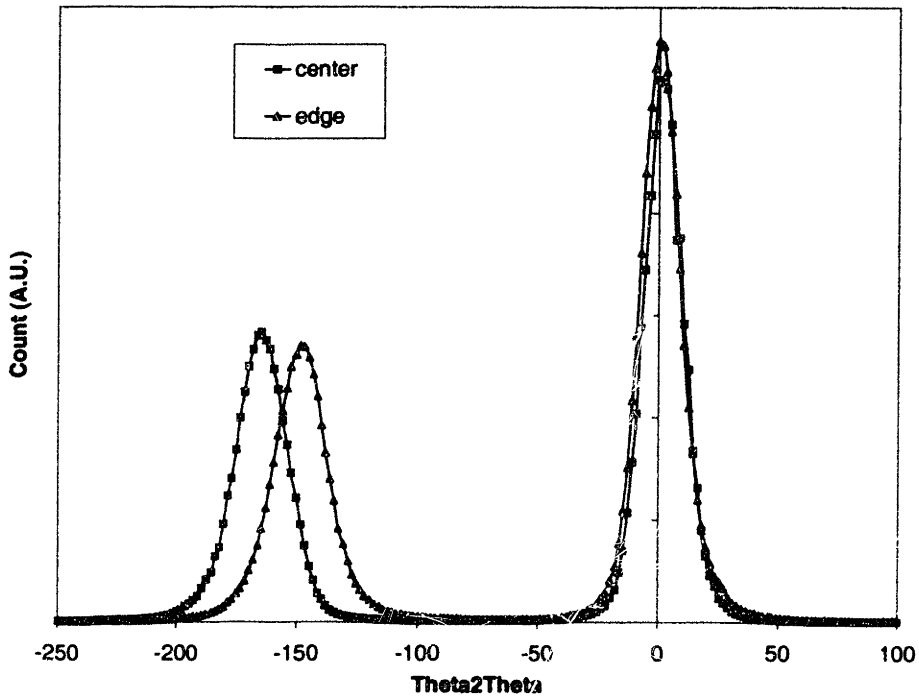


Figure 6.13: Symmetric (004) XRD scans on 3µm thick, with no grade sample

All of the waveguide structures were examined by microscopy. Optical microscopy showed no evidence of cross-hatching on the surface of some samples, which is ambiguous. Cross-hatching is a square-like pattern visible on the wafer, and results from the pattern threading dislocations form on the surface. If the film is completely strained, no threading dislocations exist, and no cross-hatching. However, if there is only a minimum of relaxation, the cross-hatch may not be present either. Nevertheless, if the Ge concentration is low (a few percent) and the surface does have a cross-hatch, then relaxation has definitely occurs. The sample shown in Figure 6.15 was processed under conditions that did give rise to cross-hatching. Under high magnification an “extended pyramid” structure was observed above the core line (Figure 6.14). This is a result of uniformly thick upper cladding layer conformably covering a surface with the protruding core. The structure forms a pyramid along an oblique crystalline plane. This pyramid structure was also observed to form above defects (Figure 6.15). The SEM of Figure 6.14b indicates that

growth was continuous from lower cladding to core to upper cladding, and that no voids were present in the structure.

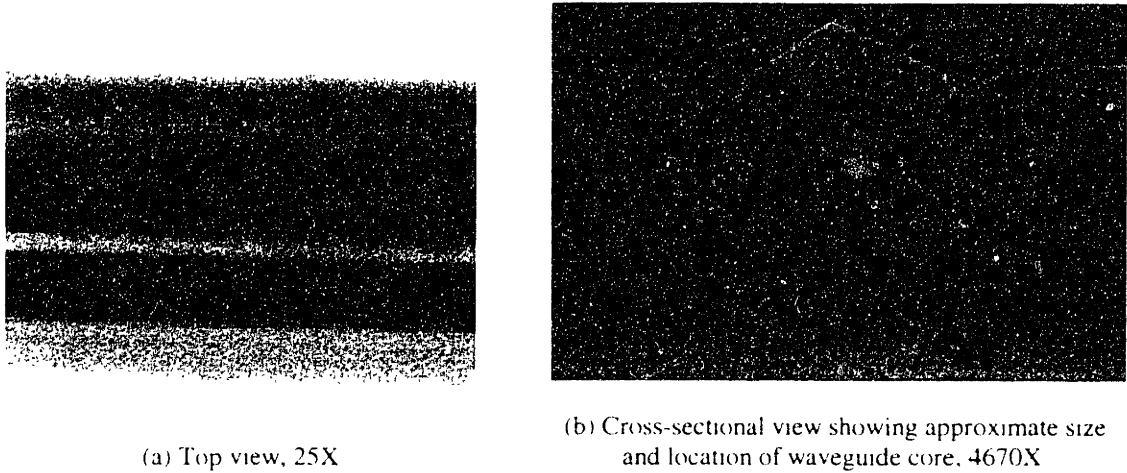


Figure 6.14. Optical micrograph and Scanning electron micrograph of waveguide structure

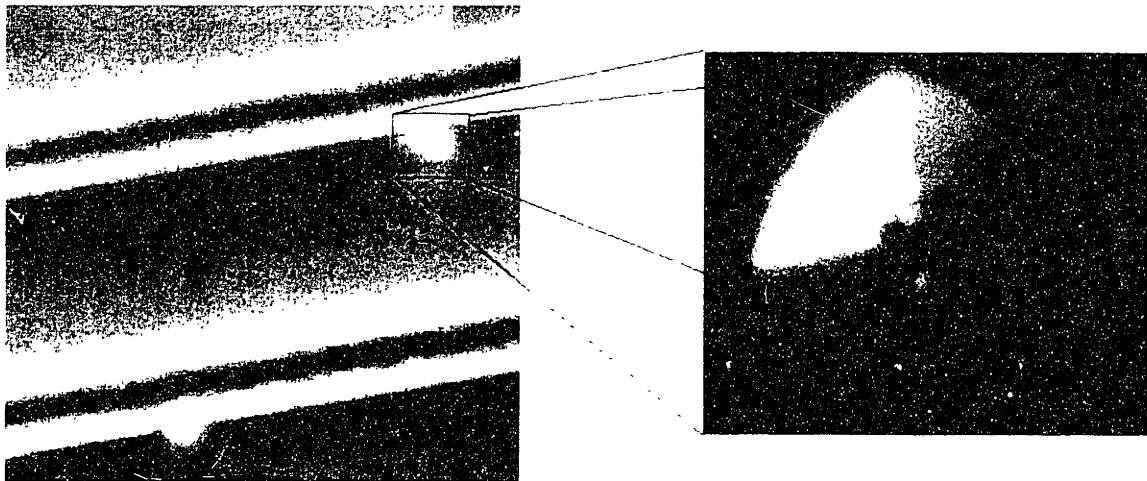


Figure 6.15 Optical micrograph showing defectivity near waveguide
Left image is 3.6X magnification, enlarged image is 36X

The sidewalls of the core were examined after etching to ascertain the roughness. It is desirable to have this surface as smooth as possible to avoid scattering by this surface [22]. Figure 6.16 presents an SEM micrograph of the sidewall just after DRIE etching. The rippling is a result of the pattern transfer

from the photoresist and not from the etch itself. The scale of this roughness may be sufficient to contribute to transmission loss.

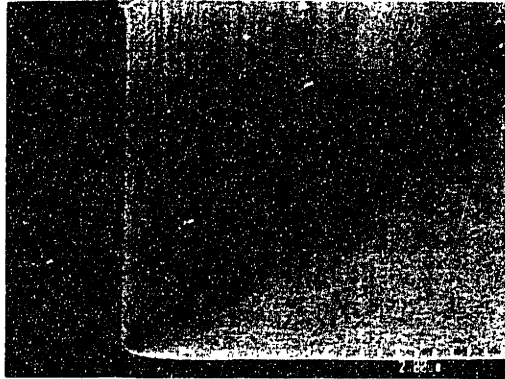


Figure 6.16: SEM micrograph of sidewall roughness after DRIE

Section 6.4 Optical Loss Measurements

The most critical parameter for any transmitting conduit is the signal loss over distance. A low loss value is desirable because it allows for increased distance between signal amplifiers and for signal transmission with less power. Due to material absorption, sidewall scattering, and interactions with defects the intensity of the signal inserted in one end of an optical waveguide decays exponentially with distance. In this section, the results of loss measurements performed on the waveguides fabricated in the previous section are presented.

Optical attenuation measurements were performed at MIT and Bell Laboratories for the transmission at the $1.55\mu\text{m}$ wavelength. $1.55\mu\text{m}$ is one of two commonly used wavelengths in optical fiber transmission (the other being $1.3\mu\text{m}$) because of its low attenuation in silica glass—the core optical fibers. The experimental apparatus used a tunable diode laser to generate the input optical power that is piped with optical fiber. The signal is passed through an in-line polarizer and delivered to the insertion face of the waveguide. Light travels through the waveguide and a lens focuses it through a pinhole. It is then received by a detector that measures the output power. For alignment purposes, the light can instead be reflected into a CCD camera that produces an image of the IR beam on a TV monitor (Figure 6.18). This apparatus is shown in Figure 6.17

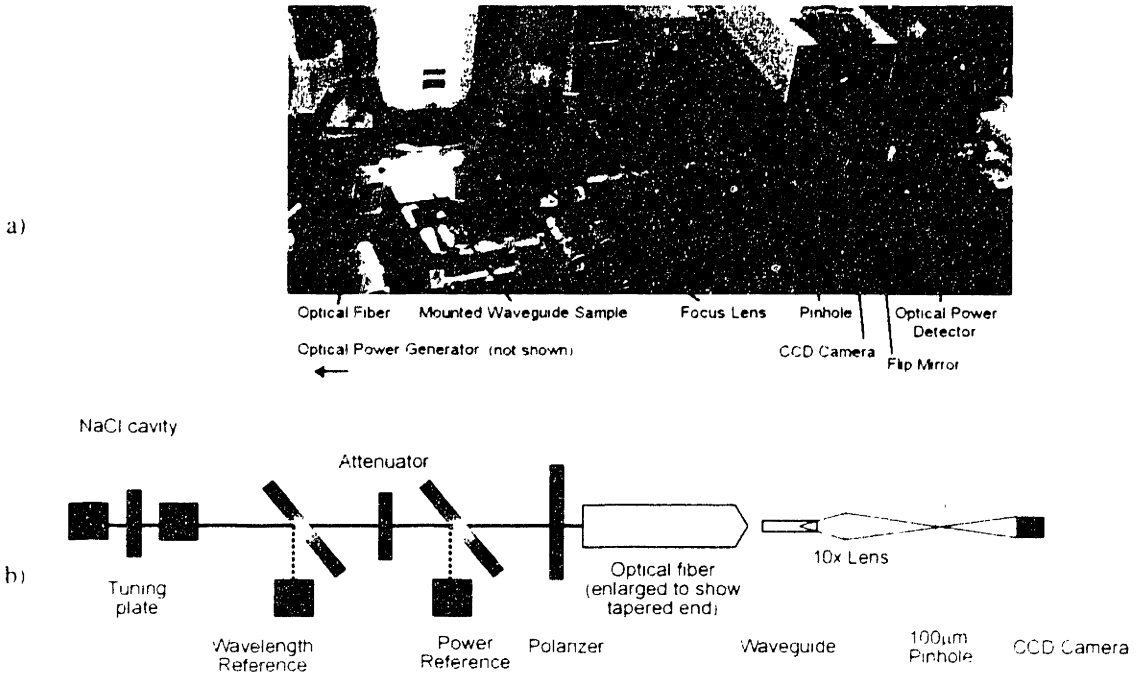


Figure 6.17: Optical Loss Measurement Apparatus (a) photograph; (b) diagram with ray tracing (not to scale)

The input optical power, P_i , and output optical power, P_o , are related by the following equation

$$P_o = \eta P_i e^{-\alpha x}$$

Equation 6.21

In this equation, η is the coupling efficiency between the measurement apparatus and the waveguide, α is the attenuation coefficient, and x is the distance the light propagates in the guide. The transmission loss, α_T , is the more commonly quoted parameter and can be obtained from the attenuation coefficient by multiplying with 4.3

The cutback technique was used to measure optical loss in waveguides. The cutback technique is a destructive method for obtaining α_T in the waveguide by repeating the loss measurements on known lengths of the same waveguide. Light of a known power is inserted into the waveguides and the exiting powers are measured. The sample is then "cutback" and the measurement repeated. From a plot of $10 \log(P/P_0)$ versus sample length, α_T is the slope and η is given by $10^{(10 \times \text{intercept})/10}$. α can also be obtained by plotting $\ln(P/P_0)$ versus sample length.

If the results from the cutback technique indicate that the insertion loss value is close to value of the attenuation loss, then an alternative technique should also be used. Since the insertion loss is experienced at each measurement of a cut length, its large value could cloud the true transmission loss of the waveguide. The Fabry-Perot resonance measurement is an alternative technique for measuring the transmission loss in low-loss waveguides. This technique uses the resonance of the optical mode in the waveguide, reflected by the end facets to determine α_T . The two facets of the waveguide are polished to have high reflectivities, forming a resonant cavity between them. Like the cutback method, light is inputted into one end and the output is measured at the other, however by changing either the length of the sample or the input wavelength, the output power switches between constructive, P_{max} , and destructive interference conditions. P_{min} . The transmission loss can be obtained from the ratio of these two extremes by

$$\alpha = \frac{1}{d} \ln \left(R \frac{1 + \sqrt{\frac{P_{min}}{P_{max}}}}{1 - \sqrt{\frac{P_{min}}{P_{max}}}} \right)$$

Equation 6.22

Where the reflectivity, R , is given by

$$R = \left(\frac{n_1 - n_0}{n_1 + n_0} \right)^2$$

Equation 6.23

This measurement was not performed, but is strongly suggested for future research [22].

Loss measurements were performed on all of these samples using the cutback technique. The waveguide samples were prepared for loss measurements by these steps. The samples were cut on a die saw and were adhered by melted thermoplastic onto a quartz holder. The samples were wet polished on a polishing wheel using 1 μ m grit polishing paper for 1hr, 0.3 μ m grit paper for 15 minutes and 0.1 μ m grit paper for 15 minutes. The samples were cleaned with ethanol and mounted in the optical loss measurement apparatus. First, the background, or nominal zero, power was recorded so it could be subtracted from each measurement. Second, the output power of the laser is determined without the waveguide by moving the sample out of the light path and focusing. This value will serve as the P_i value. Using the xyz stage, the sample was brought into alignment with the optical fiber. Finally, several measurements were taken with

the waveguide in the light path to obtain P_o values. After several measurements are taken, the length of the sample was measured by a micrometer. The process was repeated for different lengths.

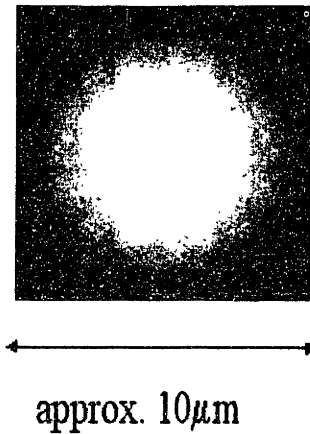
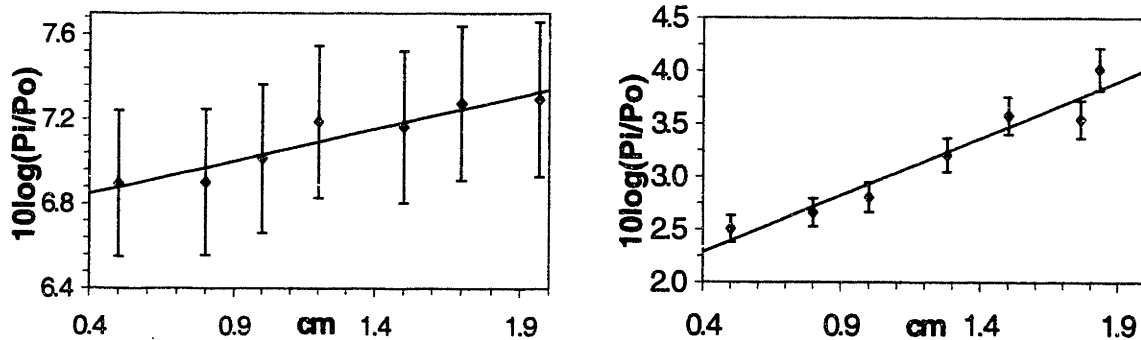


Figure 6.18: Image of light being transmitted through SiGe waveguide. Compare with model in Figure 6.8. 3 μ m core, no grade

The results of loss measurements performed on these samples are given in Figure 6.19.



(a) 3 μ m core, 0 μ m grade
 $\alpha = .072\text{dB/cm}$, $\alpha_T = 0.31\text{dB/cm}$, $\eta = 0.21\text{dB}$

(b) 2 μ m core, 0.5 μ m grade
 $\alpha = 0.25\text{dB/cm}$, $\alpha_T = 1.08\text{dB/cm}$, $\eta = 0.65\text{dB}$

Figure 6.19: Cutback measurement results on typical SiGe waveguides [34]

The lowest transmission loss achieved was $\alpha_T = 0.31\text{dB/cm}$. From the intercept, the insertion loss was determined to be $\eta = 0.21\text{dB}$. The structure consisted of a rectangular $\text{Si}_{0.98}\text{Ge}_{0.02}$ cross-section, measuring $3.2\mu\text{m} \times 3\mu\text{m}$, with $9\mu\text{m}$ of epitaxial silicon serving as the upper cladding layer, and several microns as the lower cladding layer. This sample had no graded layers.

This is a much lower loss value than previously reported in the literature. Vescan et al. fabricated SiGe strip waveguides with losses of 2.2dB/cm for $1.55\mu\text{m}$ transmission of transverse electric field

polarization [40]. That structure also consisted of multiple layers of Si and SiGe epitaxially deposited by LPCVD on a silicon substrate: 0.15 μm Si buffer layer, 0.38 μm Si_{0.8}Ge_{0.2} guiding layer, 0.63 μm Si_{0.98}Ge_{0.02} cap layer, and 0.002 μm Si cap layer. Temkin et al. also report a similar range of loss values, 2-3dB/cm [41].

Samples with grades showed a higher transmission loss values than those without (Figure 6.20). It is possible that the asymmetry introduced by the “above/below” grade increases the loss. It would be desirable to produce a more symmetric graded structure, with a grade both above and below the core, and to the right and left. For the samples with grade, the loss value increased with waveguide width. If one accepts that the loss is increased by the asymmetry induced by the grade, then this effect will be more noticeable for wider guides where more of the structure is a grade. There did not appear to be a significant variation in loss values for guides without grade of the same thickness.

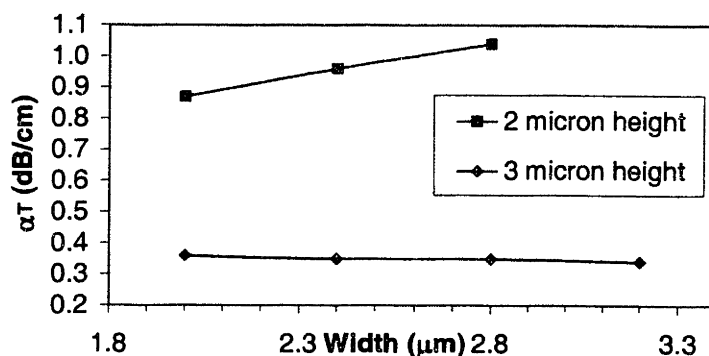


Figure 6.20: Variation in transmission loss with waveguide width

Section 6.5 Future Waveguide Test Structures

The next round of research was initiated to determine the losses encountered when waveguides turn bends, the degree of crosstalk between adjacent lines, and the conditions for coupling. Masks have been designed that contain the structures to be fabricated, though fabrication and testing of the structures has not yet been performed. It is expected that these structures will be fabricated according to the process flow of Figure 6.11 without a grade.

Modeling the beam profile along straight waveguides was relatively simple since the core cross-section remains constant in the propagation direction. The Marcatili method cannot be reliably used to

model the beam profile when the waveguide turns bends because the cross-section is distorted. Finite-Element methods divide the waveguide into an array of small discrete volume cells, and solve the waveguide equations using the boundary conditions of each cell (Figure 6.24). High resolution (small cell size) is needed to accurately model the profile, but this comes at the cost of long computation times.

Table 6.5: Parameter dimensions of structures and possible tests that may be performed using them

Figure	Name	Parameters	Possible Tests
Figure 6.21	Radial curves	$1 < r < 4\text{mm}$	<ul style="list-style-type: none"> - Test effect of bending radius on loss - Test effect of corner roughness on loss
Figure 6.22	Directional coupler	$1 < g_0 < 6\mu\text{m}$	<ul style="list-style-type: none"> - Test effect of signal coupling with inserting light in one guide and measuring emission from the other.
Figure 6.23	Y-branch signal splitter	$s_1=1\mu\text{m}$ $s_2=2\mu\text{m}$ $s_3=3\mu\text{m}$... $s_{10}=10\mu\text{m}$ $s_{11}=15\mu\text{m}$ $s_{12}=20\mu\text{m}$... $s_{67}=295\mu\text{m}$	<ul style="list-style-type: none"> - Test effect of splitting signal by inserting from main right branch and measuring in left branches - Test effect of combining signals by insert from one or both left branches and measuring in main branch - Y-structure can be cut off so that the effect of coupling between long parallel lines can be tested - As long parallel lines, the ability of our fabrication process to uniformly cover steps can be investigated.

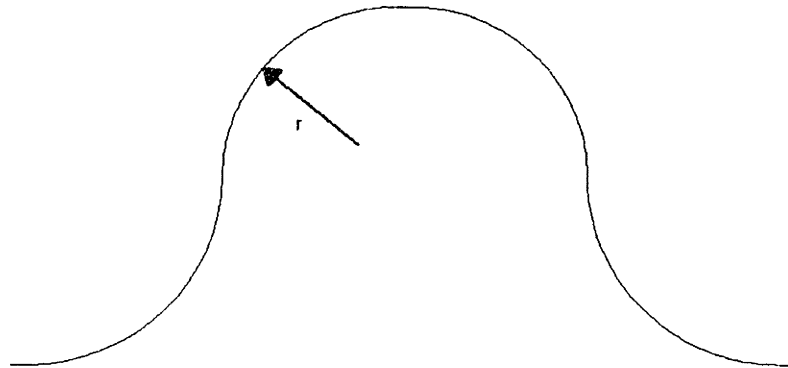


Figure 6.21: Radial curves

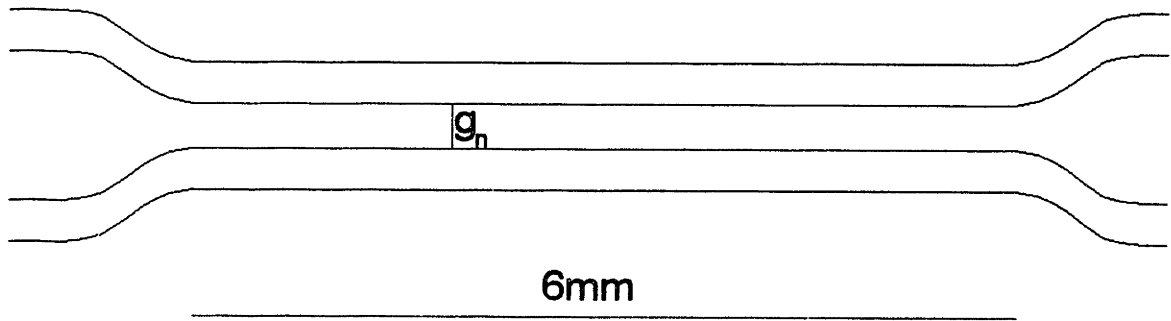


Figure 6.22: Directional coupler

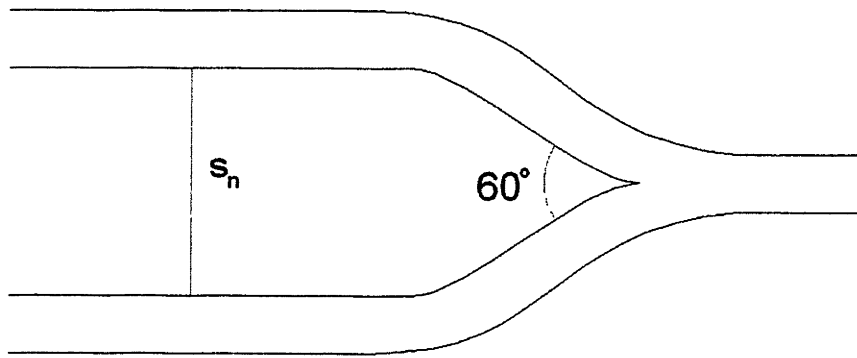


Figure 6.23: Y-branch splitter; both left branches extend to form long parallel lines

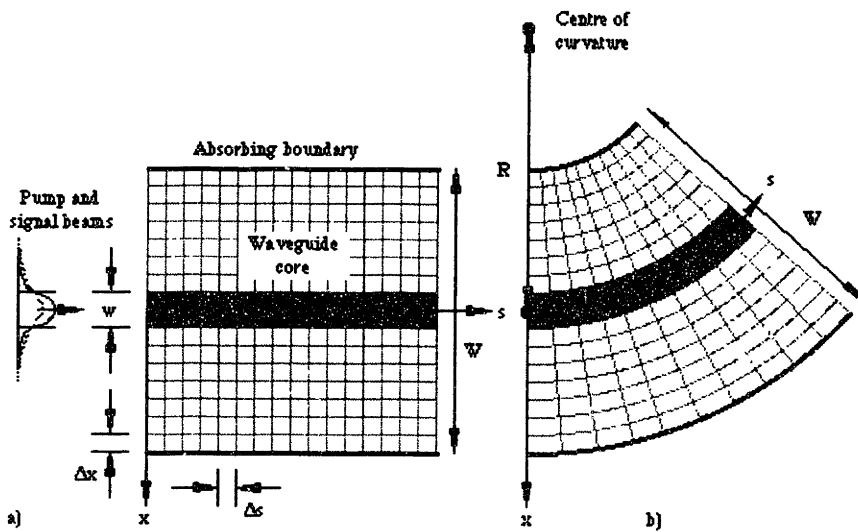


Figure 6.24: Finite-Element Array that may be used to model beam profile
 a) along straight section & b) turning bends

Chapter 7 Thesis Summary & Recommendations

The goal of this research was to demonstrate that LPCVD is a viable technique for fabricating SiGe waveguides. SiGe waveguides fabricated by LPCVD capitalize on the tunability of the optical and physical properties of the SiGe system, and the low cost and availability of silicon substrates to produce high-quality, low loss optical transmission conduits.

One purpose of this thesis was the development of Applied Materials' Epi Centura® LPCVD chamber for waveguide fabrication. New hardware was installed and tested to improve deposition uniformity and chamber purity. Process characterization was also conducted to determine conditions for selective deposition, polycrystalline deposition, and the suppression of B diffusion.

Another purpose of this thesis was the use of this chamber to fabricate square cross-section SiGe strip-waveguide structures. The Marcattili method was used to model the electric field mode profiles for this design. Waveguide structures of different shapes were designed and fabricated using the optimized LPCVD chamber. Optical attenuation measurements were obtained for these waveguide structures, demonstrating that low-loss transmission has been achieved.

Section 7.1 LPCVD Chamber Improvements

Sub-Section 7.1.1 Summary of Results & Conclusions

Hardware modifications were implemented and tested on the Epi Centura® LPCVD chamber to improve deposition uniformity and film purity. The hardware options considered were the inject orifice height, the presence or absence of flow straighteners, and the type of baffles used. It was found an orifice height of 1/8" with no flow straighteners and 7/7/7 baffles produced the most uniform flow conditions for high temperature depositions. The AccuSETT® valves were found to be effective at changing the thickness profile with the 7/7/7 baffle hardware. $1\sigma=0.58\%$ thickness uniformity was achieved using (150/60) AccuSETT® settings, 40/40/20 lamp power balance, and 25slm main H₂ flow at T=1000°C. A 3-zone lamp module was installed and tested to determine the most uniform heating profile for low temperature depositions. The 21/21/58 power ratio distribution produced a uniform deposition profile at

T=680°C for both thickness, $I\sigma=1.75\%$, and composition, $I\sigma=1.61\%$, (see Section 4.1). This uniformity is above the desired $I\sigma=1.00\%$, but is tolerable for waveguide fabrication since it does not cause a significant impact on the mode profile. The insertion of the Aeronex GateKeeper® Hydride Gas Purifier into the GeH₄ supply manifold decreased the O₂ concentration in the chamber from over 10¹⁹ atoms/cm³ less than the SIMS detection limit of 10¹⁷ atoms/cm³ (see Section 4.2).

Process characterization for SiGe deposition was conducted on the Epi Centura® LPCVD chamber. Low temperature process conditions were identified for selective growth on silicon, but not on oxide (see Section 5.1). The surface roughness of poly SiGe and poly SiGeC deposited on nitride and oxide was measured to be $R_{ms}=4.678\text{nm}$ and $R_{ms}=81.840\text{nm}$ (see Section 5.2). The incorporation of C to the SiGe lattice was found to suppress the diffusion of B by 41.75% compared to without C (see Sub-Section 5.3.1). Epitaxial films of the composition $\text{Si}_{0.965}\text{Ge}_{0.027}\text{C}_{0.00786}$ were shown to be lattice-matched to the Si substrate, and strain compensation was explored at other Ge fractions (see Sub-Section 5.3.2).

Sub-Section 7.1.2 Recommendations for Future work

At present, the “inner” and “middle” power zones heat more or less same inner region of the wafer, while the “outer” zone heats the edges. The distribution of the radiative heating could be improved by changing the reflectors such that more power is directed towards the “middle” region. Changing the flow balance using the AccuSETT® valves had a effect that is dependent on the particular baffles installed. The addition of a “middle” AccuSETT® valve might help to provide more flow to this region.

Further work is needed to identify higher throughput conditions for selective, low temperature deposition. At 722°C, the highest growth rate was 8Å/min, which is considered sluggish. It would be desirable to achieve growth rates above 20Å/min. Increasing the DCS flow rate should increase the growth rate, although 600sccm is already quite high. In addition, the techniques used in this work to detect the onset of growth on oxide are not very precise: nucleation islands in their early stages can be very small, and perhaps not visible by optical microscope. Further examination could be done using AFM to raster the surface, searching for nucleation islands. Though very sensitive to surface changes, AFM is very slow and generally applied only to small areas.

At low temperatures, the growth rate is severely depressed. Though the addition of Ge boosts the growth rate, alternative gas chemistries for silicon deposition should be explored. Thermal budget requirement demands for deposition processes are approaching the limits for standard precursor molecules to dissociate and deposit a complete epitaxial film. Either new precursors, with lower activation energies, or new mixtures that catalyze precursor dissociation, or remove the barriers to deposition, are needed.

Nucleation of polycrystalline SiGe is strongly influenced by the surface roughness. In future experiments, the deposited polycrystalline film might be made more smooth by first growing a thin layer of intrinsic epitaxial silicon on the oxide or nitride. This would serve as a more uniform, defect-free surface on which to nucleate the polycrystalline film.

Section 7.2 Waveguides

Sub-Section 7.2.1 Conclusions

Initial research was conducted to determine the optical properties of Si/SiGe/Si waveguides and the optimum processing conditions. The basic equations of waveguide transmission are presented and solved for a square cross-section SiGe strip waveguide structure (see Section 6.1 & Section 6.2). The Marcattili method was applied to the 2 μ m and 3 μ m square cross-section waveguides to show that only the fundamental mode is supported, which is desirable for device purposes. The mode profiles were mapped and plotted by this method. Modeling has shown that the small variations in Ge fraction and thickness indicated in Sub-Section 4.1.3 do not significantly impact the mode profiles. Straight waveguides were fabricated to explore the effects of core thickness, grade thickness, and capping layer thickness on the optical attenuation at 1.55 μ m (see Section 6.3). An optical attenuation of 0.31dB/cm was achieved (see Section 6.4). XRD scans showed that the Ge fraction in this sample was 1.6%, which deviates somewhat from the intended %Ge fraction of 2.0%, but still produces pseudomorphic structures below the critical thickness. In addition to straight waveguides, curved structures were designed to test waveguide field containment for different geometries. Section 6.5 discussed the fabrication of radial structures to determine the loss associated with different curvatures.

Sub-Section 7.2.2 Recommendations for Future Work

Advanced analysis methods exist for modeling the mode profiles in optical waveguides. The Marcatili method is a simple, semi-analytical technique that yields very accurate results for this simple geometry. Numerical methods such as the Beam Propagation Method can be used to solve Maxwell's equations exactly and are applicable to a wide variety of structures providing accurate results, often at the expense of long computational times [15]. The Spectral Index semi-analytical method is a popular technique for solving the waveguide equations and has been applied to structures with SiGe cores [40].

It should be possible to achieve an even lower loss value than 0.31dB/cm in further iterations of research. Using the structures fabrication in Section 6.5, experiments could be done to test the curvature loss and coupling efficiency. Some of the tests that could be conducted are listed in Table 6.5.

In the work, the cutback technique was used, although it is known that Fabry-Perot resonance measurements give more accurate loss values for low-loss waveguides. The Fabry-Perot apparatus was unavailable, although it is strongly recommended that it be employed for future loss measurements.

The systems analyzed in this work consisted of un-doped materials. It is known that doping with the standard electronic dopants does have an impact this system's optical transmission and detection properties, particularly the optical band gap and absorption coefficient. While dopants like oxygen negatively impact *passive* waveguides, other dopants may be used to form electronically activated optical devices. It is possible to use the principle of photodetection (and the reverse effect, photogeneration) to build a hybrid family of *active opto-electronic* devices which includes switches, emitters and detectors; all of which must ultimately be integrated with waveguides to form a useful network. In future works, the role of dopants in this waveguide design should be further investigated.

The telecommunications industry has been the fastest growing business sector, and is predicted to be so for many years to come. At the heart of this powerful infrastructure are the myriad of chips and circuits, they are the Pentiums humming in our laptops and the routers guiding the flow of Internet traffic. The limitation to improving these chips today is often not better software, but better materials. The mantra “smaller, faster, cheaper” has long hailed the advantages realized by reliably fabricating complex electronic circuitry at the micron scale and smaller ($<1/1000000\text{m}$), but even this has its limits. The Silicon Age got its start in electronics, but it does not have to end there. This research has shown that not only is it possible to use silicon for optical applications, it is inevitable. Mankind first shaped his world by smashing bone and stone, and today we create devices by precisely arranging atoms and guiding photons. We have advanced in countless ways, but one theme is impermeable: any task can be done, provided one has the proper tools.

Chapter 8 Acknowledgements

Ahhh...the “Acknowledgements”—the one chapter when the shackles of objectivity and muzzle of the passive voice are removed. I am now free to use the first person and speak in the present tense. Scientific writing is very effective at conveying the facts, theories, experiments, and logical conclusions of life. It is, however, a poor medium for expressing the emotions and sensations that make life worth living.

Writing this thesis has been simultaneously one of the most difficult and enjoyable things I have ever done. It has been a mammoth task that, towards the end, consumed my every waking moment and even infiltrated by dreamings. Even now, as I write these lines at 6:25AM on a rainy Saturday morning, I find myself very grateful to the many people who have helped me along the way. I would like to acknowledge the aid of some of the people who have helped me perform experiments, contributed suggestions, or offered administrative assistance. To the many not mentioned here, I extend my unwritten gratitude.

My manager at Applied Materials, Arkadii Samoilov, was instrumental in this work. I entered his project at Applied with only theoretical knowledge of semiconductor processing, very little hands-on experience. He showed me how to design experiments not just to get results, but produce solutions. Through our many, lunch-time discussions he opened my eyes to the finer points of industrial semiconductor processing—that the capable research scientist must be part economist, part mechanic, part physicist, part artist, and part veteran. Experience is as important a teacher as are books. I look forward to a healthy and productive working relationship with him, and perhaps, just maybe, another chance to have him read “Zen and the Art of Motorcycle Maintenance” by Robert Pirsig.

To the members of the Epi Substrate Division at Applied Materials, I offer my general thanks. There are too many to list here, but each of you has always been ready and available to answer my questions, no matter how mundane or basic. I’d especially like to thank the two lab technicians, Jerry Lee and Lee Landice, for quickly fixing the chamber each of the many times I managed to break a wafer blade or fault the system.

To Gene Fitzgerald, I thank for the many insightful conversations we’ve had over the years. From our ramblings after quantum mechanics lectures to our barside chats, our discussions have always proved comprehensive, educational, and thoroughly entertaining. I have worked with Gene since my undergraduate sophomore year when I assisted the research of one of his graduate students. It was a logical choice to select him as my academic advisor for graduate studies. Despite his divided interests between MIT and Amberwave, I have always felt that when you have shared your suggestions or listened to my questions I was the recipient of your full attention.

To Dan Sparacin and Douglas Cannon, thank you for helping me to perform my measurements at MIT. Both of you went out of your way to help a fellow student get a few vital readings.

This thesis was funded by the MPMI corporate liaison between Applied Materials, Inc and the Materials Processing Center at MIT. I extend my gratitude to George “Buzz” Kenney and Jonathan Bartels for coordinating the logistics of the MPMI Program and for being my contacts at the Institute while I resided in California. This is an excellent program, though recently under-utilized, and I hope students take advantage of it in the future.

To my laptop computer, I give my only *dis*acknowledgement. Had it not been for its numerous crashes, stalls and other inventive ways of disrupting my work, this document would have been completed much sooner and with much less headache. I sincerely hope that in some small way the research performed in this thesis might help to make better computers, so machines like this one may soar far and high...into the scrap heap!

Quite unlike the laptop's influence, were the contributions of my girlfriend, Tiffany Ellis. How do I properly thank someone who has played so many roles so well? As editor, her eyes caught many of the minor errors in this manuscript once contained. As my primary MIT contact, Tiffany has, on occasion, checked out books for me, or photocopied articles or even once, a 100+ page thesis (that I never ended up citing). I am inexpressibly grateful. Staying up with me until the wee hours of the morning going over and over and over my presentation; by asking me questions both the simple and complex, you forced me to learn to explain myself in terms more accessible to an audience of non-material scientists. In the same semester that I was doing this research Tiffany began to play the guitar. One late night as she played for me the different harmonics, I gained new insight into the nature of light inside the waveguide (I'll leave it as an exercise for the reader to determine the connection). My far-away muse. For the bulk of the time that this thesis work took, we were separated geographically: I in California, she in Massachusetts. Yet, despite being separated by a large, and volatile nation, our affection has not waned. Soon, we shall both be alumni.

To my dear, and only sister, Debbie I wish you the best of luck in your new marriage and in completing your college studies. Keep reaching for the stars, because even if you miss, the stretching makes it easier to catch clouds.

To my mother, Heather Berlin, I thank you for your constant love and caring words. When it seemed that this thesis would never be finished you assured me by saying "Dean, you know what you have to do, so buckle down and do it." Mom, your words of encouragement have gotten me through the thick and thin, I shall never forget them. Over the years, you have always read my school papers, generously offering your edits and suggestions, though recently they've become too technical and advanced. I hope you are able to understand some of the words 28,210 that I've written here in these 118 pages, if not I'd be willing to explain anything with a pencil and the back of an envelope.

Ever since I was a child, I've wanted to be a scientist/engineer, and now that I have achieved my goal, my inspiring figure is not here to share in my joy. You first lit the flame in me that morning so many years ago when you let me help you as we built a shelving system for the pantry. To you, I offer this permanent written recognition I'll never have the chance to speak. My late father and my original engineer, Kenny Berlin.

I dedicate this document to my parents. I love you both.

A handwritten signature in black ink, appearing to read 'D. Berlin', with a stylized flourish at the end.

Dean Berlin
December 2, 2001

Chapter 9 References

- [1] International Technology Roadmap for Semiconductors: Front-End Processes, 1999 Edition.
- [2] Samavedam S.B., et al., "Elevated source drain devices using silicon selective epitaxial growth", *J. Vac. Tech. B*, 18(3) 1244-1250, May/June 2000.
- [3] Schäffler, F., "Review Article: High-Mobility Si and Ge structures", *Semicond. Sci. Technol.*, 12 (1997) 1515-1549.
- [4] WebElements™, the periodic table on the WWW, URL: <http://www.webelements.com/>.
- [5] *Landolt-Börnstein News Series* 1982 Group III, vol 17a, ed O Madelung (Berlin: Springer)
Landolt-Börnstein News Series 1989 Group III, vol 22a, ed. O Madelung (Berlin: Springer).
- [6] "Semiconductor Device Fundamentals" by Robert F. Pierret, Katherine Harutunian (Editor), Ben S. Bernanke (Contributor), Addison-Wesley Pub Co., March 1996.
- [7] Intel Corporation, 2001. <http://www.intel.com/pressroom/kits/quickreffam.htm>.
- [8] "Physics and Technology of Semiconductor Devices," by A. S. Grove, Wiley, New York, 1967.
- [9] Ghani T., et al, *Appl. Phys. Lett.* 58 (12), 25 March 1991.
- [10] Bernasconi P., et al., "Demonstration of 1 Tb/s Optical Packet Switch Fabric (80 x 12.5Gb/s), Scaleable to 128 Tb/s (6400 x 20Gb/s)", in *Tech. Dig. ECOC 2000*, Munich, Germany, 2000, Paper PD2-7.
- [11] "Silicon VLSI Technology: Fundamentals, Practice and Modeling" by J. Plummer, M. Deal, P. Griffin, C. Sodini (Series Editor), Prentice Hall, Inc. (2000).
- [12] "The Materials Science of Thin Films" by Milton Ohring, Academic Press (1992).
- [13] "The Science and Engineering of Microelectronic Fabrication" by Stephen A. Campbell, Oxford University Press (1996).
- [14] Ahlgren J.E., Jagannathan B., Dupuis M.D., IBM, "SiGe Fuels High-Speed Communications," *Semiconductor International*, November 2000.
- [15] Tsuji Y., Koshihara M., and Takimoto N., "Finite Element Beam Propagation Method for Anisotropic Optical Waveguides", *J. Lightwave Tech.*, vol 17, no 4, April 1999.
- [16] Matthews, J.W., *Epitaxial Growth, Part B* (Academic Press, New York, 1975).

- [17] "Dislocations in strained-layer epitaxy: theory, experiment, and applications", E.A. Fitzgerald, 1991.
- [18] Davies, G. and Newman, R.C., "Carbon in Monocrystalline Silicon", in "Handbook of Semiconductors", Vol. 3, ed. By T.S. Moss (Elsevier Science B. V., 1994).
- [19] Osten, H.J., "SiGeC Materials", *IEEE* 1996.
- [20] Source: Internet Software Consortium (<http://www.isc.org/>).
- [21] Mitchell T.O., Hoyt J.L., and Gibbons J.F., "Substitutional carbon incorporation in epitaxial Si_{1-y}C_y layers grown by chemical vapor deposition", *Appl. Phys. Lett.*, **71** (12), 22 Sept. 1997.
- [22] Lee, K.K., "Transmission and Routing of Optical Signals in On-Chip Waveguides for Silicon Microphotronics", MIT PhD Thesis, February, 2001.
- [23] Samoilov, A.V., et al., "Fine Control of Low-Temperature CVD Epitaxial Growth," *Solid State Technology*, May 2001.
- [24] "Fundamentals of Photonics," by B.E.A. Saleh and M.C. Teich, (John Wiley & Sons, Inc., NY, NY) 1991.
- [25] "Fundamentals of DWDM Technology" in "Introduction to DWDM for Metropolitan Area Networks", <http://www.cisco.com/univercd/cc/td/doc/product/mels/dwdm/>, Cisco Systems 2001.
- [26] Sah, C.T., "Evolution of the MOS Transistor – From Conception to VLSI," *IEEE Proc.*, **76**, 1280 (Oct. 1988).
- [27] Dance, B., "Carbon incorporation Controls Boron Dopant Diffusion in SiGe", *Semiconductor International*, November 2001.
- [28] Rücker H., et al., "Dopant Diffusion in C-doped Si and SiGe: Physical Model and Experimental Verification", *Proc. IEDM*, 1999, p. 345.
- [29] Osten, H.J., et al., "Carbon-containing Group IV Heterostructures on Si: Properties and Device Applications," *Thin Solid Films*, Vol. 321, p. 11, 1988.
- [30] "Solid State Physics" by Neil W. Ashcroft and N. David Mermin, Saunder College Publishing, 1976.
- [31] 2001 Aeronex, Inc. All rights reserved

- [32] Dash, W.C., and R. Newman, "Intrinsic Optical Absorption in Single-crystal Germanium and Silicon at 77K and 300K", *Phys. Rev.*, vol. 99, pp. 1151-1155, 1955.
- [33] Johnson, F.A., "Lattice Absorption Bands in Silicon," *Proc. Phys. Soc. (London)*, vol. 73, pp. 265-272, 1959.
- [34] Courtesy of Bell Laboratories, 2001.
- [35] Charles Evans and Associates, 2001. <http://www.cea.com/cai/simstheo/caistheo.htm>
- [36] Carroll, M.S., Chang, C-L., Sturm, J.C., Büyüklımanlı, T., "Complete suppression of boron transient-enhanced diffusion and oxidation-enhanced diffusion in silicon using localized substitutional carbon incorporation", *Appl. Phys. Lett.* **73**, 3695 (1998).
- [37] Kaiser, W., and Keck, P.H., "Oxygen Content of Silicon Single Crystals", *J. Appl. Phys.*, vol. 28, pp. 882-887, 1957.
- [38] Marcatili, E.A.J., "Dielectric Rectangular Waveguide and Directional Coupler for Integrated Optics", *Bell Sys. Tech. J.*, Sept. 1969, p. 2071-2102.
- [39] Goell, J.E., "A Circular-Harmonic Computer Analysis of Rectangular Dielectric Waveguides," *Bell Sys. Tech. J.*, Sept. 1969, p. 2133-2160.
- [40] Vescan, L., Poghossian, S.P., and Vonsovici, A., "High-Confinement SiGe Low Loss Waveguides for Si Based Optoelectronics", *Appl. Phys. Lett.*, **75** (1999) 1440.
- [41] Temkin, H., et al., *Appl. Phys. Lett.*, **49** (1986) 809.
- [42] Robillard, M., et al, "Strain-induced birefringence in Si_{1-x}Ge_x optical waveguides", *J. Vac. Sci. Technol. B.*, **16**(4), Jul/Aug 1998, p 1773.
- [43] *Properties of Silicon*, Inspec Emis Datareviews Series No. 4 (Inspec, London, 1988), p. 19.
- [44] M.J. Weber, *CRC Handbook of Laser Science and Technology* (CRC, Boca Raton, FL, 1986), p. 325.

Chapter 10 Appendix

Section 10.1 Units

The following units are used in this thesis and may be unfamiliar to the reader:

Torr

A measure of gas pressure equal to $133.32\text{kg}\cdot\text{m}^{-1}\cdot\text{s}^{-2}$. 760Torr is approximately equal to atmospheric pressure at sea level.

Standard liter per minute (slm)

Volumetric fluid flow equal to the movement 1 cubic decimeter of fluid (at 298°C and 760Torr) per minute. A measure of large gas flow.

Standard cubic centimeter per minute (sccm)

Volumetric fluid flow equal to the movement 1 cubic centimeter of fluid (at 298°C and 760Torr) per minute. A measure of small gas flow.

1000 sccm=1 slm

Relative flow for a given gas is the proportion of that flow to the total flow admitted to the chamber.

1σ

Data uniformity measurement equal to the standard deviation of the data set divided by the mean of the data set for a normal distribution expressed as a percentage. For a normal Gaussian distribution, $1\sigma \leq 1\%$ means that approximately 68.3% of the data deviates by less than 1% from the mean. It can also mean simply the standard deviation, not divided by the mean, and it is then expressed with the appropriate units. 1σ is also quoted as "1s."

Decibel (dB)

One tenth of the common logarithm of the ratio relative powers equal to 0.1 B (bel). The decibel is the common unit, not the bel. It is a measurement of signal attenuation. The ratio in dB is given by

$$dB = 10 \log_{10} \left(\frac{P_{in}}{P_{out}} \right)$$

Equation 10.1

In Equation 10.1, dB gives the signal loss between the power inserted into a transmission medium, P_{in} , and the power received, P_{out} .

Section 10.2 Derivation of Wave Equations

Maxwell's differential equations of electrodynamics are:

$$\begin{aligned}\epsilon_0 \nabla \cdot \vec{E} &= \rho \\ \nabla \times \vec{E} &= -\frac{\partial \vec{B}}{\partial t} \\ \nabla \cdot \vec{B} &= 0 \\ \nabla \times \vec{B} &= \mu_0 \vec{J} + \mu_0 \epsilon_0 \frac{\partial \vec{E}}{\partial t}\end{aligned}$$

Equation 10.2

Since a waveguide does not contain current sources and is non-magnetic, $\vec{J} = \rho = 0$, and these equations simplify to:

$$\begin{aligned}\nabla \times \vec{E} &= -\frac{\partial \vec{B}}{\partial t} \\ \nabla \cdot \vec{B} &= 0 = \epsilon_0 \nabla \cdot \vec{E} \\ \nabla \times \vec{B} &= \mu_0 \epsilon_0 \frac{\partial \vec{E}}{\partial t}\end{aligned}$$

Equation 10.3

It is a mathematical fact that the curl of a curl of a vector field results in the divergence of a gradient, so

$\nabla \times \nabla \times = \nabla^2$. ∇^2 is a second-derivative operator called the Laplacian Operator, which is given by

$$\nabla^2 = \frac{\partial^2}{\partial x^2} + \frac{\partial^2}{\partial y^2} + \frac{\partial^2}{\partial z^2}$$

Equation 10.4

Using the Laplacian Operator, Maxwell's equations of Equation 10.3 can be further reduced to the wave equations:

$$\begin{aligned}\nabla^2 \vec{E} &= \mu_0 \epsilon_0 \frac{\partial^2 \vec{E}}{\partial t^2} \\ \nabla^2 \vec{B} &= \mu_0 \epsilon_0 \frac{\partial^2 \vec{B}}{\partial t^2}\end{aligned}$$

Equation 10.5

The permittivity of free-space is $\epsilon_0=8.8542 \times 10^{-12}$ F/m and the permeability of free-space $\mu_0=1.2567 \times 10^{-6}$ H/m. It is a pleasant surprise to find that both of these fundamental constants are related to another familiar constant, the speed of light, c :

$$(\mu_0 \epsilon_0)^{-1/2} = c = 3 \times 10^8 \text{ m/s}$$

Equation 10.6

For a time-harmonic field with an angular frequency ω , the time-dependence can be eliminated from Equation 10.5 by choosing

$$\begin{aligned} \vec{E}(\vec{r}, t) &= \text{Re} \left\{ \vec{E}(\vec{r}) e^{-i\omega t} \right\} \\ \vec{B}(\vec{r}, t) &= \text{Re} \left\{ \vec{B}(\vec{r}) e^{-i\omega t} \right\} \end{aligned}$$

Equation 10.7

Combining Equation 10.5 and Equation 10.7 leads to the homogenous equations:

$$(\nabla^2 + \omega^2 \mu_0 \epsilon_0) \vec{E} = 0 = (\nabla^2 + \omega^2 \mu_0 \epsilon_0) \vec{B}$$

Equation 10.8

where $\vec{E} = \vec{E}(\vec{r})$.

Electromagnetic waves are transverse waves; waves in which the varying quantities are directed perpendicular to the direction of motion (Figure 10.1).

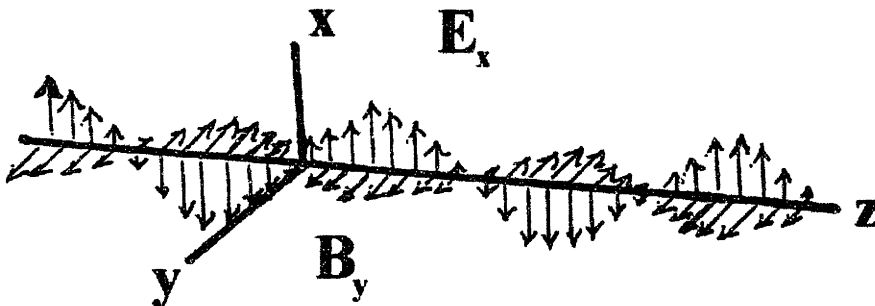


Figure 10.1: Electric and magnetic field in an electromagnetic wave

A useful expression of magnitude of the *electric field* of these waves is

$$E = E_0 \cos(\omega t - kz)$$

Equation 10.9

The *magnetic field* oscillates at right angles to the electric field, so

$$B = B_0 \cos(\omega t - kz) = \frac{E_0}{c} \cos(\omega t - kz)$$

Equation 10.10

Two important parameters of the wave are presented: the wave number, k , and the angular frequency, ω

$$k = \frac{2\pi}{\lambda}$$

Equation 10.11

$$\omega = 2\pi\nu$$

Equation 10.12

The wavenumber, with units of reciprocal length ($[=] \text{ m}^{-1}$) is the natural unit of measurement in reciprocal space where the periodic, repeating sense of the wave is expressed as a point. This representation is useful when visualizing the interaction of electromagnetic periodicity with lattice periodicity in a crystalline solid, or when visualizing the modes possible in a boundary condition such as in the core of a rectangular dielectric waveguide. The angular frequency, expressed as radians/sec, describes the rate the electromagnetic vector rotates in the complex plane. Inserting Equation 10.9 into Equation 10.5 shows that Equation 10.9 is in fact a solution if

$$\frac{\omega}{k} = (\mu_0 \epsilon_0)^{-1/2} = \lambda \nu = c$$

Equation 10.13

This elegant expression shows ω/k to represent the velocity of light in a medium, in the case of Equation 10.13 a vacuum. When this oscillating electromagnetic field interacts with the electrons in a non-magnetic solid, the dielectric constant in Equation 10.6 and Equation 10.13 is replaced by the *relative dielectric constant*, ϵ_r , and the velocity becomes

$$\frac{\omega}{k} = (\mu_0 \epsilon_r \epsilon_0)^{-1/2} = c \epsilon^{-1/2} = c'$$

Equation 10.14

The light velocity in the material has been reduced by the factor $\epsilon_r^{-1/2}$, and so the *index of refraction* is defined

$$n = \epsilon_r^{1/2}$$

Equation 10.15

By considering the boundary conditions at the interface between the vacuum and the dielectric, where the time dependence of the fields is shown to be the same on either side of the interface, it is observed that ω does not change. However, since ω/k is decreased by n , k must have increased by n , implying that the wavelength, λ , is decreased by a factor of n . This decrease of the wavelength is the reason light is refracted. Refraction is observed as a bending of the light towards the surface normal when moving from a material of lower index of refraction into a material of higher index. This bending is captured in Snell's Law, which can be derived from the trigonometric Law of Sines:

$$n_1 \sin \theta_1 = n_2 \sin \theta_2$$

Equation 10.16

Section 10.3 Aeronex GateKeeper® Hydride Gas Purifier Data Sheet

AERONEX, INC. • 5975 Flanders Drive • San Diego, CA 92121
TEL 858 452 0124 • FAX 858 452 0229

AERONEX
High Purity Fluid Delivery

GATEKEEPER®

Hydride Gas Purifier Series

Features

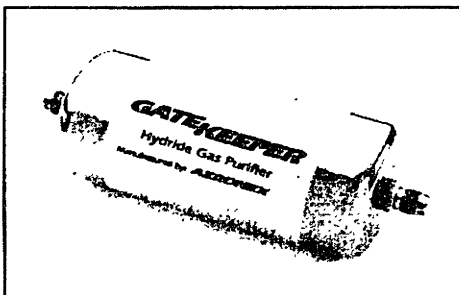
- Removes H₂O, O₂, CO₂, CO, NMHC's, and oxidation by-products from Hydrides to <1 ppb outlet gas purity
- Operates at ambient temperature
- Regenerable
- 0.003 µm and larger particle filtration
- No heat or power required
- Does NOT release hydrocarbons
- Optional Preconditioning

Applications

- MOCVD
- Doping
- Molecular Beam Epitaxy
- Compound Semiconductors

Specifications

- Purifying Media: Metal Oxide/Reduced Metal
- Gases Purified: NH₃, SiH₄, GeH₄, AsH₃, PH₃, B₂H₆, and Hydride/Carrier gas mixtures
- Contaminants Removed: H₂O, O₂, CO₂, CO, non-methane hydrocarbons and oxidation by-products
- Outlet Purity: up to 99 9999999% pure gas or 1ppb for impurities listed
- Leak Rating 1X10⁻⁹ atm cc/sec



Aeronex's GateKeeper® Hydride series purifiers remove H₂O, O₂, CO₂, CO, NMHC's and oxidation by-products present in high purity hydride gases. The integrated filter removes 99.9999999% of all particles 0.003 µm and larger.

Even the highest purity gas is subject to molecular or particulate contamination. This can occur through the manufacturing process, transfer into and degradation of the storage container, and later as the result of contact with the gas delivery system. For the full range of point-of-use to bulk gas applications, the GateKeeper purifier prevents this contamination and insures your gas purity. In the case of corrosive gases, use of the GateKeeper purifier in gas cabinets and valve manifold boxes has also been shown to extend the life of your other components.

GateKeeper® Hydride series purifiers have been shown to improve compound semiconductor film quality. Low oxygen levels are critical for performance of films such as SiGe, GaN, GaAs, and InP.

Unlike other purification technologies, GateKeeper® Hydride series purifiers do not contain organic compounds that can outgas and cause contamination to critical processes. GateKeeper Hydride purifiers are factory regenerable. Optional preconditioning is available for some gases.

For more information, please call 800 511 9761 or visit our web site at www.aeronex.com

Figure 10.2: Aeronex GateKeeper® Data Sheet-1 [31]

GATEKEEPER® Hydride Series Specifications

MODEL	35K	70K	100K	500K	2500K	5000K
Maximum Flow Rate	1slm	3slm	20slm	60slm	60slm**	60slm**
Max Δ Pressure	200 psid (1380 kPa)					
Max Internal Pressure	3000 psig (20,700kPa)		500 psig (3450 kPa)		700 psig (4830 kPa) Max. valve pressure 300psig (2070 kPa)	
Pressure Drop	Consult Factory					
Purifying Media	Metal Oxide/Reduced Metal					
Gases Purified	NH ₃ , SiH ₄ , GeH ₄ , AsH ₃ , PH ₃ , B ₂ H ₆ , and Hydride/Carrier gas mixtures Call Aeronex for information on purifying other gases					
Gases Removed	H ₂ O, O ₂ , CO ₂ , CO, non-methane hydrocarbons and oxidation by-products					
Outlet Purity	<1ppb					
Operating Temperature	- 40° F to +150° F (- 40° C to + 65° C)					
Inlet / Outlet Connections	¼" Face Seal			¼" or ½" Face Seal		½" Face Seal
Isolation Valves	Optional			Included		
Filter	0.003 μm sintered stainless steel outlet filter for particle removal					
Housing	316L Stainless Steel internally electropolished to 10Ra					
Leak Rating	1 x 10 ⁻⁹ atm cc/sec					
Approximate Shipping Weight	0.7 lbs (0.3 kg)	0.9 lbs (0.4 kg)	2 lbs (0.8 kg)	3.5 lbs (1.6 kg)	20 lbs (9.3 kg)	34lbs (15.5 kg)
Order Information	Consult Factory For Specific Part Numbers					

**Consult factory regarding high flows

*For more information on GateKeeper purifier sizes, gas compatibility, or product life,
please call Aeronex at 1 800 511 9761 or visit our web site at www.aeronex.com*

GateKeeper® is a registered trademark of Aeronex Incorporated

© Aeronex Inc. 1999

All rights reserved

Figure 10.3: Aeronex GateKeeper® Data Sheet-2 [31].

THESIS PROCESSING SLIP

FIXED FIELD: ill. _____ name _____

index _____ biblio _____

► COPIES: Archives Aero Dewey Barker Hum
Lindgren Music Rotch Science Sche-Plough

TITLE VARIES: ► _____

NAME VARIES: ► _____

IMPRINT: (COPYRIGHT) _____

► COLLATION: _____

► ADD: DEGREE: _____ ► DEPT.: _____

► ADD: DEGREE: _____ ► DEPT.: _____

SUPERVISORS: _____

NOTES:

cat'r:

date:

► DEPT: Mt+Soc&E

page:
► F58

► YEAR: 2002 ► DEGREE: SM

► NAME: BERKIN, Dean Edward